

An-Najah National University

Faculty of Graduate Studies

Ga_{1-x}Mn_xN Magnetic Semiconductors: First-Principles Study

Prepared by

Farah Ali Deib Saleh

Supervised by

Dr. Abdel-Rahman Mustafa Abu-Labdeh

Dr. Mohammed Salameh Salem Abu-Jafar

This thesis submitted in partial fulfillment of the requirements for the degree of Master of Science in Physics, Faculty of Graduated Studies, at An-Najah National University, Nablus, Palestine.

2008

Ga_{1-x}Mn_xN Magnetic Semiconductors:

First-Principles Study

To my Family

by

Farah Ali Deib Saleh

This Thesis was defended successfully on 18/11/ 2008. and approved by

Committee Members

- **Dr. Abdel-Rahman Abu-Labdeh** (Supervisor)
- **Dr. Mohammed S. Abu-Jafar** (Co-Supervisor)
- **Dr. Rezek Estaiteh** (External Examiner)
- **Dr. Musa El-Hasan** (Internal Examiner)

Signature

Abdel-Rahman
Mohammed S.
Rezek Estaiteh
Musa El-Hasan

Dedication

To the Memory of my Mother

and

To my Family

Acknowledgment

I would like to convey my sincere gratitude to my supervisor Dr. Abdel-Rahman Abu-Labdeh and the co-supervisor Dr. Mohammed Abu-Jafar for their close supervision, Indispensable encouragement, and guidance throughout all stages of this work. My thanks are sent out to all my friends and Teachers who supported and guided me during this work, especially brother Dr. Belal Al-qassem-Jordan, Prof. Dr. Jamil Khalifeh-University of Jordan, and Dr. S. Goumri Said–France-Universite, of Paris.

I would like to thank all my Teachers at An-Najah National University, and appreciation and special thanks to my group at my faculty, sisters and brothers whom without their support this work would not be possible, especially my faithful friends (Omar Isleem and Na'eem Malak).

Finally, special gratitude is paid to my father, brothers, kids and my wife for their constant support and encouragement.

إقرار

أنا الموقع أدناه مقدم الرسالة التي تحمل العنوان:

Ga_{1-x}Mn_xN Magnetic Semiconductors: First-Principles Study

أقر بان ما اشتملت عليه هذه الرسالة إنما هي نتاج جهدي الخاص ، باستثناء ما تمت الإشارة إليه حيثما ورد ، وأن هذه الرسالة ككل ، أو أي جزء منها لم يقدم من قبل لنيل أية درجة أو لقب علمي أو بحثي لدى أي مؤسسه تعليمية أو بحثية أخرى.

Declaration

The work provided in this thesis, unless otherwise referenced, is the researcher's own work, and has not been submitted elsewhere for any other degree or qualification.

Student's name:

اسم الطالب :

Signature:

التوقيع :

Date:

التاريخ:

Contents

<i>Section</i>	<i>Subject</i>	<i>Page</i>
	Committee Decision	ii
	Dedication	iii
	Acknowledgment	iv
	Declaration	v
	Contents	vi
	List of Tables	x
	List of Figures	xii
	Abstract	xvii
1	Introduction	1
2	Theoretical modeling	8
2.1	Introduction	8

2.2	The Density Functional Theory(DFT)	12
2.2.1	The Local Spin Density Approximation(LSDA)	16
2.2.2	Generalized Gradient Approximation(GGA)	17
2.3	Kohn-Sham Approach	18
2.3.1	Total Energy and Force	18
2.3.2	The Kohn-Sham Equations	19
2.3.3	Magnetism	23
2.3.4	The Eigenvalue Problem	24
2.4	Full-Potential Linearized Augmented Plane-Wave FP-LAPW	28
2.4.1	The Augmented Plane Wave Method (APW)	29
2.4.2	Linearized Augmented Plane Wave Method (LAPW)	31
2.4.3	The (FP-LAPW) Method	34

2.5	The WIEN2K Program	36
3	Results And Discussion	39
3.1	Convergence Tests	39
3.1.1	k-Points Test	40
3.1.2	$R_{MT} \cdot K_{max}$ Cutoff Test	50
3.2	GaN, MnN Bulk Properties	59
3.2.1	Optimization procedure of the lattice constants for GaN and MnN	62
3.2.2	GaN and MnN Electronic Properties	64
3.3	$Ga_{1-x}Mn_xN$ Ternary Alloys	68
3.3.1	Optimization procedure of the lattice constants for $Ga_{1-x}Mn_xN$	69
3.3.2	Computational Details	71
3.3.3	$Ga_{1-x}Mn_xN$ Alloys Geometry	72

3.3.4	Ga_{1-x}Mn_xN Electronic Properties	77
3.4	Ga_{1-x}Mn_xN Magnetic Properties	79
4	Summary and Conclusion	83
	References	87
	Appendix	98

List of Tables

Table 3.1:	K-Points test at initial cutoff energy 13.5 Ry = 183.7 eV for GaN in ZB structure.	41
Table 3.2:	K-Points test at initial cutoff energy 14.5 Ry = 197.4 eV for MnN in ZB structure.	41
Table 3.3:	K-Points tests for $Ga_{1-x}Mn_xN$ optimization procedure ($x = 0.125, 0.25$).	42
Table 3.4:	K-Points tests for $Ga_{1-x}Mn_xN$ optimization procedure ($x = 0.5, 0.75$).	43
Table 3.5:	The final $K_{irred.}$ and $K_{mesh.}$ that is sufficient to perform the calculations at initial cutoff energy 13.5 Ry = 183.7 eV for (GaN)Mn in Zb structure.	44
Table 3.6:	$R_{MT.K_{max}}$ cutoff test at initial cutoff energy 13.5 Ry = 183.7 eV for GaN in Zb structure	51
Table 3.7:	$R_{MT.K_{max}}$ cutoff test at initial cutoff energy 14.5 Ry = 197.4 eV for MnN in Zb structure	51
Table 3.8:	$R_{MT.K_{max}}$ tests for $Ga_{1-x}Mn_xN$ optimization procedure.	54

Table 3.9:	$R_{MT}.K_{max}$ tests for $Ga_{1-x}Mn_xN$ optimization procedure.	55
Table 3.10:	$R_{MT}.K_{max}$ cutoff test at initial cutoff energy 13.5 Ry = 183.7 eV for $Ga_{1-x}Mn_xN$ in ZB structure	56
Table 3.11:	Calculated and experimental structural parameters of GaN at equilibrium.	60
Table 3.12:	Calculated and experimental structural parameters of MnN at equilibrium.	61
Table 3.13:	Calculated and experimental energy band gap (E_g) of GaN and MnN in ZB-structure (in eV).	67
Table 3.14:	Evaluated and optimized lattice constants for $Ga_{1-x}Mn_xN$.	70
Table 3.15:	A summary of the energy band gaps (eV) for $Ga_{1-x}Mn_xN$.	79
Table 3.16:	Magnetic moments in $Ga_{1-x}Mn_xN$ systems.	81

List of Figures

Figure 2.1:	Flowchart for the n th iteration in the selfconsistent procedure to solve Kohn-Sham equation.	22
Figure 2.2:	Space as two regions: Muffin Tin (MT) region with radius R_{mt} and Interstitial (I) region.	30
Figure 2.3:	Flowchart of the WIEN2K program.	38
Figure 3.1:	GaN k-Points Test in the ZB-structure by (a) LSDA and (b) GGA Approximation methods.	45
Figure 3.2:	MnN k-Points Test in the ZB-structure by (a) LSDA and (b) GGA Approximation methods.	46
Figure 3.3:	k-Points tests for $Ga_{1-x}Mn_xN$ with composition $x = 0.125$ in the ZB structure using : a) LSDA method and b) GGA method.	47
Figure 3.4:	k-Points tests for $Ga_{1-x}Mn_xN$ with composition $x = 0.25$ in the ZB structure using : a) LSDA method and b) GGA method.	48

Figure 3.5:	k-Points tests for $\text{Ga}_{1-x}\text{Mn}_x\text{N}$ with composition $x = 0.5$ in the ZB structure using : a) LSDA method and b) GGA method.	49
Figure 3.6:	k-Points tests for $\text{Ga}_{1-x}\text{Mn}_x\text{N}$ with composition $x = 0.75$ in the ZB structure using : a) LSDA method and b) GGA method.	50
Figure 3.7:	$R_{\text{MT}} \cdot K_{\text{max}}$ Cutoff test for GaN by: a) LSDA and b) GGA approximation methods.	52
Figure 3.8:	$R_{\text{MT}} \cdot K_{\text{max}}$ Cutoff test for MnN by: a) LSDA and b) GGA approximation methods.	53
Figure 3.9:	$R_{\text{MT}} \cdot K_{\text{max}}$ tests for $\text{Ga}_{1-x}\text{Mn}_x\text{N}$ with composition $x = 0.125$ in the ZB structure using: a) LSDA method and b) GGA method.	56
Figure 3.10:	$R_{\text{MT}} \cdot K_{\text{max}}$ tests for $\text{Ga}_{1-x}\text{Mn}_x\text{N}$ with composition $x = 0.25$ in the ZB structure using : a) LSDA method and b) GGA method.	57
Figure 3.11:	$R_{\text{MT}} \cdot K_{\text{max}}$ tests for $\text{Ga}_{1-x}\text{Mn}_x\text{N}$ with composition $x = 0.50$ in the ZB structure using : a) LSDA method and b) GGA method.	58

Figure 3.12:	$R_{MT} \cdot K_{max}$ tests for $Ga_{1-x}Mn_xN$ with composition $x = 0.75$ in the ZB structure using : a) LSDA method and b) GGA method.	59
Figure 3.13:	Optimization procedure for GaN using : a) LSDA and b) GGA methods.	63
Figure 3.14:	Optimization procedure for MnN using : a) LSDA and b) GGA methods.	64
Figure 3.15:	ZB-GaN Band structure (spin polarized system) using LSDA method.	65
Figure 3.16:	ZB-GaN Band structure (spin polarized system) using GGA method.	66
Figure 3.17:	ZB-MnN Band structure (spin polarized system) using GGA method.	68
Figure 3.18:	Unit cell used to simulate the $Ga_{1-x}Mn_xN$ alloys with compositions: a) $x = 0$, b) $x = 1$.	73
Figure 3.19:	Unit cell used to simulate the $Ga_{1-x}Mn_xN$ alloys with compositions: a) $x = 0.125$, b) $x = 0.25$	74

Figure 3.20:	Unit cell used to simulate the $Ga_{1-x}Mn_xN$ alloys with compositions: a) $x = 0.50$, b) $x = 0.75$	74
Figure 3.21:	Total energy per atom as a function of volume for the alloys $Ga_{1-x}Mn_xN$ for $x = 0.125$ with approximations: a) LSDA, b) GGA.	75
Figure 3.22:	Total energy per atom as a function of volume for the alloys $Ga_{1-x}Mn_xN$ for $x = 0.25$ with approximations: a) LSDA, b) GGA.	75
Figure 3.23:	Total energy per atom as a function of volume for the alloys $Ga_{1-x}Mn_xN$ for $x = 0.50$ with approximations: a) LSDA, b) GGA.	76
Figure 3.24:	Total energy per atom as a function of volume for the alloys $Ga_{1-x}Mn_xN$ for $x = 0.75$ with approximations: a) LSDA, b) GGA.	76
Figure 3.25:	The spin polarized band structure for $Ga_{0.75}Mn_{0.25}N$ in the ZB- structure: a) Majority spin, b) Minority spin.	77

Figure 3.26:	The spin polarized band structure for $\text{Ga}_{0.25}\text{Mn}_{0.75}\text{N}$ in the ZB- structure: a) Majority spin, b) Minority spin.	78
Figure 4.1:	Evaluated and optimized lattice constants vs. the Mn concentration for the $\text{Ga}_{1-x}\text{Mn}_x\text{N}$ systems.	83
Figure 4.2:	Magnetization for the MnN compound as a function of the lattice parameter in both approaches LSDA and GGA.	85

Ga_{1-x}Mn_xN Magnetic Semiconductors: First-Principles Study

By

Farah Ali Deib Saleh

Supervisor

Dr. Abdel-Rahman Abu-Labdeh

Co-Supervisor

Dr. Mohammed Abu-Jafar

Abstract

We present the results of First-Principles calculations of the magnetic semiconductors for $Ga_{1-x}Mn_xN$ systems taking the concentrations (0.0, 0.125, 0.25, 0.50, 0.75, 1.00) in the Zinc-blende Structure (ZB-Structure), using a self-consistent full-potential linearized augmented plane-wave (FP-LAPW) method implemented by the WIEN2K package. The local spin density approximation (LSDA) as well as the generalized gradient approximation (GGA) are used to treat the exchange correlation potential, and taking into account spin polarization.

In order to design new or employ the existing diluted magnetic semiconductor materials, the underlying mechanisms of magnetism must be understood. The total energy versus lattice constant is obtained using the spin density functional theory (DFT). It is found that the equilibrium lattice parameters strongly depend on the concentration of the Mn-dopant (x). Also we found that the energy band gaps (E_g) for these systems depend on (x), in other words the energy band gap decreases by increasing the Mn concentration.

We mainly studied the Bulk parameters of our system, band structures, and magnetic properties. We made numerical investigations of the structural, magnetic properties for simple cases under pressure, in other part of our results we report an analysis of structures, magnetic properties of the $Ga_{1-x}Mn_xN$, i.e GaN doped with Mn, with different concentrations, 0.125, 0.25, 0.5, 0.75 and so for major, minor compounds (GaN, MnN).

Chapter One

Introduction

In recent years, group III-nitrides have attracted the interest of many researchers due to their scientific and technological applications. These materials are regarded as hopeful wide-band-gap semiconductors for optoelectronic applications in the short wavelength range as well for high temperature, high-power, and high-frequency electronic devices [1]. The most important applications of these materials are the short wavelength laser diodes (LDs), which are used for optical disk readout, and high efficiency light-emitting diodes (LEDs), for full color display [2, 3, 4]. Integrated circuits (ICs) used for data processing use the charge of electrons in semiconductors, while data storage media such as hard disks use the spin of electrons in a magnetic material.

Recently, various types of spin polarization have been formed in semiconductors such as carrier spin, spin in introduced magnetic atoms, and nuclear spin of constituent atoms. It has been shown that new functions can be implemented by injecting, transporting and controlling these spin states. This is resulting in the emergence of a new field-semiconductor spin electronics (or semiconductor spintronics) involving the use of spin states inside semiconductor materials.

Semiconductor spin electronics may be divided into two fields. One might be referred to as semiconductor magneto-electronics, which can be defined as semiconductor materials that are also magnetic or combinations of semiconductors and magnetic materials. As an application for

semiconductor magneto-electronics are, optical isolators, magnetic sensors, and non-volatile memories that can be integrated into semiconductor devices. The other field is probably best referred to as semiconductor quantum spin electronics, which is a semiconductor for which the main focus is on using the quantum mechanical nature of spin in semiconductors.

Earlier time, research of semiconductor materials of group III-nitrides have been taken up, since its applications are immediately clear for all. Many researchers have been attempted to improve the efficiency of blue devices using II-VI materials, it was partially successful [5]. This makes many of them to go back to III-V with open field for many possibilities, since much progress is yet to be made in developing these materials.

The outstanding properties of the group III-nitrides are mainly related to the specific role of the nitrogen (N) atoms, in which the smallness of the N atom (0.7 \AA covalent radius compared with the group III atoms, $1.1\text{-}1.4 \text{ \AA}$) gives rise to the formation of short bond with a large bond ionicity [6, 7, 8]. Nitrogen atom, therefore reduces the lattice parameters of group III-nitrides compared with III-V compounds. For example, the lattice parameters for gallium nitride (GaN) in the wurtzite structure is 4.5 \AA , while for GaAs, GaSb and GaP in the same structure are 5.65 \AA , 6.1 \AA , 5.45 \AA , respectively [6]. Hence the melting points for group III-nitrides are high. Also the size of N atom appears to play essential role in determining the stable crystal structure for these compounds [9].

The group III-nitride can crystallize in wurtzite (Wz), zinc-blende (ZB) and rocksalt (RS) structures [10]. The wurtzite structure is a stable phase for

most of group-III compounds [11]. A phase transition to the rocksalt, however, can take place at high pressure. The zinc-blende structure may be stabilized just for GaN [9], so that GaN has been studied in depth in ZB-structure [11, 12, 13].

GaN is an important compound in III-nitrides group. It has been studied in more than one structure, mainly Wz and ZB structures [14, 10]. It was pointed out that this compound has an average lattice constant of about 4.5 \AA in ZB structure and $a = 3.2 \text{ \AA}$ and $c = 5.19 \text{ \AA}$ in Wz structure [15]. Also, it was found that GaN is a nonmagnetic semiconductor material with a direct band-gap of about 3.23 eV [16, 17]. Other researchers, however, found that the band-gap of GaN is about 2.1 eV [18]. The main problem with GaN technology is its cost. A special process is required to grow a GaN crystal (or wafer) on which transistors and integrated circuits (ICs) can be fabricated [19, 20]. Once the process is implemented on a large scale, the cost should come down.

The advantages of GaN devices include high output power with small physical volume, and high efficiency in power amplifiers at ultra-high and microwave radio frequencies [21]. In spite of the advantages of GaN devices, these devices are nonmagnetic semiconductors. It is worth to produce new materials with magnetic properties. Producing of magnetic semiconductors have been made by several techniques.

The first important one is the molecular-beam epitaxy (MBE). The principle of MBE growth is relatively simple. It consists of molecule by molecule deposition of material desired composition from a molecular

beam. In spite of the simplicity, a great technological effort is required to produce systems that yield the desired quality in terms of material purity, uniformity and interface control. To obtain high-purity layers (pure materials), it is critical that the material sources be extremely pure and that the entire process be done in an ultra-high vacuum environment.

Another important feature is that growth rates are typically on the order of a few Angstroms per second ($\text{\AA}/\text{s}$) and the beams can be shuttered in a fraction of a second, allowing for nearly atomically unexpected sudden transitions from one material to another. One can fabricate artificial periodic super lattices consisting of alternating layers of different semiconductors, different metals or different semiconductors and metals [22]. Joonyeon Chang *et al* were able to produce gallium manganese nitride $Ga_{1-x}Mn_xN$ as a magnetic semiconductor material, using MBE technique [23]. Their study was performed to determine the change in lattice parameter of epitaxial Mn-doped GaN films with low Mn concentrations (0.0006 - 0.005) grown by plasma-enhanced molecular beam epitaxy by which added Mn distribution can be investigated. Secondary ion mass spectroscopy reveals that the Mn profiles for the films are uniform throughout the entire thickness range of (0.7- 1.0) μm with no noticeable isolation. It was found that the lattice parameter for $Ga_{1-x}Mn_xN$ is larger than those for the GaN.

Another way for production of magnetic semiconductors is the multi layers fabrication. One important class of ferromagnetic semiconductors that can be produced using the multi layers technique is $A_{1-x}Mn_xB$, where A denotes the group-III ion, specially Ga, and B denotes As or N. $A_{1-x}Mn_xB$ is a

ferromagnetic semiconductor whose parameters may be tailored by Mn doping. Tanaka and Higo have taken an approach to spin polarized tunneling in epitaxial systems [24]. However, the magnetization of the $Ga_{1-x}Mn_xN$ layers were not fully antiparallel, which expects even larger effects for a fully antiparallel alignment. They were able to explain the barrier thickness dependence of the tunnel magneto-resistance (TMR) [25, 26]. The role of the interfacial GaN layers, however, was not addressed. Though it may perhaps expected to be minimal. Given the recent interest in spin-polarized transport [27], these results are almost certain to be extended in future investigations. The third way for producing magnetic semiconductor materials by inclusion of transition metal atoms in the non magnetic semiconductor lattice. The first material produced by this way was $In_{1-x}Mn_xAs$ [28], where Mn atoms replace In atoms in the InAs semiconductor. Ferromagnetic semiconductors would be the natural choice to overcome material incompatibilities in metal-semiconductor interfaces, and display an excess of new possibilities to interlink magnetic properties with existing semiconductor technologies [29, 30]. The enormous potential of this type of materials was immediately recognized, which initiated the ongoing quest for a fully-fledged room temperature magnetic semiconductor material that is compatible with existing semiconductor technologies. These materials that we propose called diluted magnetic semiconductors (DMSs) [31], which are mostly based on III-V and II-VI compound semiconductors with embedded Cr, Mn or Co atoms. DMSs can be defined as semiconductors doped with magnetic impurities and therefore combine magnetic with semiconducting properties.

The important property of most of III-nitride semiconductors that the direct band gaps of the group III-nitride alloys span an extremely wide energy range from near infrared in InN to deep ultraviolet in AlN, offering possibilities for new device applications of these materials [11, 12]. All the unusual properties of the alloys are well described by a band anti-crossing (BAC) model [32], that considers an interaction between localized nitrogen states and the extended states of the conduction band.

In the present system Mn has been doped in different concentrations in the nonmagnetic semiconductor GaN. Mn is one of the 3d transition metals and it is a paramagnetic material [33, 10]. It has 25 electrons, a cubic structure with $I-43m$ space group [10, 34]. The experimental lattice constant for cubic Mn is 8.91 \AA [14, 10].

The aim of this work is to understand the role of the exchange coupling and to investigate its impact in determining magnetic properties for the $Ga_{1-x}Mn_xN$ systems ($x = 0.125, 0.25, 0.50, 0.75$), also the major and minor compounds GaN and MnN respectively. Although the structural as well as the magnetic properties of some of these systems have been investigated experimentally for very low concentrations [89, 91], few theoretical studies based on total energy calculations exist for $x < 0.5$ due to computational difficulties [12].

In order to have more information about the aim of this work, we have to study the basics of the semiconductor alloys and to investigate this phenomenon for some different magnetic doped structures (Mn concentrations), namely the $Ga_{1-x}Mn_xN$ systems. From the theoretical point

of view, an intense activity has been devoted to the problem of diluted semiconductor alloys (DMSs), essentially focusing on the oscillatory character of the coupling. The most direct way to study the DMSs theoretically is the first-principle total energy calculations. The first-principle calculations play a very important role in elucidating the mechanism of DMS. On one hand, they provide a test of the qualitative predictions of the simplified models; while on the other hand, they yield quantitative predictions for realistic systems that can be compared with experimental observations.

In this work we use one of the most accurate methods for calculating the electronic structure of ordered materials, which is the full-potential linearized augmented plane-wave (FP-LAPW) method as implemented in program package WIEN2K [45]. This method is based on density functional theory (DFT), using the local (spin) density approximation (LSDA) or the generalized gradient approximation (GGA) for the exchange-correlation energy.

The outline of the thesis is as follows. The basics of DFT, and FP-LAPW as methods are discussed in chapter two. In chapter three we report and discuss our results obtained for the $Ga_{1-x}Mn_xN$ systems. Computational details used in this work are also discussed in chapter three. The main results and conclusions of the present work are summarized in chapter four.

Chapter two

Theoretical Modeling

2.1 Introduction

During the past ten years, first-principles calculations based on the density functional theory (DFT) [35], with the local (spin-) density approximation (LSDA) or the generalized gradient approximation (GGA) [36] emerged as the most powerful framework to reply to the demands on a microscopic level. By first-principles or *ab initio*, respectively, is meant, that the parameters of the theory are fixed by the basic assumptions and equations of quantum mechanics and, for our discussion, density functional theory. The overwhelming success of the density functional theory for the description of the ground-state properties of large material classes including insulators, semiconductors, semimetals, half-metals (half-metals are defined as magnetic materials showing a band gap at the Fermi energy for one spin direction), simple metals, transition-metals and rare-earths in bulk, at surfaces and as nanostructures makes it the unchallenged foundation of any modern electronic structure theory. The wide applicability combined with the predictive power of the approach turned it to the standard model in material science. In principle, the only input needed for the theory are the atomic numbers of the constituent atoms of a system, all other properties follow as a direct consequence of the density functional equations. In practice, the definition has to be modified since one is always limited to some set of model systems. These limitations might include system size, crystal structure, neglect of disorder, low or zero

temperature, or any number of other restrictions on the phase space to probe. While some of these restrictions and limitations are burdensome, the goal of calculations is not merely to obtain numbers, but rather insight. By focusing on well-defined, but restricted models, by working on chemical trends rather than on isolated case studies, by investigating systems in hypothetical no equilibrium structures or follow simulations in idealized environments, which may not be realized in experiments, one is able to develop different levels of understanding of the system in question and may hopefully learn which aspects of the problem are important. In the density functional theory we work in an effective one-particle picture: the wave-functions are solutions of the Kohn-Sham equations and the interaction of the particles is taken into account by a self-consistent field, which depends on the density of the particles.

In any practical implementation the computational effort increases significantly with the number of electrons that have to be taken into account. The observation that the chemical binding is determined almost entirely by the valence electrons, while the influence of the core electrons is negligible, has given rise to the idea to replace the core electrons by an effective potential, so they don't have to be taken explicitly into account. This is done in pseudo potential plane wave methods, and the set of functions chosen as basis are plane waves. The pseudo potential plane wave method has been applied with a great success to understand and predict the solid state properties, especially for semiconductors, as well as metals. On the other hand, there are reasons to why alternative methods are attractive. For some elements there is a significant interaction between core and valence electrons, or one may be interested in properties due to the

core electrons. Thus, different basis set should be designed to expand the wave functions.

Successful extensions of the theoretical framework treat quasiparticle excitations of weakly correlated electron systems by many-body perturbation theory based on Green function techniques in the so-called GW approximation for the electronic self-energy [37], or by time-dependent density functional theory (TDDFT) [38]. The treatment of strongly correlated electron systems is currently being explored investigating the LDA+U approximation, the optimized effective potential method (OEP) [39] and by combining the dynamical mean field theory (DMFT) with the LDA.

In this chapter we review the full-potential linearized augmented plane wave (FP-LAPW) method [40] to solve the density functional equations for a crystalline solid, ultra thin film and one-dimensional system [41]. The method originates from the APW method proposed by Slater [42]. Great progress of the APW methodology was achieved as the concept of linear methods, was introduced by Andersen, and first applied by Koelling and Arbman using a model potential within the muffin-tin approximation [43].

The linearized APW (LAPW) method reconciled the linear-algebra formulation of the variational problem with the convergence properties of the original formulation and allowed a straight forward extension of the method to the treatment of crystal potentials of general shape. The treatment of the potential and charge density without shape approximation [44] and the implementation of the total energy [40] led to the development

of FP-LAPW bulk, film codes [45]. It was during this time that the power and accuracy of the method were demonstrated to the community, largely through a series of calculations of surface and adsorbate electronic structures. These and other demonstrations established the FP-LAPW method as the method of choice for accurate electronic structure calculations for a broad spectrum of applications. Constant conceptual and technical developments and refinements such as the proposal and implementation of the scalar-relativistic approximation (SRA) [46]. The spin-orbit interaction by second variation, and the possibility to calculate forces [47] acting on the ions to carry out structure optimizations, Quasi-Newton methods [48] to accelerate the self consistency iterations, the iterative diagonalization techniques [44], the proposal of new efficient basis sets, the LAPW+LO and APW+LO [49] basis, in which the APW basis is amended by local orbitals (LO), the extension of the method to non-collinear magnetism[50], to the wire geometry [51], to calculations of the quasiparticle self-energy in the GW approximation[26], and the recent formulation and application of the scattering problem in semi-infinite crystals[52] has made APW-like methods. For our discussion the FP-LAPW method, a robust, versatile and flexible method, at reasonable computational expense. It is an all-electron method, that means, one works with a true crystal potential, which diverges as $1/r$ at the nucleus, as opposed to the pseudo-potential [53], in which the singularity is removed. Due to the all electron nature of the method, magnetism is included rigorously and nuclear quantities e.g. isomer shift, hyperfine field, electric field gradient (EFG), and core level shift are calculated routinely [54]. The method and the breadth of applications has benefited from the large growth of available computing power and parallelization strategies.

This chapter starts with a quick overview to the many body problem to interest studying Density functional theory (DFT), as the method of our calculations, so the approximations used LSDA, GGA are discussed. Kohn- Sham ansatz outlining the general aspects of the first-principles method followed by an introduction of the augmented plane wave methods, APW like concepts to solve the Kohn-Sham equation for a periodic solid. Then, we discuss the linearized augmented plane wave (LAPW) basis set method, as an improvement to APW.

The full potential linearized augmented plane wave FP-LAPW method is described in detail for bulk solids followed by a short description of adaptations of the FP-LAPW methods to systems of reduced dimensions (nanoscience) , the film and wire geometry. Finally an analysis of the CPU time distribution across the different steps of an ab initio and first-principles calculations with an FP-LAPW program is presented. Strategies to speed-up the calculations in the light of symmetry and parallelization concepts are described.

2.2 The Density Functional Theory (DFT)

The ultimate goal in theoretical physics is to solve the many-particle Schrödinger equation including all ions and electrons in the system under consideration as well as their interactions. The equation can be written as :

$$Hy(R_1, R_2, \dots, R_i, r_1, r_2, \dots, r_j) = -i\hbar \frac{\partial}{\partial t} \psi(R_1, R_2, \dots, R_i, r_1, r_2, \dots, r_j) \quad (2.2.1)$$

where coordinates $\{R_i\}$ denotes dynamical variables of ions, and coordinates $\{r_j\}$ for electrons. To solve this kind of equations, it is

impossible to have analytical solution, since it is unknown for the simplest atoms and smallest molecules. The usual restriction to the time independent Schrödinger equation, where the time derivative in (2.2.1) is replaced by the energy E , does not change the picture. Therefore because of the large mass of the ions, we have to use some approximations. The ions can quite generally be described as classical particles whose trajectory at all times is described by only their positions and velocities.

In general, wave-function based first-principles calculations approach the atomistic interactions at the fundamental level - quantum physics is utilized by solving Schrödinger's equation for the many-body problem of the electronic structure. The complexity of this approach is obvious - in general the wave function of the many-particle system depends on the coordinates of each particle and, thus, the treatment of any system larger than a small number of electrons is not feasible. DFT provides some kind of compromise in the field of first-principles and ab initio concepts, and can be applied to the fully interacting system of many electrons. DFT is based on theorems of Hohenberg and Kohn [35], who demonstrated that the total ground state energy E of a system of interacting particles is completely determined by the electron density ρ . Therefore, E can be expressed as a functional of the electron density and the functional $E(\rho)$ satisfies the variational principle. [55] then rederived the rigorous functional equations in terms of a simplified wave function concept, separating the contributions to the total energy as,

$$E[\mathbf{r}(\mathbf{r})] = T_s \mathbf{r}(\mathbf{r}) + \int V(\mathbf{r}) \mathbf{r}(\mathbf{r}) d\mathbf{r} + \frac{1}{2} \int \frac{\mathbf{r}(\mathbf{r}) \mathbf{r}(\mathbf{r}')}{r-r'} d\mathbf{r} d\mathbf{r}' + E_{xc} \mathbf{r}(\mathbf{r}) \quad (2.2.2)$$

In which T_s represents the kinetic energy of a non-interacting electron gas, V the external potential of the nuclei. The last term, E_{xc} , comprises the many-body quantum particle interactions, it describes the energy functional connected with the exchange and correlation interactions of the electrons as fermions. Introducing the Kohn-Sham orbitals the solution of the variational Euler equation corresponding to the functional of equation 2.2.2 results in Schrödinger like equations for the orbitals Ψ

$$\left(-\frac{\hbar^2}{2m}\nabla^2 + V_{\text{eff}}(\mathbf{r})\right)\Psi(\mathbf{r}) = \epsilon\Psi(\mathbf{r}) \quad (2.2.3)$$

These are the renowned Kohn-Sham equations which are then actually solved (after introducing the approximations described below). Equation 2.2.3 transforms the many-particle problem into a problem of one electron moving in an effective potential such that

$$V_{\text{eff}}(\mathbf{r}) = V(\mathbf{r}) + \int \frac{r(r')}{|\mathbf{r}-\mathbf{r}'|} dr' + \frac{dE_{xc}(r)}{dr} \quad (2.2.4)$$

which describes the effective field induced by the other quantum particles. The actual role of the auxiliary orbitals is to build up the true ground state density by summing over all occupied states.

$$r(\mathbf{r}) = \sum \Psi^*(\mathbf{r})\Psi(\mathbf{r}) \quad (2.2.5)$$

In short, the reformulation of Kohn and Sham provides a suitable basis, which transforms the functional equation into a set of differential equations. The resulting equations can be solved in a self-consistent manner. The crucial point for actual applications is the functional E_{xc} , which is not known (and therefore has no analytical expression) and it therefore requires approximations. The historically first and widely used

approximation is the local density approximation (LDA), which is based on the assumption that the exact exchange-correlation energy can be locally at the point r be replaced by the expression and value for an homogeneous electron gas,

$$E_{xc} = \int r(r) e_{xc} r(r) dr \quad (2.2.6)$$

In which $e_{xc}(\rho)$ is the exchange-correlation energy per particle of the homogeneous electron gas. The function $e_{xc}(\rho)$ has to be partially-approximated as well [56], but this can be done accurately by computer simulations. Several methods have been utilized to parameterize the many-body interactions of a homogeneous gas of interacting electrons, for instance by many body perturbation theory or periodic density functional theory calculations within the full-potential linearized augmented - plane wave (FP-LAPW) approach as implemented in the WIEN2k package. Various improvements have been proposed by going beyond the most simple local assumption of LDA taking into account the gradient of the electron density.

Nowadays, this is done by the so-called generalized gradient approximation (GGA), which counteracts the over binding of LDA, e.g. equilibrium volumes are increased whereas cohesive properties are reduced when compared to standard LDA [57] results. In many applications, GGA provides a substantially improved description of the ground state properties, in particular for 3d transition metals, such as ours; (Mn) transition metal.

2.2.1 The Local Spin Density Approximation (LSDA)

The initial formulation of DFT dealt only with nonmagnetic systems, i.e. wave- functions, densities, and potentials with only one spin-component which is LDA. In this case, the approximate functionals are usually expressed in an unrestricted version, where not the electron density $\mathbf{r}(r)$, but the two spin-densities, $\mathbf{r}_{\uparrow}(r)$ and $\mathbf{r}_{\downarrow}(r)$, with $\mathbf{r}_{\uparrow}(r) + \mathbf{r}_{\downarrow}(r) = \mathbf{r}(r)$ are employed as the central input. In particular for open shell situations with an unequal number of spin-up (\uparrow) and spin-down (\downarrow) electrons, functionals of the two spin densities consistently lead to more accurate results. But also for certain situations with even number of electrons, such as the H₂ molecule at larger separation, the unrestricted functionals perform significantly better because they allow symmetry breaking. Up to this point the local density approximation was introduced to a functional depending solely on $\mathbf{r}(r)$. If we extend the LDA to the unrestricted case, we arrive at the local spin-density approximation (LSDA).

$$E_{xc}^{LSDA}(\mathbf{r}_{\uparrow}, \mathbf{r}_{\downarrow}) = \int \mathbf{r}(r) e_{xc}(\mathbf{r}_{\uparrow}(r), \mathbf{r}_{\downarrow}(r)) dr \quad (2.2.7)$$

Just for the simple, spin compensated situation where $\mathbf{r}_{\uparrow}(r) = \mathbf{r}_{\downarrow}(r) = 1/2 \mathbf{r}(r)$ there are related expressions for the exchange and correlation energies per particle of the uniform electron gas characterized by $\mathbf{r}_{\uparrow} \neq \mathbf{r}_{\downarrow}$, the so-called spin polarized case. The degree of spin-polarization is often measured through the spin-polarization parameter Z

$$Z = \frac{\mathbf{r}_{\uparrow}(r) - \mathbf{r}_{\downarrow}(r)}{\mathbf{r}(r)} \quad (2.2.8)$$

Z attains values from 0 (spin compensated) to 1 (fully spin polarized, i.e. all electrons have only one kind of spin).

2.2.2 Generalized Gradient Approximation (GGA)

In a very straightforward elegant way this problem was solved by enforcing the restrictions valid for the true holes also for the hole of the beyond - L(S)DA functionals. Functionals that include the gradients of the charge density are collectively known as generalized gradient approximations (GGA). These functionals are the workhorse of the current density functional theory and can be generically written as:

$$E_{xc}^{GGA}(\mathbf{r}_\uparrow(r), \mathbf{r}_\downarrow(r)) = \int f(\mathbf{r}_\uparrow(r), \mathbf{r}_\downarrow(r), \nabla \mathbf{r}_\uparrow(r), \nabla \mathbf{r}_\downarrow(r)) d\mathbf{r} \quad (2.2.9)$$

As one will see, several suggestions for the explicit dependence of this integrand f on the densities and their gradients exist, including semi-empirical functionals which contain parameters that are calibrated against reference values rather than being derived from first principles. In practice, E_{xc}^{GGA} is usually split into exchange and correlation contributions

$$E_{xc}^{GGA} = E_x^{GGA} + E_c^{GGA} \quad (2.2.10)$$

and approximations for the two terms are sought individually. The exchange part can be written as:

$$E_x^{GGA} = E_x^{LSDA} - \sum_s \int F(S_s) r_s^{4/3}(r) dr \quad (2.2.11)$$

The argument of the function is the reduced gradient for spin $\frac{3}{4}$:

$$S_s(r) = \left| \frac{\nabla \mathbf{r}_s(r)}{r_s^{4/3}(r)} \right| \quad (2.2.12)$$

The Where s_{σ} is to be understood as a local inhomogeneity parameter. It assumes large values not only for large gradients, but also in regions of small densities, such as exponential tails far from the nuclei. Likewise, small values of s_{σ} occur for small gradients, typical for bonding regions, but also regions for large density [58].

2.3 Kohn-Sham Approach

2.3.1 Total Energy and Force

In the density functional theory, the total energy $E(\mathbf{R}, \Psi_i)$ of a system of interacting atoms and electrons is a functional of the atomic positions \mathbf{R} and the electron density $\rho(\mathbf{r})$. The electron density can be expressed in terms of M occupied single-particle orbitals $\Psi_i(\mathbf{r})$:

$$\rho(\mathbf{r}) = \sum_{i(occ)}^M |\Psi_i(\mathbf{r})|^2 \quad (2.3.1)$$

Where i labels the states. If the total energy functional $E(\dot{\mathbf{R}}, \Psi_i(\dot{\mathbf{r}}))$ is minimized with respect to the electronic degrees of freedom $\Psi_i(\dot{\mathbf{r}})$, we recover the Born-Oppenheimer surface $f_i(\dot{\mathbf{r}})$:

$$f_i(\dot{\mathbf{r}}) = \min_{\Psi_i} E(\dot{\mathbf{R}}, \Psi_i) \quad (2.3.2)$$

on which the atoms move. The derivative of $\rho_i(\dot{\mathbf{r}})$ with respect to the atomic position R^m gives the force F^m ,

$$F^m = -\nabla_{\mathbf{R}^m} \Phi(\dot{\mathbf{R}}) \quad (2.3.3)$$

exerted on the atom μ , which ties electronic structure to structural optimization and molecular dynamics calculations. The energy functional is divided into several terms:

$$\mathbf{E}(\dot{\mathbf{R}}, \Psi_i) = E_{kin}(\Psi_i) + E_H(\Psi_i) + E_{xc}(\Psi_i) + E_{ext}(\dot{\mathbf{R}}, \Psi_i) + E_{ion}(\dot{\mathbf{R}}) \quad (2.3.4)$$

where E_{kin} is the kinetic energy of non-interacting electrons, E_H is the Hartree energy, i.e. the classical Coulomb energy of the electrons, and E_{xc} is the exchange-correlation energy which contains terms coming from the Pauli principle (exchange hole), from correlations due to the repulsive Coulombic electron-electron interaction and from the contribution to the kinetic energy of interacting electrons [59]. E.g. In the local density approximation $E_{xc}(r(\mathbf{r}))$ is written in the form

$$E_{xc}(r) = \int r(r) e_{xc} r(r) dr$$

Then, E_{ext} is the interaction energy of the electrons with the ions, e.g. described by the ... $\frac{1}{r}$ potential as in all-electron methods or by pseudo potentials, and E_{ion} is the classical Coulomb energy of the ions.

2.3.2 The Kohn-Sham Equations

The single-particle wave functions $\Psi_i(\mathbf{r})$ are obtained by minimization of the total energy with respect to the wave functions subject to the normalization constraint

$$\int |\Psi_i(\mathbf{r})|^2 dr = 1 \quad (2.3.5)$$

This leads to the Kohn–Sham equations [55], an eigenvalue problem for the electronic eigenfunctions $\Psi_i(\mathbf{r})$ and the eigenvalues ε_i :

$$\hat{H}(\mathbf{r})\Psi_i(\rho) = \varepsilon_i\Psi_i(\mathbf{r}) \quad (2.3.6)$$

where all quantities depend on the electron density ρ . According to the form of the total energy Eq. (2.3.4), the Hamiltonian \hat{H} is a sum of corresponding terms and the eigenvalue problem is written in the form:

$$(\hat{T}_o + \hat{V}_{ext} + \hat{V}_H + \hat{V}_{xc})\Psi_i = \varepsilon_i\Psi_i \quad (2.3.7)$$

The first approximation in such a hierarchy is the well-known Born-Oppenheimer (BO) or also called adiabatic approximation. It is based on the large difference masses between the electrons and the nuclei. Therefore, the electrons move much faster than the nuclei and to a good approximation the positions of the nuclei can be assumed to be static. In this way the motion of the electrons is separated from the motion of the nuclei, which now form an "external" potential to the electrons, i.e., the electrons move in the field of fixed nuclei (Born and Oppenheimer, 1927). Thus, within this approximation, the kinetic energy of the nuclei can be neglected, where the nuclei-nuclei interaction in Eq. (2.3.7) enters the total energy expression as a constant.

In the real space representation the individual terms are the following:

$$\text{kinetic energy : } \hat{T}_o = -\frac{\mathbf{h}^2}{2m}\nabla_r^2 \quad (2.3.8)$$

$$\text{external potential : } \hat{V}_{ext} = -\frac{1}{4\pi\varepsilon_o} \sum_{i,j} \frac{e^2 Z_i}{|\mathbf{R}_i - \mathbf{r}_j|} + \frac{1}{2} \frac{1}{4\pi\varepsilon_o} \sum_{i \neq j} \frac{e^2 Z_i Z_j}{|\mathbf{R}_i - \mathbf{R}_j|} \quad (2.3.9)$$

$$\text{Hartree potential: } \Delta V_H(\mathbf{r}) = 4\pi e^2 \rho(\mathbf{r}) \quad (2.3.10)$$

$$\text{xc - potential(L(S)DA) : } V_{xc}(\mathbf{r}) = \frac{\partial}{\partial \rho(\mathbf{r})} \int \rho(\mathbf{r}) \varepsilon_{xc} \rho(\mathbf{r}) d\mathbf{r} \quad (2.3.11)$$

Even though the resulting electronic Hamiltonian is much simpler than the original one, the remaining electronic many-body problem is still far too difficult to be solved. In a pseudo-potential approach V_{ext} is replaced for each atom by a pseudo-potential V_{ps} . The terms $V_H(r)$ and $V_{xc}(r)$ are local potentials and explicitly density dependent. Thus, the Hamiltonian $\hat{H}(r)$ and the wave functions $\Psi_i(r, \mathbf{r})$ are also dependent on the electron density $\rho(\mathbf{r})$.

Together with the expression Eq. (2.3.1) a self-consistency problem to obtain the charge density $\rho(\mathbf{r})$ is established, which is solved iteratively until the input density (used to define the potential terms in the Hamiltonian) is equal to the output density within the required accuracy. The number of self consistency iterations N_{iter} is considerably reduced applying Quasi-Newton methods [48].

The external potential $V_{ext}(\mathbf{R})$ depends explicitly on the positions $\{\mathbf{R}\}$ of all atoms, which change at certain steps to optimize the atomic structure or every time-step of a molecular dynamics algorithm. Thus, the Hamiltonian $\hat{H}(\{\mathbf{R}\})$ and the wave functions $\Psi_i(\mathbf{R}(t), r)$ are also dependent on the atomic

positions $\{\mathbf{R}\}$. After the self-consistency condition for the electron density has been fulfilled, the atom positions are moved by a molecular static or molecular dynamics time-step, $\mathbf{R}(t) \rightarrow \{\mathbf{R}(t + \Delta t)\}$. Thus, for NMD molecular time steps the eigenvalue problem has to be solved N_{MD} \cdot N_{iter} times. These arguments suggest a particular loop structure of a typical first-principles method and a particular sequence how the different elements are calculated. This is summarized in Figure 2.1.

Typical codes use L(S)DA exchange-correlation potentials and energies of Hedin and Lundqvist [60] or Vosko, Wilk, and Nusair [61], or GGA functionals of Perdew et al. [62] are given as analytical expressions of the density and their derivatives in case of the GGA.

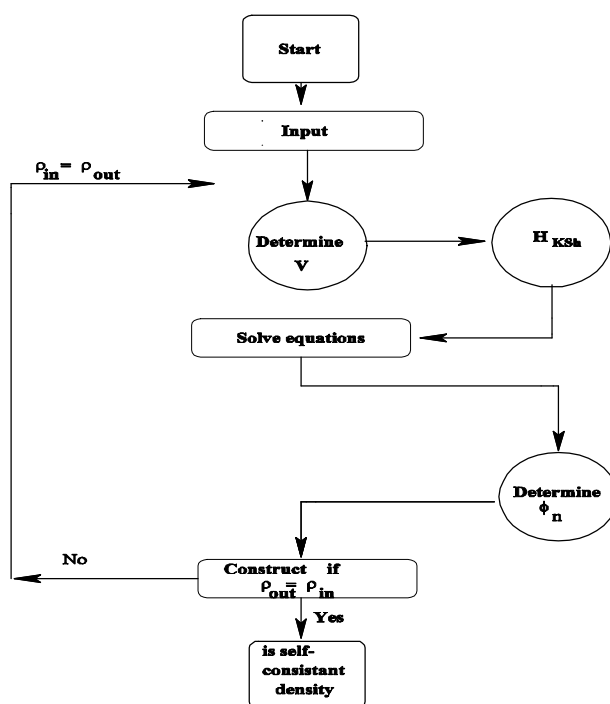


Figure 2.1: Flowchart for the n th iteration in the selfconsistent procedure to solve Kohn-Sham equation.

2.3.3 Magnetism

If magnetism occurs, the ground state has a broken symmetry and the ground-state energy is described by functionals which depend on the vector-magnetization density $m(\mathbf{r})$ as an additional field to the ordinary charge density $r(\mathbf{r})$, discussed so far. An additional term $m_B \mathbf{S} \cdot \mathbf{B}_{xc}(\mathbf{r})$ appears in the Kohn-Sham equations Eq. (2.3.7), where $m_B = \frac{e\hbar}{2mc}$ is the Bohr magneton, \mathbf{B}_{xc} is the magnetic xc-field an electron experiences, and \mathbf{S} are the Pauli spinors. Thus, calculating magnetic systems, one works in a two dimensional spin-space and the basis functions y_{is} carry an additional spin label $s = \pm 1$.

The Hamiltonian is a 2×2 matrix in spin-space and is now hermitian and not symmetric. Complex magnetic structures lower frequently the symmetry of the problem and more states have to be calculated or a much large fraction of the BZ has to be sampled, respectively, pushing the computational effort to the limits of modern supercomputers. In case of collinear magnetism, e.g. Ferro-, ferri-, or anti-ferromagnetism, $\mathbf{S} \cdot \mathbf{B}_{xc}$ reduces to $s_z B_{xc}$, the Hamiltonian is diagonal in spin space, the magnetization density $m_z(\mathbf{r})$ is then given by spin-up and -down densities, $m_z(\mathbf{r}) = r_{\uparrow}(\mathbf{r}) - r_{\downarrow}(\mathbf{r})$, and the effort of a magnetic calculation is just twice that of a nonmagnetic one.

In general, the magnetic moment $\mathbf{M} = \int m(\mathbf{r}) d\mathbf{r}$ is a vector quantity, and the search of the magnetic structure can be done dynamically bearing

similarities to the dynamical structure optimization combining molecular dynamics and simulated annealing. Therefore, everything said in this chapter on structural optimization applies to both, the atomic and the magnetic structure.

2.3.4 The Eigenvalue Problem

In all-electron methods, eigenvalue problem Eq. (2.3.7) is solved for all occupied states i but typically subject to different boundary conditions. As shown schematically in Figure 2.1 we distinguish core electrons from valence electrons. The former have eigen-energies which are at least a couple of Rydbergs below the Fermi energy, the potential they experience is to an excellent approximation spherically symmetric and the wave-functions have no overlap to neighboring atoms. The eigenvalue problem of these states is solved applying the boundary conditions of isolated atoms, which is numerically tackled by a shooting method. Valence electrons in a crystalline solid form electron bands and the eigenvalue problem is solved subject to the Bloch boundary conditions. The eigenstate is classified by the band index n and a three-dimensional Bloch vector k within the first Brillouin zone, ($i \in \{kn\}$). Some materials contain chemical elements with states (e.g. $5p$ states of $4f$ elements, p states of early transition metals) intermediate between band and core states and those are coined semicore states. These are high-lying and extended core states and particular care has to be taken on their treatment since their treatment as core states can cause significant errors in total energy, force and phonon calculations. According to the different treatment of the electrons, we decompose the charge density in the valence, semicore and core densities

$$\rho(\mathbf{r}) = \rho_{val}(\mathbf{r}) + \rho_{ps}(\mathbf{r}) + \rho_{core}(\mathbf{r}) \quad (2.3.12)$$

the latter being spherically symmetric. The charge densities are calculated according to Eq. (2.3.1). Wave functions and energies of core states give access to hyperfine quantities such as isomer shifts, hyperfine fields and electric field gradient as well as chemical shifts of core levels. There are many possible ways to solve the Kohn-Sham equations for valence electrons. Frequently, a variational method is chosen by which a wave function $y_{kn}(\mathbf{r})$ of Bloch vector \mathbf{k} and band index n is sought as a linear combination of basis functions $j_r(\mathbf{k}, \mathbf{r})$

$$\psi_{kv}(\mathbf{r}) = \sum_{n=1}^N C_{kn}^n j_n(\mathbf{k}, \mathbf{r}) \quad (2.3.13)$$

satisfying the Bloch boundary conditions. C_{kn}^n are the expansion coefficients of the wave function (coefficient vector), and N is the number of basis functions taken into account. By this expansion, the eigenvalue problem

$$\hat{H} y_{kn}(\mathbf{r}) = e_{kn} y_{kn}(\mathbf{r}) \quad (2.3.14)$$

is translated into an algebraic eigenvalue problem of dimension N

$$(H(\mathbf{k}) - e_{kn} S(\mathbf{k})) C_{kn}^n = 0, \quad \forall \mathbf{k} \in \mathbf{BZ} \quad (2.3.15)$$

for the coefficient vector C_{kn}^n corresponding to the eigenvalues e_{kn} . The Hamilton $H^{n,n'}(\mathbf{k})$ and overlap matrices $S^{n,n'}(\mathbf{k})$ are hermitian or real symmetric, depending on the point symmetry of the atomic structure. If the basis functions are orthonormal, i.e. $\langle j_n | j_{n'} \rangle = d_{n,n'}$, as for example in case of simple plane waves, then the overlap matrix S , defined as

$$S^{n,n'}(\mathbf{k}) = \int_{\mathcal{Q}} \mathbf{j}_n^*(\mathbf{k}, \mathbf{r}) \mathbf{j}_{n'}(\mathbf{k}, \mathbf{r}) d^3 r \quad (2.3.16)$$

becomes diagonal, $S^{n,n'}(\mathbf{k}) = \delta_{n,n'}$, and the generalized eigenvalue problem Eq. (2.3.15) becomes of standard type. Ω is the volume of the unit cell. In general, the general eigenvalue problem is reduced to a standard one using the Cholesky decomposition. It can be shown (e.g. [63]), that any hermitian and positive definite matrix can be decomposed into a matrix product of a lower triangular matrix with only positive diagonal elements and its transposed. Clearly, the overlap matrix satisfies these conditions and can be written $S = LL^T$. Therefore, Eq. (2.3.15) becomes

$$HC_i = \varepsilon_i LL^T C_i \quad (2.3.17)$$

Or it can be written as:

$$P x_i = \varepsilon_i x_i, \quad P = L^{-1} H (L^{-1})^T \quad \text{and} \quad x_i = L^T C_i \quad (2.3.18)$$

Thus, the generalized eigenvalue problem has been reduced to a simple one. The eigenvectors C_i can be obtained by the back-transformation, $C_i = (L^T)^{-1} x_i$.

The choice of the most efficient numerical algorithm to solve Eq. (3.2.15) depends on the number of basis functions N and the number M of states n taken into account. If $\frac{M}{N} > 0.1$, direct numerical diagonalization schemes are employed. If $\frac{M}{N} < 0.1$ or if N is too large to fit the eigenvalue problem into the memory of a computer the eigenvalue problem is solved iteratively. Any iterative solution of an eigenvalue problem can be divided into two parts:

(i) The determination of the iterative improvement of the state vector $C_{kn}^{n',m}$ at iteration step m by multiplying the Hamiltonian with the state vector to obtain the update $C_{kv}^{n,[m+1]}$:

$$C_{kv}^{n,[m+1]} = \sum_{n'} H^{n,n'}(\mathbf{k}) C_{kn}^{n',m} \quad (2.3.19)$$

and (ii) the orthonormalization of the wave functions

$$\sum_n \{ C_{kv}^{n,[m+1]} C_{kv'}^{n,[m+1]} \} = \delta_{v,v'} \quad (2.3.20)$$

Frequently, each iteration step is accompanied by a direct sub-space diagonalization of a dimension proportional to M , on which Hamiltonian H is projected. If the multiplication of H.C can be made fast by expressing the Hamiltonian in terms of dyadic products or convolutions as in norm conserving or ultra-soft pseudo-potentials minimizing thereby the number of multiplications, iterative methods become particular beneficial.

The number of basis functions N is determined by the required precision P of a calculation and by the volume Ω of the unit cell or the number of atoms in the unit cell, N_A , respectively. The precision P is controlled by the finest real-space resolution the basis functions can resolve. For three dimensional unit cells N scales as NaP^3 . In general, the triple (N_K, M, N) , the number of k -vectors in the BZ used, the number M of states n considered, and the number of basis functions N are determined by the required precision of the calculation and by the volume of the unit cell as mentioned before. These parameters determine the CPU time and memory requirements of the calculations.

2.4 Full-Potential Linearized Augmented Plane-Wave (FP-LAPW)

The primary computational task in DFT is the solution of the KS equations for a given crystalline structure. "Solving" in most methods means that we want to find the coefficients c_p^m needed to express f_m in a given basis set f_p^b

$$f_m = \sum_{p=1}^P c_p^m f_p^b \quad (2.4.1)$$

In principle, the number of basis functions is infinite ($P = \infty$); in practice one works with a limited set of basis functions. Such a limited basis will never be able to describe f_m exactly, but one could try to find a basis that can generate a function that is 'close' to f_m . To do that, there are two points to strive for when choosing a basis set, (i) mathematically simple basis functions, in order to simplify the setup of matrix elements. (ii) basis functions that are will designed to describe the electronic states of the systems that minimize the size of the basis set, and hence the dimension of the secular equation.

In any practical implementation the computational effort increases significantly with the number of electrons that have to be taken into account. The observation that the chemical binding is determined almost entirely by the valence electrons, while the influence of the core electrons is negligible, has given rise to the idea to replace the core electrons by an effective potential, so they don't have to be taken explicitly into account. This is done in pseudo potential plane wave methods, and the set of functions chosen as a basis are plane waves. The pseudo potential plane

wave method has been applied with a great success to understand and predict the solid-state properties, especially for semiconductors, as well as metals. On the other hand, there are reasons to why alternative methods are attractive. For some elements there is a significant interaction between core and valence electrons, or one may be interested in properties due to the core electrons. Thus, different basis set should be designed to expand the wave functions.

2.4.1 The Augmented Plane Wave Method (APW)

The APW method is a procedure for solving Kohn-Sham equations by introducing a basis set which is especially adapted to the problem. This adoption is achieved by dividing the space into two regions as shown in Fig.2.2.

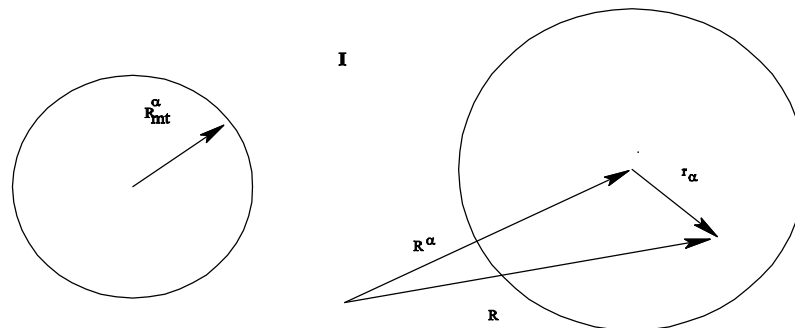


Figure 2.2: Space as two regions: Muffin Tin(MT) region with radius R_{mt} and Interstitial(I) region.

- (i) The Muffin Tin region: where a sphere of radius R_{MT}^{α} is drawn around each atom. The spheres (usually called muffin tin spheres) are non overlapping spheres and centered at the atomic sites, R^{α} . (ii) An interstitial region (call it I), which fills the space outside the spheres. In these regions different basis sets are used:

$$\varphi_{k+K}^{APW}(\mathbf{r}) = \begin{cases} \frac{1}{\sqrt{V}} e^{i(\mathbf{k}+\mathbf{K})\cdot\mathbf{r}}, & \mathbf{r} \in I \\ \sum_{l,m} A_{lm}^{a,\mathbf{k}+\mathbf{K}} u_l^a(r_a, \varepsilon) Y_{lm}(\hat{r}_a), & |r_a| \leq R_{MT}^a \end{cases} \quad (2.4.2)$$

where \mathbf{K} is the reciprocal lattice vector, \mathbf{k} is the wave vector inside the first Brillouin Zone (BZ), and V is the volume of the unit cell. The Y_{lm} are the spherical harmonics, A_{lm} are expansion parameters and the position inside the sphere is given by $\mathbf{r}_a = \mathbf{r} - \mathbf{R}_a$. Finally, $u_l^a(r_a, e)$ is the regular solution of the radial Schrödinger equation for a spherical potential inside the sphere with a radius R_{MT}^a .

$$\left\{ -\frac{\hbar^2}{2m} \frac{\partial^2}{\partial r^2} + \frac{\hbar^2}{2m} \frac{l(l+1)}{r^2} + V(r) - E \right\} r u_l(r) = 0 \quad (2.4.3)$$

The dual representation defined by Eq. (2.4.2) is not guaranteed to be continuous on the sphere boundary, as it must be for the kinetic energy to be well defined. Accordingly, it is necessary to impose this constraint. In the APW method this is done by requiring that the augmented functions match (in value not in slope) the plane waves at the atomic sphere boundary, and there is no restriction on the derivative at the atomic sphere boundary. Therefore, the APW basis functions have in general a kink at $|r_a| = R_{MT}^a$ and their derivations are discontinuous at the boundary. A further drawback is the energy dependence of the functions $u_l^a(r_a, e)$, leading to a non-linear eigenvalue problem, which is computationally quite demanding, that what led to another method called Linearized Augmented Plane Waves LAPW.

2.4.2 Linearized Augmented Plane Waves (LAPW) Method

In the linearized augmented plane waves method (LAPW), the basis functions and their first derivatives are required to be continuous at the boundary between core and interstitial region. Since the matching criteria are strictly mathematical, the shape of the resulting linear combination will differ in general from the shape of the physical solution $u_l^a(r_a, e)$. The more important change is, that the radial functions $u_l^a(r_a, e)$ are expanded around a fixed energy, in other words the basis functions (radial) u_l^a in the muffin-tins were supplemented by their energy derivatives \dot{u}_l^a , but both, u_l^a and \dot{u}_l^a , are now evaluated at a fixed energy e_l . The original energy dependence of the radial basis function is thereby replaced by the Taylor series:

$$u_l^a(r_a, e) = u_l^a(r_a, e_l) + (e - e_l) \left. \frac{\partial u_l^a(r_a, e)}{\partial e} \right|_{e=e_l} + O(e - e_l) \quad (2.4.4)$$

In this way, the wave functions are affected by an error which is quadratic in the deviation of the eigenvalue e from the energy parameter e_l , the error in the eigenvalues enter only to fourth order [64]. Substituting the first two terms of the expansion in the APW for fixed e_l gives the definition of the LAPW

$$f_{k+K}^{LAPW}(\mathbf{r}) = \begin{cases} \frac{1}{\sqrt{V}} e^{i(\mathbf{k}+\mathbf{K})\cdot\mathbf{r}}, & \mathbf{r} \in I \\ \sum_{l,m} [A_{lm}^a u_l^a(r_a, e_l^a) + B_{lm}^a \dot{u}_l^a(r_a, e_l^a)] Y_{lm}(\hat{r}_a), & |r_a| \leq R_{MT}^a \end{cases} \quad (2.4.5)$$

In order to determine the coefficients A_{lm} and B_{lm} , we will require that the function in the sphere matches the plane wave both in value and in slope at the sphere boundary.

In many cases it is desirable to distinguish three types of electronic states, namely core, semi-core and valence states. For example titanium has core (1s, 2s, 2p), semi-core (3s, 3p) and valence (3d, 4s, 4p) states. Core states are defined as only those whose charge is entirely confined inside the corresponding atomic sphere. They are deep in energy, e.g., more than 7-10 Ry below the Fermi energy.

Semi-core states lie high enough in energy (between about 1 and 7 Ry below the Fermi energy), so that their charge is no longer completely confined inside the atomic sphere, but has a few percent outside the sphere. Valence states are energetically the highest (occupied) states and always have a significant amount of charge outside the spheres.

The LAPW basis functions, however, are not suited for treating electronic states that lie far from the linearization energy, such as the semi-core states, that have a principal quantum number one less than the corresponding valence state [41]. In this case, describing two states of the same quantum number l but different principal quantum number n by the same energy parameter e_l , would lead to a poor description for one or both of them. This dilemma is solved by adding another type of basis function to the LAPW basis set, called a *local orbital* (LO). A local orbital (“*local*” in the

sense they are confined exclusively to the muffin-tin region and are identically zero outside the muffin-tin sphere) is defined as

$$f_{lm}^{LO}(\mathbf{r}) = \begin{cases} 0 & r_a \in I \\ \sum_{lm} [A_{lm}^{a,LO} u_l^a(r_a, \mathbf{e}_{l,1}^a) + B_{lm}^{a,LO} u_l^a(r_a, \mathbf{e}_l^a) + C_{lm}^{a,LO} u_l^a(r_a, \mathbf{e}_{l,2}^a)] Y_{lm}^a(\hat{r}), & |r_a| \leq R_{MT}^a \end{cases} \quad (2.4.6)$$

The coefficients A_{lm} , B_{lm} , and C_{lm} are determined by the requirement that f_{lm}^{LO} should be normalized and have zero value and slope at the sphere boundary (it doesn't leak out of the muffin tin sphere). As can be seen from Eq. (2.4.4), the LO is constructed from the LAPW radial function at the linearization energy $e_{l,1}^a$. A third radial function $u_l^a(r_a, \mathbf{e}_{l,2}^a)$, obtained at the second linearization energy $e_{l,2}^a$ was chosen to most efficiently decrease the linearization error.

The overwhelming success of the density functional theory for the description of the ground-state properties of large material classes including insulators, semiconductors, semimetals, half-metals, simple metals, transition metals and rare-earths in bulk, at surfaces and as nanostructures makes it the unchallenged basis of any modern electronic structure theory. The wide applicability combined with the predictive power of the approach turned it to the standard model in material science.

In principle, the only input needed for the theory are the atomic numbers of the main atoms of a system, all other properties follow as a direct result of the density functional equations. In practice, the definition has to be modified since one is always limited to some set of model systems. These limitations might include system size, crystal structure, neglect of disorder,

low or zero temperature, or any number of other boundaries on the phase space to probe. While some of these restrictions and limitations are troublesome, the goal of calculations is not merely to obtain numbers, but rather insight.

By focusing on well-defined, but restricted models, by working on chemical trends rather than on isolated case studies, by investigating systems in imaginary non-equilibrium structures or follow simulations in idealized environments, which may not be realized in experiments, one is able to develop different levels of understanding of the system in question and may hopefully learn which aspects of the problem are important. In the density functional theory many objects have been done in an effective one-particle picture:

The wave functions are solutions of the Kohn-Sham equations and the interaction of the particles is taken into account by a self-consistent field, which depends on the density of the particles. The sufficiency and limitations of this approach have been extensively discussed in the literature and pioneered by [65].

2.4.3 The FP-LAPW Method

In the APW as well as LAPW methods, we assumed that the potential is spherically symmetric within atomic spheres with radius R_m and centered at atomic positions R^a , where the potential is constant in the interstitial region. This approximation works reasonably well in highly coordinated systems, such as close-packed metals, however, it might lead to serious discrepancies compared with experimental measurements for open structures, such as layered structures and surfaces. Therefore, a treatment

where no shape approximation is made for the potential is essential to understand and predict electronic and structural properties of open systems.

The full-potential LAPW method (FP-LAPW) [45] combines the choice of the LAPW basis set with the treatment of the full-potential and charge density without any shape approximations in the interstitial region and inside the muffin-tins. By relaxing the constant interstitial potential r and the spherical muffin-tin approximation $V_{MT}^o(r)$ due to the inclusion of a warped interstitial $\sum V_l^K \exp^{i\vec{K}\cdot\vec{r}}$ and the non-spherical terms inside the muffin-tin spheres its generalization can be achieved as:

$$V_{eff}(\mathbf{r}) = \begin{cases} \sum_{K}^{|\mathbf{K}| \leq K^{pot}} V_{eff}(\mathbf{K}) e^{i\mathbf{K}\cdot\mathbf{r}}, & \mathbf{r} \in I \\ \sum_{lm}^{l \leq l_{max}} V_{eff}^{lm}(\mathbf{r}_a) Y_{lm}(\hat{\mathbf{r}}_a), & |\mathbf{r}_a| \leq R_{MT} \end{cases} \quad (2.4.7)$$

where K^{pot} determines the highest reciprocal lattice vector included in the sum, which are used to describe the potential in the interstitial region, while l_{max} determines the size of the (l, m) representation to describe the potential inside the atomic sphere [41]. By increasing these values, the quality of the full-potential description can be improved systematically. These are values, which should be carefully tested, to determine an optimal basis set for a calculation.

This method became possible with the development of a technique for obtaining the Coulomb potential for a general periodic charge density

without shape-approximations and with the inclusion of the Hamiltonian matrix elements due to the warped interstitial and non-spherical terms of the potential. The charge density ρ is represented analogously to Eq.(2.4.7), just exchanging V by ρ . Details of the solution of the Poisson equation for an arbitrarily shaped periodic potential are described in many references [66, 67, 68]. The program used in this work, is WIEN2K, based on the FP-LAPW method will be the subject of the next section.

2.5 The Wien2k Program

The calculations presented in this work are performed with the program package WIEN2K. The program package WIEN2K allows performing electronic structure calculations of solids using density functional theory (DFT). It is based on the full-potential (linearized) augmented plane-wave method, one among the most accurate schemes for band structure calculations. In DFT the local (spin) density approximation (LDA) or the improved version of the generalized gradient approximation (GGA) can be used. A flow chart of the program is shown in Fig. 2.3. The program is divided mainly into two parts, initialization and main program (self-consistent cycle). Each of them is divided into sub-programs, connected by scripts.

In the initialization, the geometric and electronic structure of the system of interest is set up. The symmetry of the system and the k-points, which will be used, are determined. During initialization the electron densities of free atoms are calculated and superposed to get an initial guess for the charge density used in the self-consistent cycle.

In the main program, a potential is generated from the input charge density, which in turn builds up the Hamiltonian used to solve the eigenvalue problem for the valence electrons. As a result, a new valence electron density is obtained from the calculated eigen functions. On the other hand, the core electrons energy and densities are determined by a fully-relativistic self-consistent calculation in the crystal potential. The two densities (valence and core) are mixed with the old density using a Broyden mixing scheme to obtain the new density. Convergence is reached, when old and new electron densities are within computational tolerance.

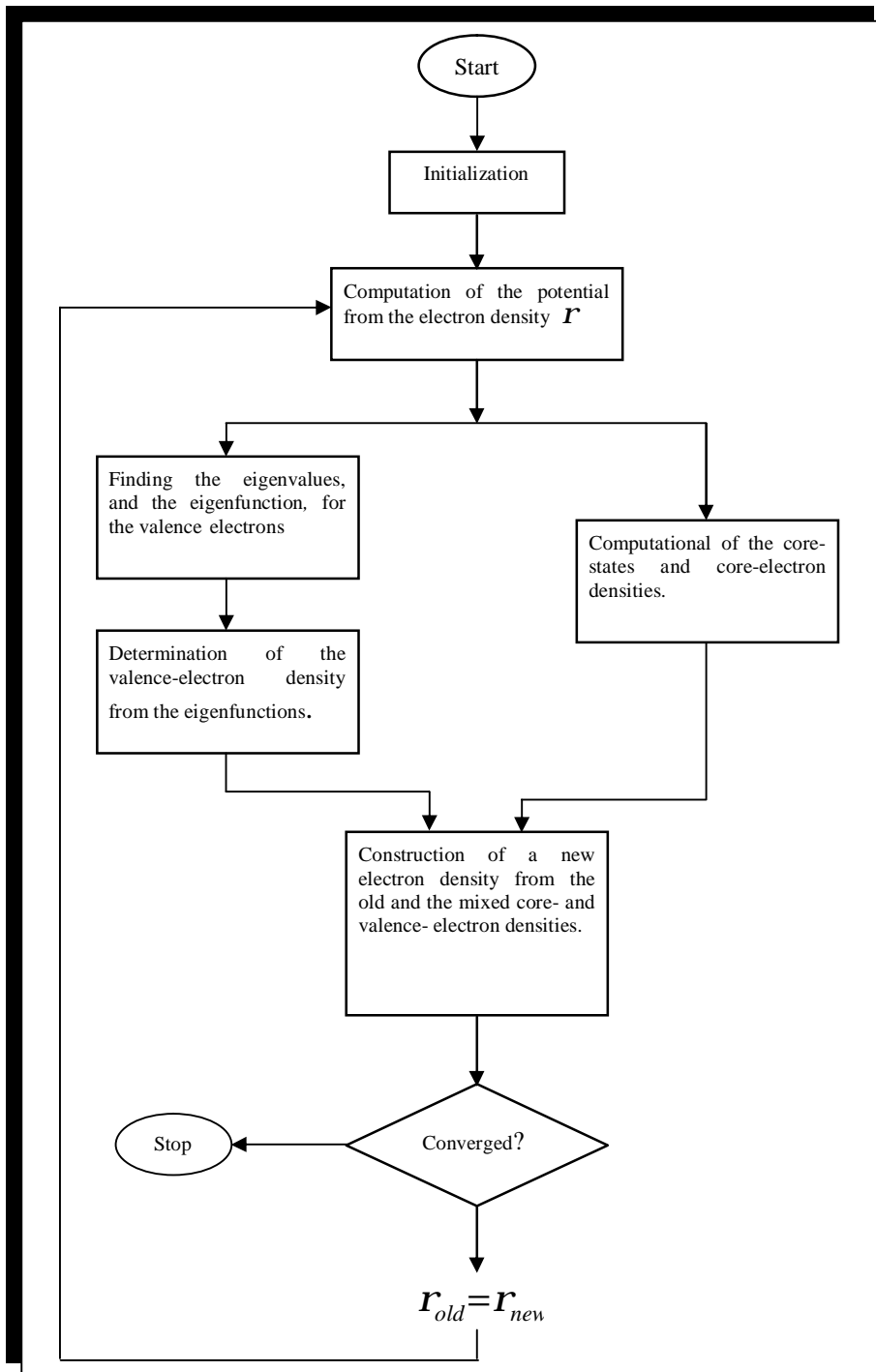


Fig. 2.3: Flowchart of the Wien2k program.

Chapter Three

Results and Discussion

When dealing with supercells and studying the properties of the alloys, especially their magnetic properties, it is important to remember that supercell is connected to the bulk. This means that characteristic features of the bulk material will probably have a strong influence on the supercell properties and behavior. For example, the lattice constants for bulk material are very important to build up the supercell.

Calculating the bulk properties for the binary and ternary alloys for the system of interest must be made after applying some tests. k-points and Energy cutoff tests are very important procedures to get best results in short time.

In the following section we present the systematic convergence tests for the systems of interest. The calculated bulk properties of the binary compounds GaN, MnN as well as the ternary $Ga_{1-x}Mn_xN$ alloys are presented in the second section. Section three, which is one of the most important parts in these results, contains the bulk as well as magnetic results for the ternary alloys, by using the FP-LAPW method as implemented by the WIEN2K program package. The procedure for calculating the equilibrium lattice parameters will also be discussed for every material.

3.1 Convergence Tests

The results as well as the running time depend on some input factors. In order to obtain reliable calculations, one has to perform some convergence

tests to optimize the input parameters with respect to time and accuracy.

The parameters, which have to be tested, are mainly:

- I- *K-points*: the number of necessary irreducible k-points in the (BZ) is needed to obtain accurate self-consistent potential, total energy, structural properties, magnetic moments...etc.
- II- $R_{MT} \cdot K_{max}$ and *Energy cutoff*: in the interstitial region, a plane wave expansion of the wave function and the potential should be done. Ideally, one should use an infinite set of plane waves. Since this is impossible in practice, a reasonable truncation is required.

In this work, the convergence tests are performed for determining the equilibrium lattice constants for the two compounds GaN and MnN. For GaN calculations, the lattice constants $a = 4.35 \text{ \AA}$ and $a = 4.34 \text{ \AA}$ are performed as trial values for LSDA and GGA respectively, for the k-points as well as the cutoff energy convergence tests [15]. The purpose of that is to achieve the minimum energies. However, for the MnN calculations, the trial values of the lattice constants that have been performed are $a_{LSDA} = 4.383 \text{ \AA}$ and $a_{GGA} = 4.175 \text{ \AA}$. It is to be noted here that a muffin tin radii R_{MT} of 1.78 bohr is used for Ga and Mn, while 1.6 bohr for N in order to insure that the spheres do not overlap.

3.1.1 k-Points Test

In the k-points test, the initial cutoff $R_{MT} \cdot K_{max}$ used is 8.5 (where R_{MT} is the average radius of the muffin-tin spheres and K_{max} is the maximum modulus for the reciprocal lattice vector). The maximum value of l for the wave function expansion inside the atomic spheres is confined to $l_{max} = 10$. The

total number of k-points is increased in the total BZ in a way that the Monkhorst-Pack grids go successfully with values of K_{mesh} as shown in Tables 3.1 and 3.2. The total energy dependence on the k-points at the lattice constants are also displayed.

Table 3.1: *K-Points test at initial cutoff energy 13.5 Ry = 183.7 eV for GaN in ZB structure.*

$K_{\text{tot.}}$	K_{mesh}	$K_{\text{irred.}}$	E_{LSDA} (eV)	E_{GGA} (eV)
8	2×2×2	3	-3991.38579	-3997.68991
27	3×3×3	5	-3991.49267	-3997.79226
64	4×4×4	10	-3991.5108	-3997.81016
125	5×5×5	14	-3991.51451	-3997.81347
216	6×6×6	22	-3991.51539	-3997.81427
343	7×7×7	30	-3991.51557	-3997.81438
512	8×8×8	43	-3991.5156	-3997.81344
729	9×9×9	55	-3991.51565	-3997.81332
1000	10×10×10	73	-3991.51562	-3997.81335

Table 3.2: *k-Points test at initial cutoff energy 14.5 Ry = 197.345 eV for MnN in ZB structure.*

$K_{\text{tot.}}$	K_{mesh}	$K_{\text{irred.}}$	E_{LSDA} (eV)	E_{GGA} (eV)
8	2×2×2	3	-2421.88391	-2426.84976
27	3×3×3	5	-2421.89546	-2426.85873
64	4×4×4	10	-2421.89547	-2426.86199
125	5×5×5	14	-2421.89553	-2426.86969
216	6×6×6	22	-2421.89952	-2426.86871
343	7×7×7	30	-2421.8997	-2426.87505
512	8×8×8	43	-2421.89945	-2426.87658
729	9×9×9	55	-2421.89961	-2426.87676
1000	10×10×10	73	-2421.89955	-2426.87645

For the $Ga_{1-x}Mn_xN$ ternary alloys, the energy dependence on the k- point is tested. The initial cutoff energy used is $13.5 \text{ Ry} = 183.735 \text{ eV}$. The total number of k-points is increased from 27 to 1000 in the total BZ in a way that Monkhorst-pack grids go successfully from $3 \times 3 \times 3$ up to $10 \times 10 \times 10$. In the irreducible wedge, this corresponds to an increase from 5 to 70 points, as shown in Tables 3.3 and 3.4.

Table 3.3: *k*-Points tests for $Ga_{1-x}Mn_xN$ at initial cutoff energy $13.5 \text{ Ry} = 183.7 \text{ eV}$.

$K_{\text{tot.}}$	K_{mesh}	$K_{\text{irred.}}$	$E_{\text{LSDA}} \text{ (eV)}$	$E_{\text{GGA}} \text{ (eV)}$
<i>Ga_{0.875}Mn_{0.125}N</i>				
27	$3 \times 3 \times 3$	5	-121442.5832	-121638.1537
64	$4 \times 4 \times 4$	8	-121442.7996	-121638.3086
125	$5 \times 5 \times 5$	14	-121442.8142	-121638.3125
216	$6 \times 6 \times 6$	20	-121443.0159	-121638.3236
343	$7 \times 7 \times 7$	30	-121442.824	-121638.3516
512	$8 \times 8 \times 8$	40	-121442.8244	-121638.3237
729	$9 \times 9 \times 9$	55	-121442.8246	-121638.3391
1000	$10 \times 10 \times 10$	70	-121442.8243	-121638.3235
<i>Ga_{0.75}Mn_{0.25}N</i>				
27	$3 \times 3 \times 3$	5	-14396.21533	-14420.22805
64	$4 \times 4 \times 4$	8	-14396.24353	-14420.22807
125	$5 \times 5 \times 5$	14	-14396.27648	-14420.22812
216	$6 \times 6 \times 6$	20	-14396.28519	-14420.22901
343	$7 \times 7 \times 7$	30	-14396.29935	-14420.22907
512	$8 \times 8 \times 8$	40	-14396.29932	-14420.22907
729	$9 \times 9 \times 9$	55	-14396.29885	-14420.22907
1000	$10 \times 10 \times 10$	70	-14396.29893	-14420.22907

As a consequence of the total energy versus $K_{\text{irred.}}$, plot for all of the concentrations that have been taken, Figure 3.3-a, b for $x = 0.125$, Figure

3.4-a, b for $x = 0.25$, Figure 3.5-a, b for $x = 0.50$, Figure 3.6-a, b for $x = 0.75$. It is found the $K_{\text{irred.}}$ and K_{mesh} that is sufficient to perform the calculations for LSDA and GGA are summarized in Table 3.5.

Table 3.4: *k*-Points tests for $\text{Ga}_{1-x}\text{Mn}_x\text{N}$ at initial cutoff energy $13.5 \text{ Ry} = 183.6 \text{ eV}$.

$K_{\text{tot.}}$	K_{mesh}	$K_{\text{irred.}}$	$E_{\text{LSDA}} \text{ (eV)}$	$E_{\text{GGA}} \text{ (eV)}$
<i>Ga_{0.5}Mn_{0.5}N</i>				
27	3×3×3	5	-12826.60601	-12849.23516
64	4×4×4	8	-12826.69866	-12849.23717
125	5×5×5	14	-12826.70409	-12849.23908
216	6×6×6	20	-12826.70409	-12849.23895
343	7×7×7	30	-12826.70305	-12849.23889
512	8×8×8	40	-12826.70311	-12849.23889
729	9×9×9	55	-12826.70304	-12849.23886
1000	10×10×10	70	-12826.70301	-12849.23889
<i>Ga_{0.25}Mn_{0.75}N</i>				
27	3×3×3	5	-11257.21533	-12278.22737
64	4×4×4	8	-11257.24353	-12278.22788
125	5×5×5	14	-11257.27648	-12278.22812
216	6×6×6	20	-11257.28519	-12278.22832
343	7×7×7	30	-11257.29935	-12278.22839
512	8×8×8	40	-11257.29932	-12278.22907
729	9×9×9	55	-11257.29885	-12278.22897
1000	10×10×10	70	-11257.29893	-12278.22895

Table 3.5: The final $K_{irred.}$ and $K_{mesh.}$ that is sufficient to perform the calculations at initial cutoff energy $13.5 \text{ Ry} = 183.735 \text{ eV}$ for $\text{Ga}_{1-x}\text{Mn}_x\text{N}$ in ZB structure.

K_{mesh}^{LSDA}	K_{mesh}^{GGA}	$K_{irred.}^{LSDA}$	$K_{irred.}^{GGA}$	Concentration
$6 \times 6 \times 6$	$7 \times 7 \times 7$	20	30	0.125
$7 \times 7 \times 7$	$8 \times 8 \times 8$	30	40	0.25
$6 \times 6 \times 6$	$5 \times 5 \times 5$	20	14	0.5
$7 \times 7 \times 7$	$8 \times 8 \times 8$	30	40	0.75

As a consequence of the total energy versus $K_{irred.}$ plot for both lattice constants, Figure 3.1-a for $a = 4.35 \text{ \AA}$ by LSDA method and Figure 3.1-b for $a = 4.34 \text{ \AA}$ by GGA method for the GaN. Figures 3.1-a and 3.1-b predict that $7 \times 7 \times 7$ (i.e. $K_{irred.} = 30$), are sufficient to perform the calculations for GaN. While Figures 3.2-a and 3.2-b predict that $9 \times 9 \times 9$ ($K_{irred.} = 55$) is sufficient for MnN.

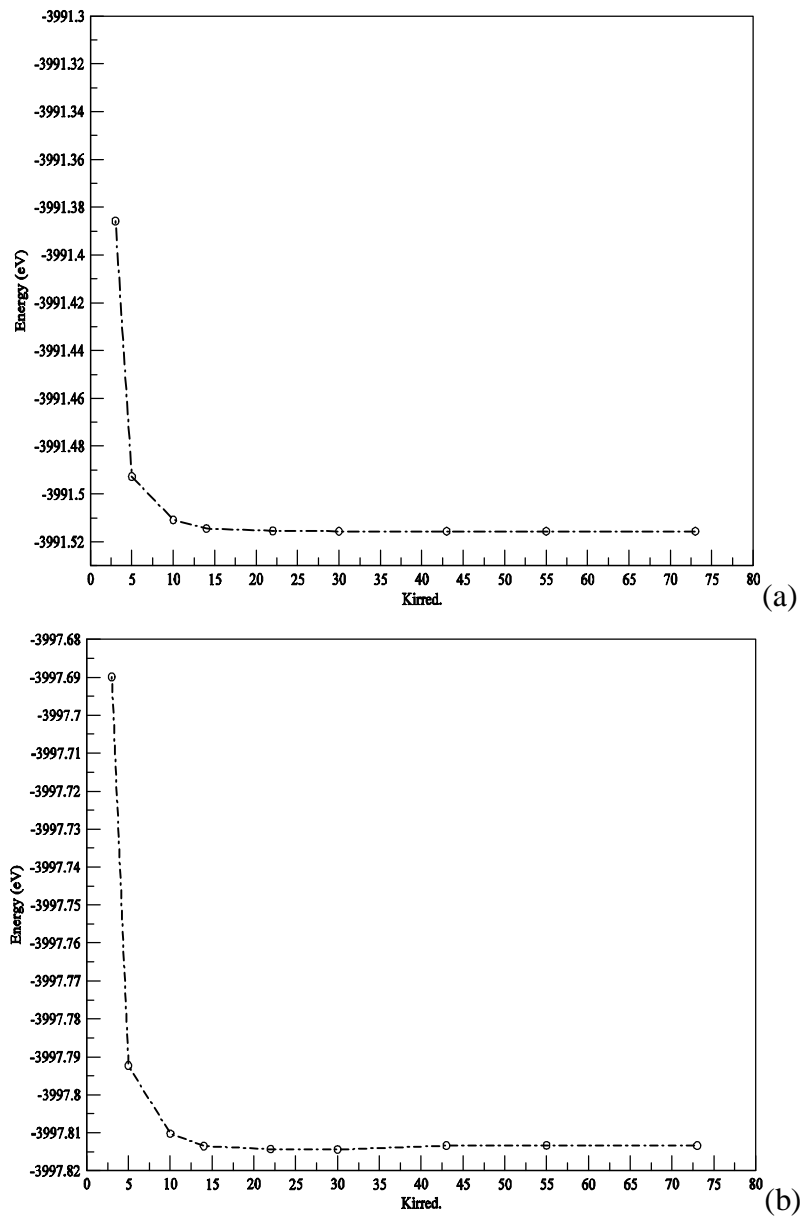


Figure 3.1: *GaN k-Points Test in the ZB-structure by (a) LSDA, (b) GGA Approximation methods.*

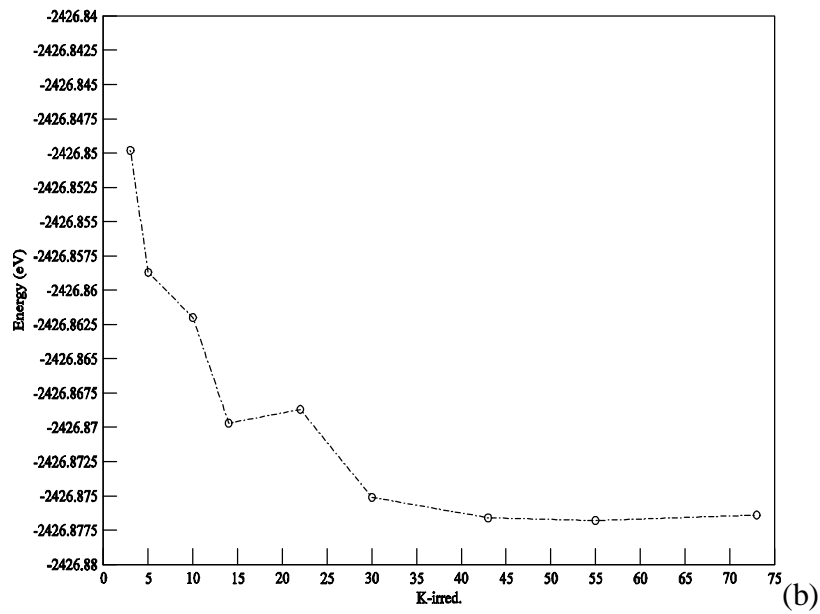
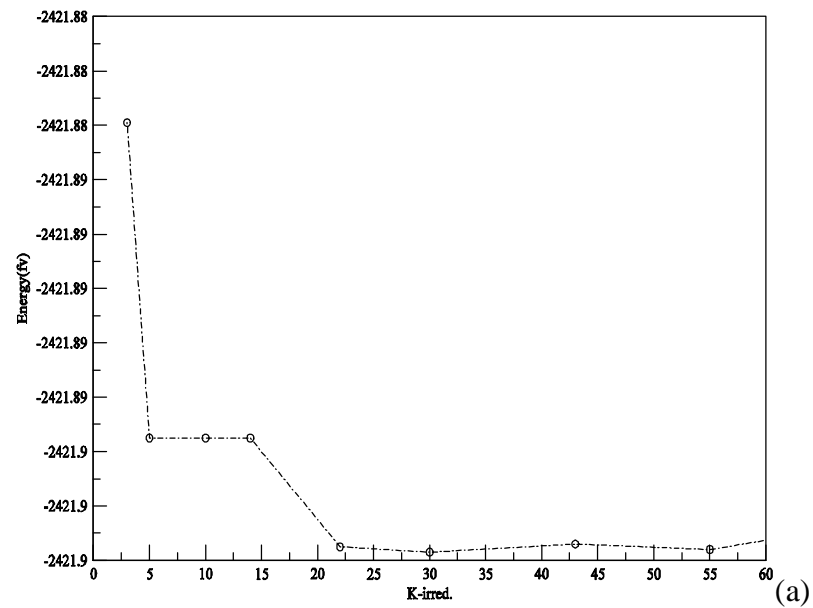
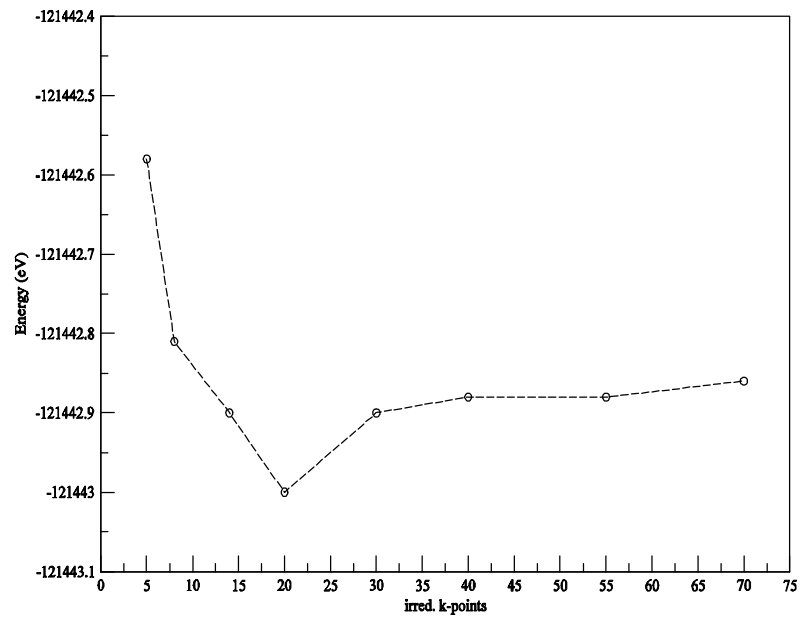
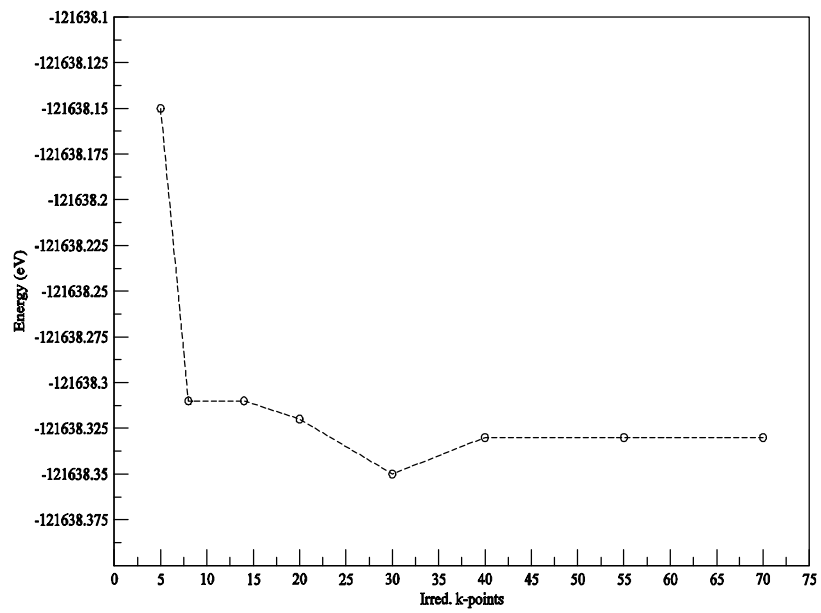


Figure 3.2: *MnN* *k*-Points Test in the ZB-structure by (a) LSDA, (b) GGA Approximation methods.



(a)



(b)

Figure 3.3: *k*-Points tests for $\text{Ga}_{1-x}\text{Mn}_x\text{N}$ with composition $x = 0.125$ in the ZB-structure using: a) LSDA method and b) GGA method.

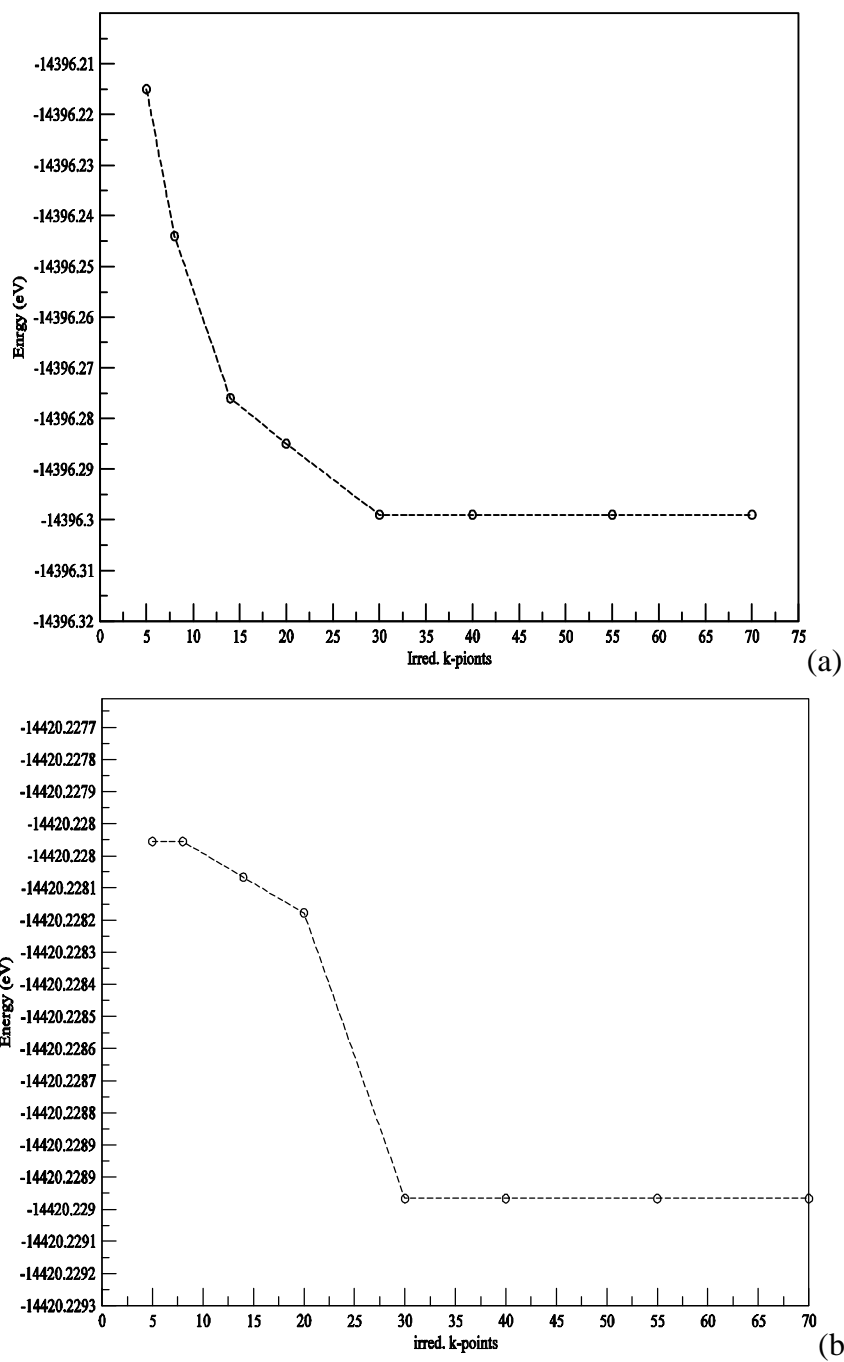


Figure 3.4: *k*-Points tests for $\text{Ga}_{1-x}\text{Mn}_x\text{N}$ with composition $x = 0.25$ in the ZB structure using: a) LSDA method and b) GGA method.

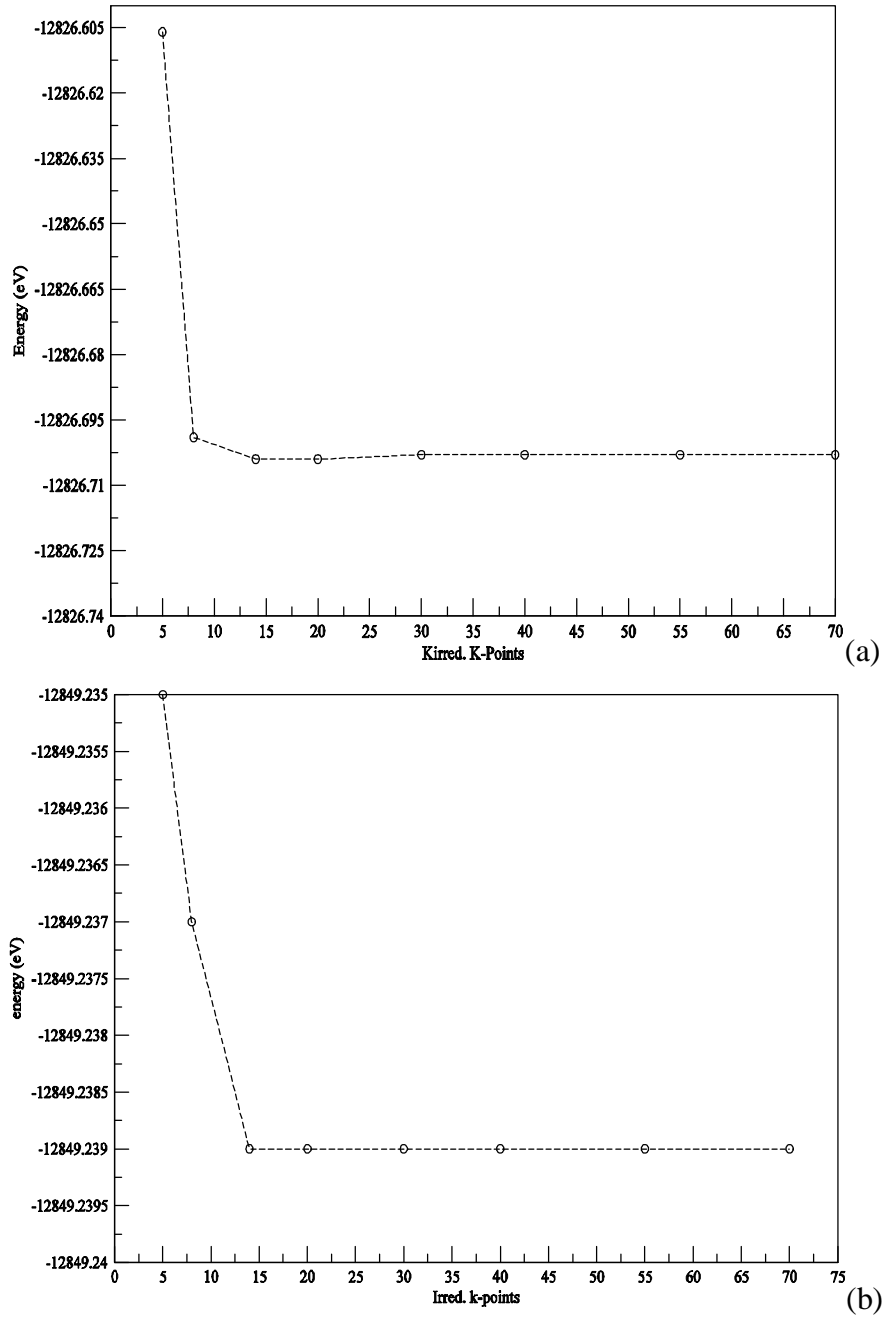


Figure 3.5: *k*-Points tests for $\text{Ga}_{1-x}\text{Mn}_x\text{N}$ with composition $x = 0.5$ in the ZB structure using: a) LSDA method and b) GGA method.

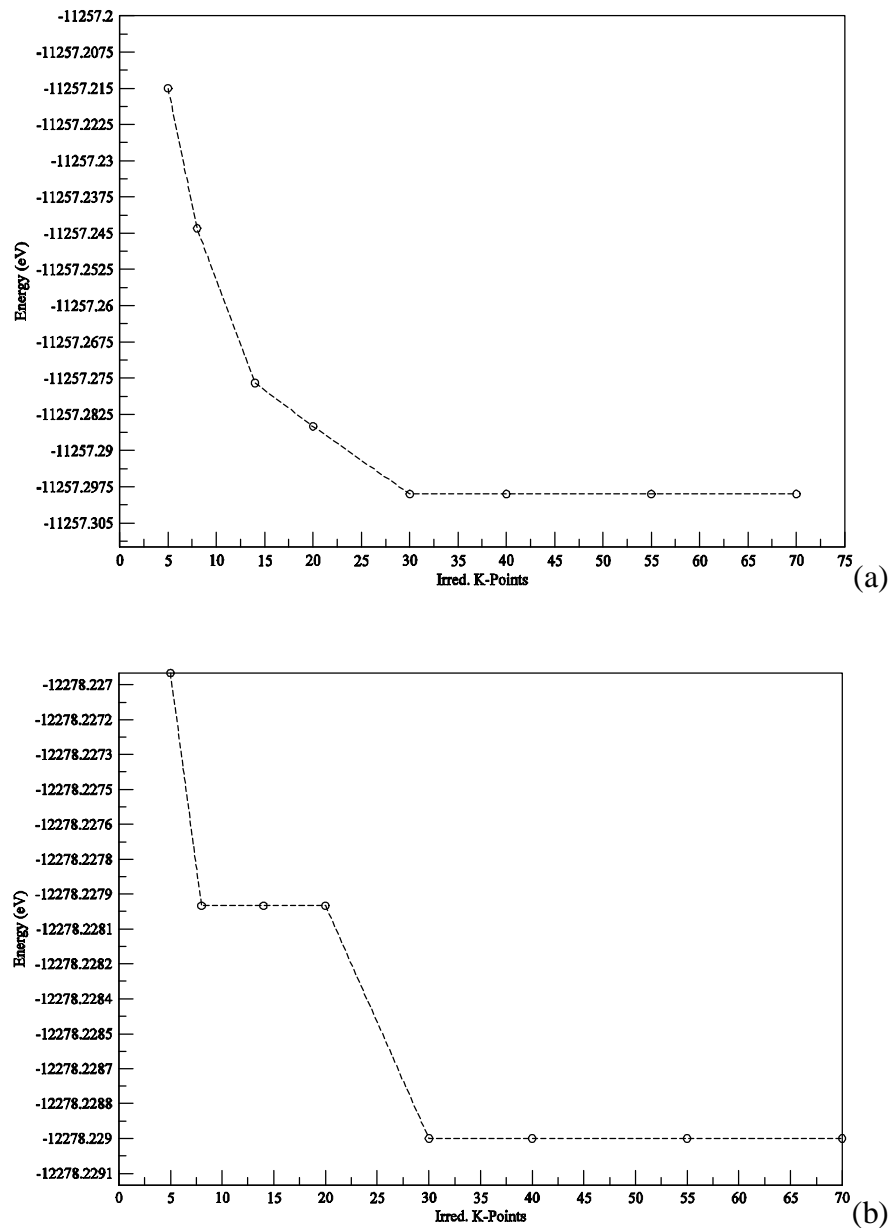


Figure 3.6: *k*-Points tests for Ga_{1-x}Mn_xN with composition $x = 0.75$ in the ZB structure using : a) LSDA method and b) GGA methods.

3.1.2 R_{MT}.K_{max} Cutoff Test

In this test, the total energy dependence on the cutoff energy is checked.

Calculations for GaN are performed for the two lattice constants mentioned before with $K_{\text{irred.}} = 30$. On the other hand, $K_{\text{irred.}}$ is taken to be 55 for MnN

cutoff test. The total energy dependence on the $R_{MT} \cdot K_{max}$ cutoff is displayed in Tables 3.6 and 3.7 for both GaN and MnN compounds respectively with the two lattice constants mentioned before.

Table 3.6: $R_{MT} \cdot K_{max}$ cutoff test at initial cutoff energy $13.5 \text{ Ry} = 183.7 \text{ eV}$ for GaN in ZB structure.

$R_{MT} \cdot K_{max}$	E_{tot}^{LSDA} (eV)	E_{tot}^{GGA} (eV)
6	-3991.43250	-3997.72931
6.5	-3991.47880	-3997.77550
7	-3991.50086	-3997.79759
7.5	-3991.51104	-3997.80952
8	-3991.51561	-3997.81493
8.5	-3991.51756	-3997.81698
9	-3991.51840	-3997.81708
9.5	-3991.51852	no convergence

Table 3.7: $R_{MT} \cdot K_{max}$ cutoff test at initial cutoff energy $14.5 \text{ Ry} = 197.345 \text{ eV}$ for MnN in ZB structure.

$R_{MT} \cdot K_{max}$	E_{tot}^{LSDA} (eV)	E_{tot}^{GGA} (eV)
6	-2421.831606	-2426.812419
6.5	-2421.870363	-2426.849433
7	-2421.887429	-2426.868827
7.5	-2421.895003	-2426.876584
8	-2421.898001	-2426.880173
8.5	-2421.899687	-2426.882175
9	-2421.899904	-2426.883159
9.5	-2421.900380	-2426.883211

As a consequence of the total energy versus $R_{MT} \cdot K_{max}$ cutoff, plot for both GaN lattice constants is shown in Figure 3.7-(a, b) for $a_{LSDA} = 4.35 \text{ \AA}$ and

$a_{GGA} = 4.34 \text{ \AA}$, respectively. It is found that the $R_{MT} \cdot K_{max}$ cutoff of 9 is sufficient to perform the calculations for LSDA, while for GGA it is found to be 8.5. Figures 3.8-(a, b) show the stability of states of the MnN compound in the ZB structure using the LSDA and GGA approximations. It is found that the $R_{MT} \cdot K_{max}$ cutoff of 9 is sufficient to perform the calculations for LSDA and GGA methods.

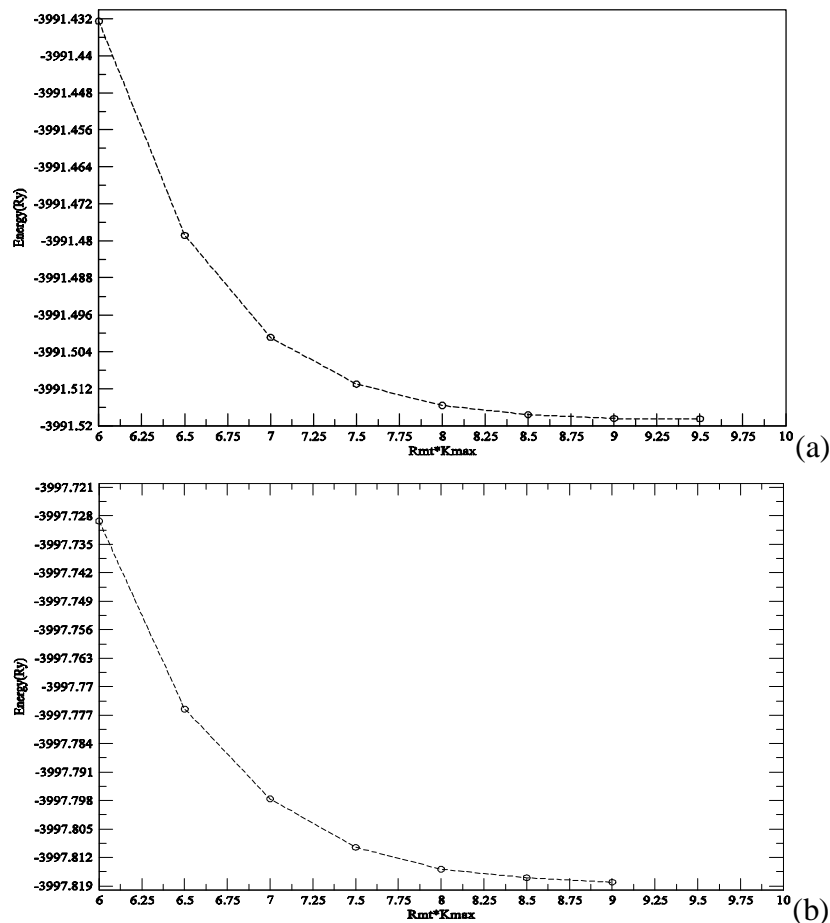


Figure 3.7: $R_{MT} \cdot K_{max}$ Cutoff test for GaN by: a) LSDA and b) GGA approximation methods.

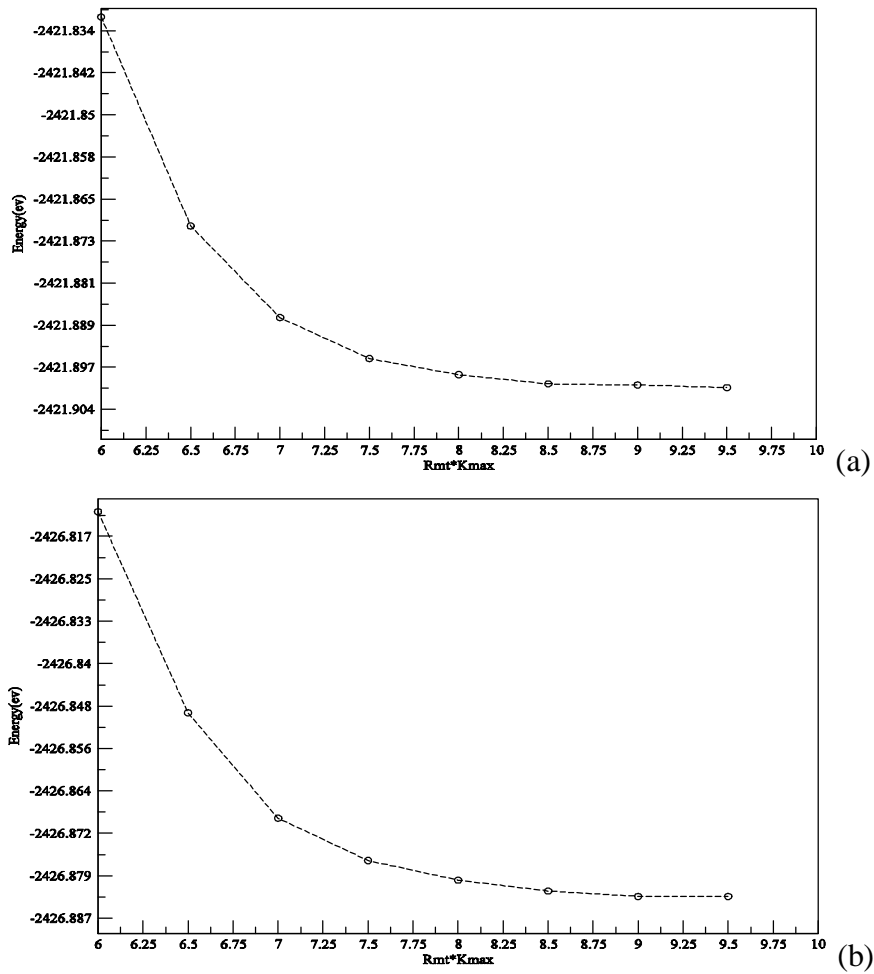


Figure 3.8: $R_{MT} \cdot K_{max}$ Cutoff test for MnN by: a) LSDA approximation, b) GGA approximation methods.

For $Ga_{1-x}Mn_xN$ ternary alloys, the $R_{MT} \cdot K_{max}$ tests have been made carefully. The total energy dependence on the $R_{MT} \cdot K_{max}$ cutoff is displayed in Tables 3.8, 3.9 for all of the concentrations that have been studied.

Table 3.8: $R_{\text{MT}} \cdot K_{\text{max}}$ tests for $\text{Ga}_{1-x}\text{Mn}_x\text{N}$ at initial cutoff energy $13.5 \text{ Ry} = 183.7 \text{ eV}$.

$R_{\text{MT}} \cdot K_{\text{max}}$	$E_{\text{tot.}}^{\text{LSDA}}$ (eV)	$E_{\text{tot.}}^{\text{GGA}}$ (eV)
<i>Ga0.875Mn0.125N</i>		
6	-121442.7958	-121638.2615
6.5	-121442.8515	-121638.3248
7	-121442.8572	-121638.3287
7.5	-121442.8592	-121638.5291
8	-121442.8649	-121638.5315
8.5	-121443.8648	-121638.6485
9	-121443.8645	-121638.6548
9.5	-121443.8646	-121638.6544
<i>Ga0.75Mn0.25N</i>		
6	-14396.30158	-14419.911760
6.5	-14396.32425	-14420.085370
7	-14396.32742	-14420.172130
7.5	-14396.32927	-14420.210250
8	-14396.33579	-14420.229070
8.5	-14396.33658	-14420.235170
9	-14396.33575	-14420.238630
9.5	-14396.33576	-14420.238252

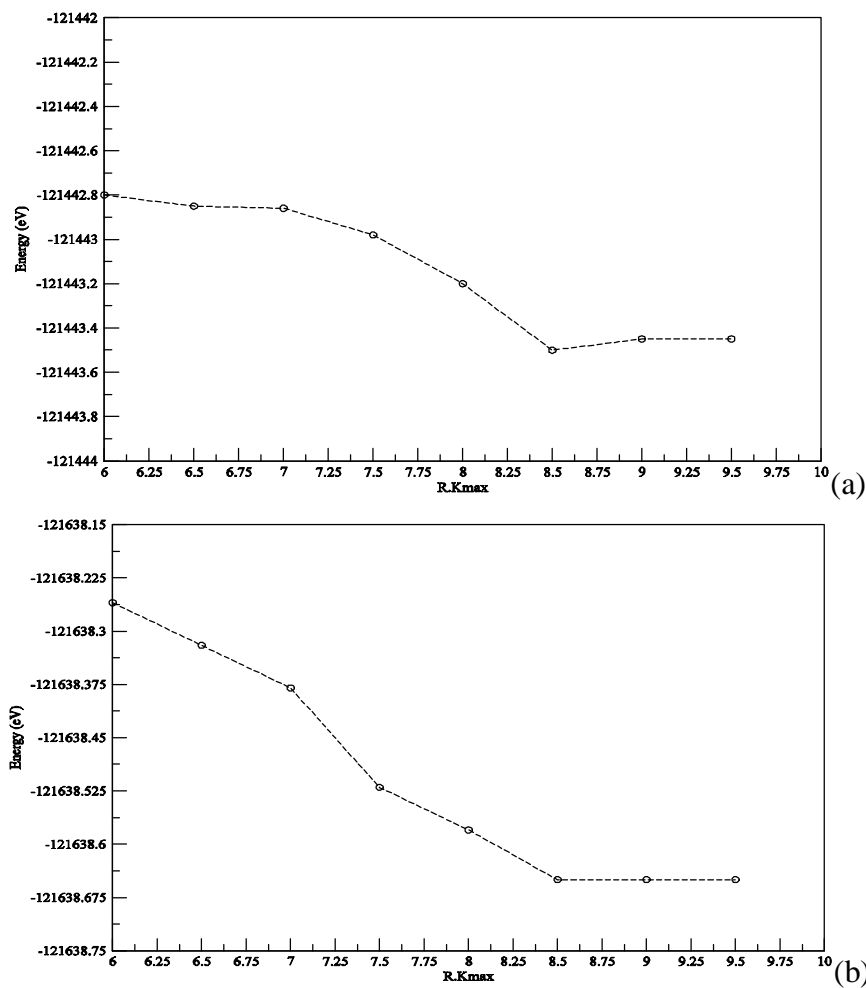
Table 3.9: $R_{MT}.K_{max}$ tests for $Ga_{1-x}Mn_xN$ at initial cutoff energy $13.5 Ry = 183.7 eV$.

$R_{MT}.K_{max}$	E_{tot}^{LSDA} (eV)	E_{tot}^{GGA} (eV)
<i>Gao.5Mno. 5N</i>		
6	-12826.405072	-12849.204706
6.5	-12826.574245	-12849.242738
7	-12826.653314	-12849.242915
7.5	-12826.687818	-12849.242993
8	-12826.702998	-12849.243472
8.5	-12826.702548	-12849.243829
9	-12826.702295	-12849.243317
9.5	-12826.702274	-12849.243377
<i>Gao.25Mno. 75N</i>		
6	-11256.923356	-11277.95176
6.5	-11257.086508	-11278.08217
7	-11257.154713	-11278.10213
7.5	-11257.190213	-11278.11053
8	-11257.203984	-11278.13027
8.5	-11257.209912	-11278.13047
9	-11257.211883	-11278.13043
9.5	-11257.211795	-11278.13012

From Figures (3.9 - 3.12), it is found the $R_{MT}.K_{max}$ cutoff that is sufficient to perform the calculations for LSDA and GGA are displayed in Table 3.10

Table 3.10: $R_{MT} \cdot K_{max}$ cutoff test at initial cutoff energy $13.5 \text{ Ry} = 183.7 \text{ eV}$ for $\text{Ga}_{1-x}\text{Mn}_x\text{N}$ in ZB structure.

$R_{MT} \cdot K_{max}$	$R_{MT} \cdot K_{max}$	Concentration
8.5	9	0.125
8.5	9	0.25
8	8.5	0.50
8.5	8.5	0.75
LSDA	GGA	

**Figure 3.9:** $R_{MT} \cdot K_{max}$ tests for $\text{Ga}_{1-x}\text{Mn}_x\text{N}$ with composition $x = 0.125$ in the ZB

structure using: a) LSDA method and b) GGA method.

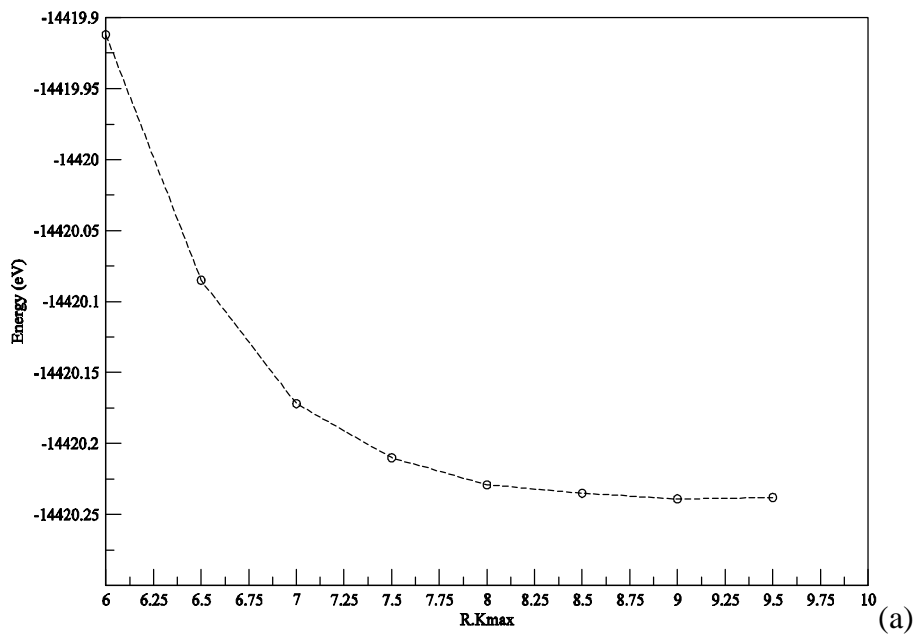
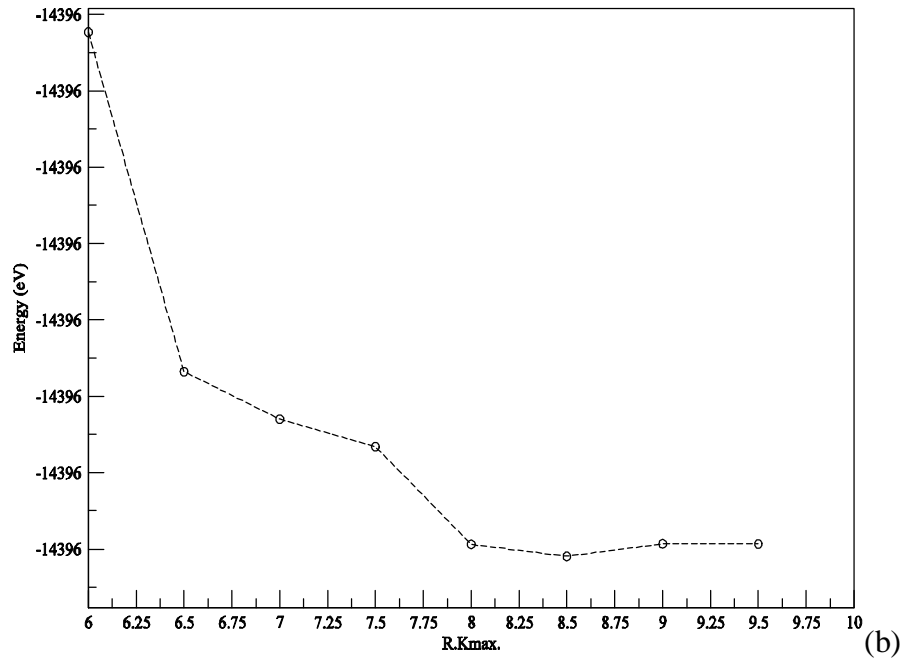


Figure 3.10: $R_{MT} \cdot K_{max}$ tests for $Ga_{1-x}Mn_xN$ with composition $x = 0.25$ in the ZB structure using: a) LSDA method and b) GGA method.

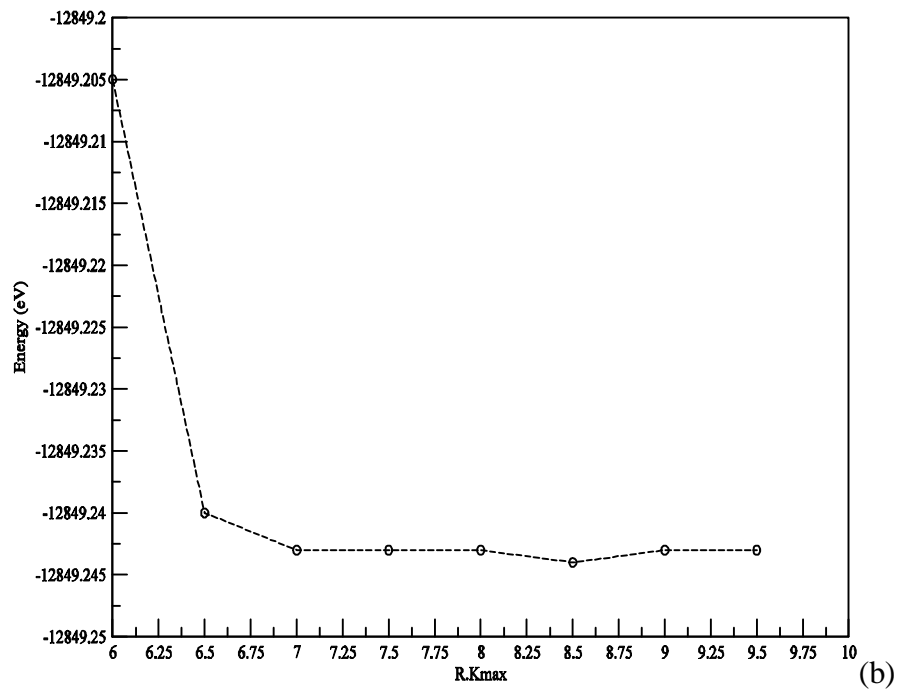
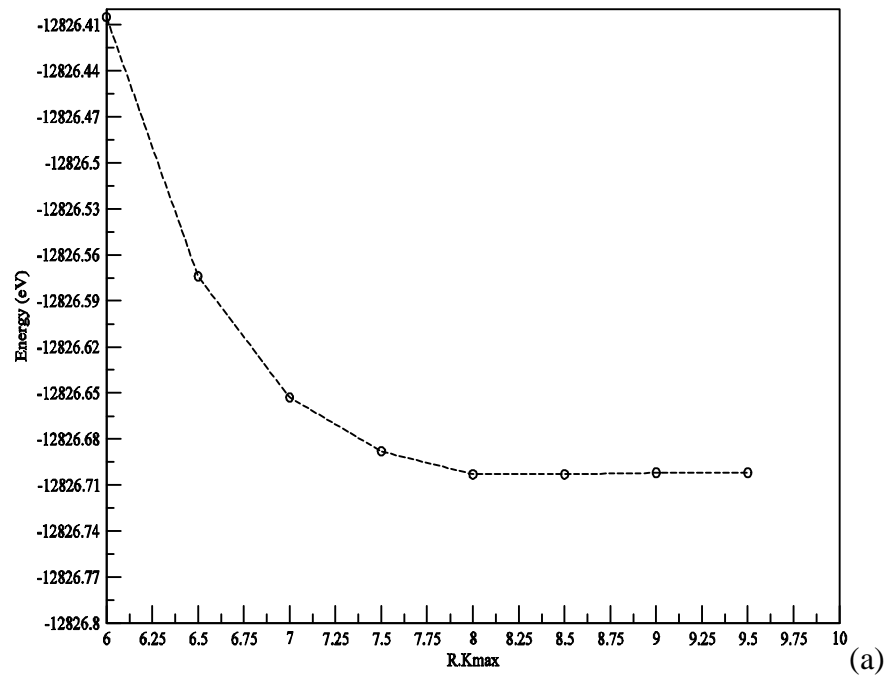


Figure 3.11: $R_{MT} \cdot K_{max}$ tests for $Ga_{1-x}Mn_xN$ with composition $x = 0.5$ in the ZB structure using: a) LSDA method and b) GGA method.

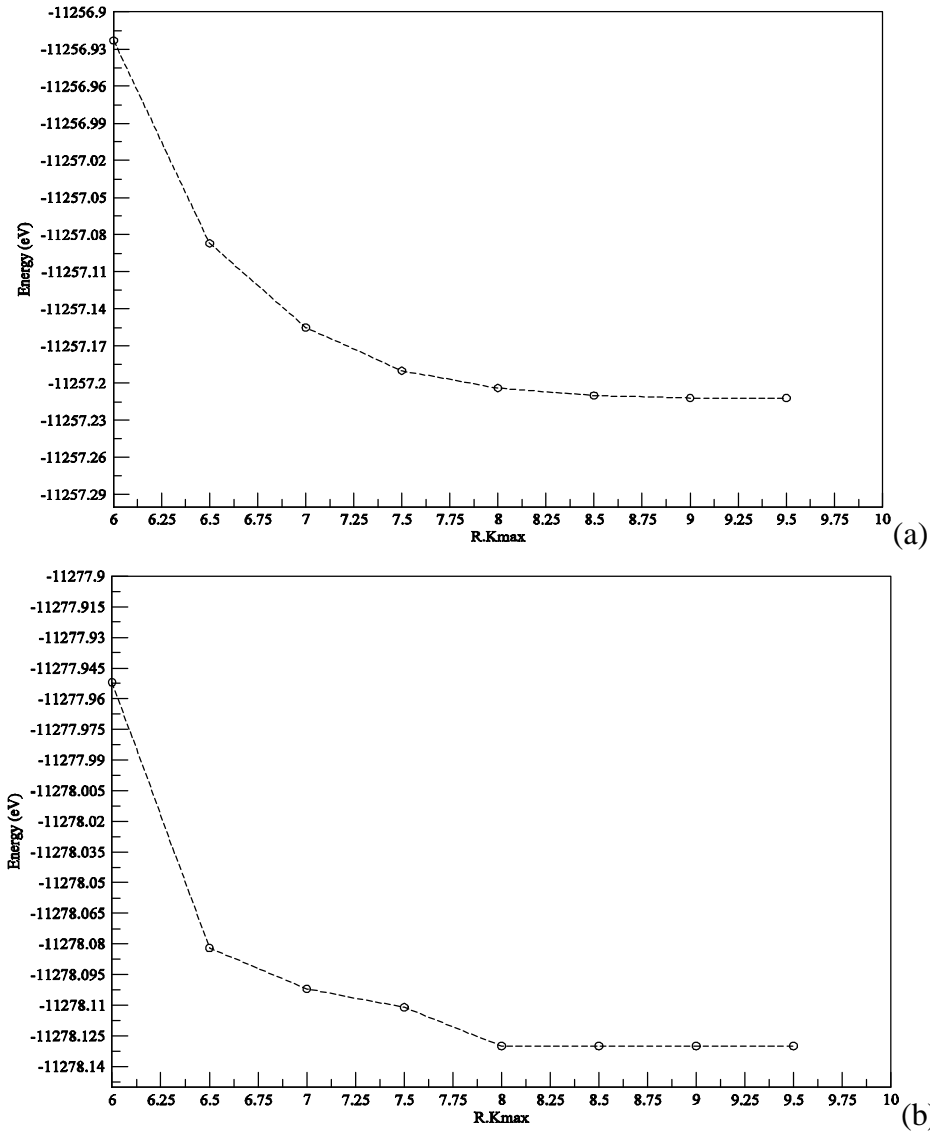


Figure 3.12: $R_{MT}-K_{max}$ tests for $Ga_{1-x}Mn_xN$ with composition $x = 0.75$ in the ZB structure using: a) LSDA method and b) GGA method.

3.2 GaN, MnN Bulk Properties

In this section, only the final results for the equilibrium lattice constants and bulk moduli will be discussed. The procedure for calculating the

equilibrium lattice constants as well as the systematic convergence tests will be discussed in the following section.

In order to study the properties of GaN we must first determine the equilibrium lattice constant for this material in the ZB structure. Table 3.11 summarizes the calculated lattice constants, bulk moduli (B) and the first derivative of the bulk modulus (B') for the GaN compound (after performing the convergence tests), and compare them with other theoretical and experimental results. Comparing these results with the experimental, an error percentage can be calculated to be between 0.008 for GGA to 0.016 for LSDA calculations for the equilibrium lattice constants, so for the optimized bulk modulus, the error have been calculated to be 0.064 for LSDA and 0.186 for the GGA calculations.

Table 3.11: *Calculated and experimental structural parameters of GaN at equilibrium in the ZB structure, 1 and 2 superscript numbers means for the LDA and GGA, respectively.*

Present Calculations		Experiment	Other Calculations
$a_{eq.} (A^\circ)$	LSDA	(4.49-4.52) f , 4.53 c	4.475 $a1$, 4.55 $b2$, 4.46 $d1$, 4.47 $b1$, 4.552 $e2$
	GGA		
B(GPa)	202.9	190 f	175 $b2$ 207 a , 202 $d1,e1$, 208 $b1$, 171 $e2$
B'	4.686		4.32 $d1$, 4.64 $b1$, 5.3 $b2$

a : Ref.[69, 65], b : Ref.[15], c : Ref.[68], d : Ref.[12], e : Ref.[71, 11], f : Ref.[10, 14].

Although the ZB is not the ground-state structure for MnN material [72,73], we are interested to study it in the ZB structure, since in the ZB

structure the Mn atoms find the same local environment as in diluted alloys. Therefore, Table 3.12 summarizes the equilibrium bulk parameters for MnN compound in the ZB phase.

Table 3.12: *Calculated and experimental structural parameters of MnN at equilibrium in the ZB structure.*

Present Calculations			Other Calculations	
	LSDA	GGA	LSDA	GGA
$a_{eq.} (A^\circ)$	4.187	4.309	4.19 ^a	4.3 ^a , 4.378 ^b , 4.34 ^c
B(GPa)	329.578	273.186	336 ^a	271 ^a
B'	4.948	4.4997	--	--

a: Ref.[75], b : Ref.[76], c : Ref.[77]

It is worth noting that the results obtained using LSDA and GGA methods for both GaN and MnN agree very well with the experimental values and other theoretical calculations reported in Table 3.11 and Table 3.12. So far, to the best of our knowledge, no experimental data have been reported for B' regarding GaN and MnN in the ZB phase. However, as compared to other calculations, it appears that our results are close to those reported in References.[12,13,16,72,75,76,77].

3.2.1 Optimization procedure of the lattice constants for GaN and MnN

To determine the equilibrium lattice constants for GaN in the ZB structure by LSDA approximation, the volume of the cell is varied from 135 (a.u.)^3 to 180 (a.u.)^3 ($\text{a.u} = 0.529177 \text{ \AA}^\circ$) as shown in Figure 3.13-a, while for GGA it has been taken to be varied from 137 (a.u.)^3 to 173 (a.u.)^3 as shown in Figure 3.13-b. The optimized number of k-points ($K_{\text{ired.}} = 30$) for the two cases, and $R_{\text{MT}} \cdot K_{\text{max}}$ cutoff of 8 are used for LSDA, while it was 8.5 for GGA calculations. The equilibrium values are obtained using a Murnaghan equation of state fit. [85]. For GaN, it is found that the minimum energy occurs at a lattice constant $a = 4.46 \text{ \AA}^\circ$ and 4.56 \AA° by LSDA and GGA methods respectively. The lattice constants have been found by LSDA and GGA methods for MnN are 4.187 \AA° and 4.309 \AA° respectively. The range of the volume to vary was 118 (a.u.)^3 to 155 (a.u.)^3 using (LSDA), while it has been varied from 122 (a.u.)^3 to 161 (a.u.)^3 using (GGA) method, as shown in Figures 3.14-(a, b), with optimized number of k-points ($K_{\text{ired.}} = 55$) and $R_{\text{MT}} \cdot K_{\text{max}}$ cutoff of 9

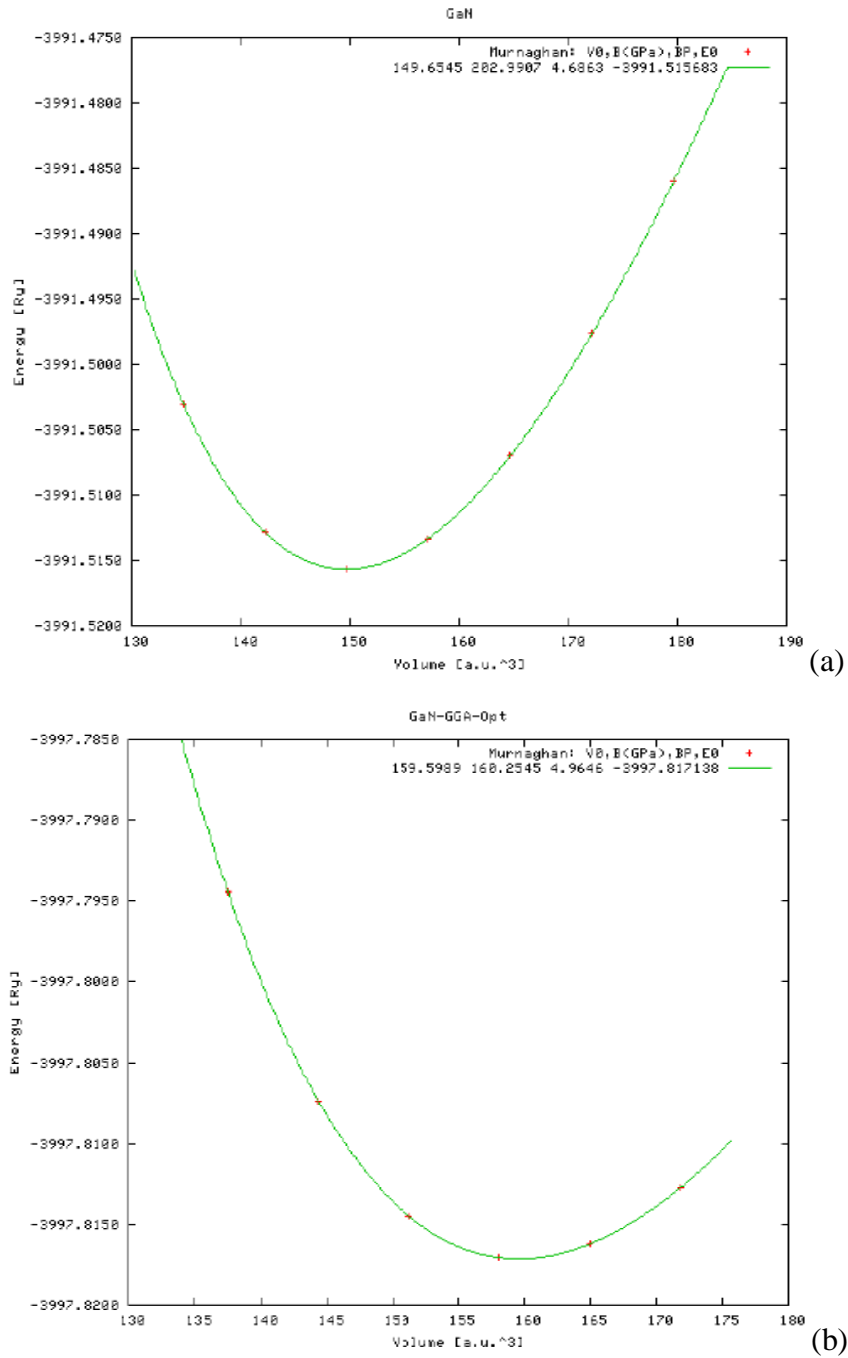


Figure 3.13: Optimization procedure for GaN using: a) LSDA and b) GGA methods.

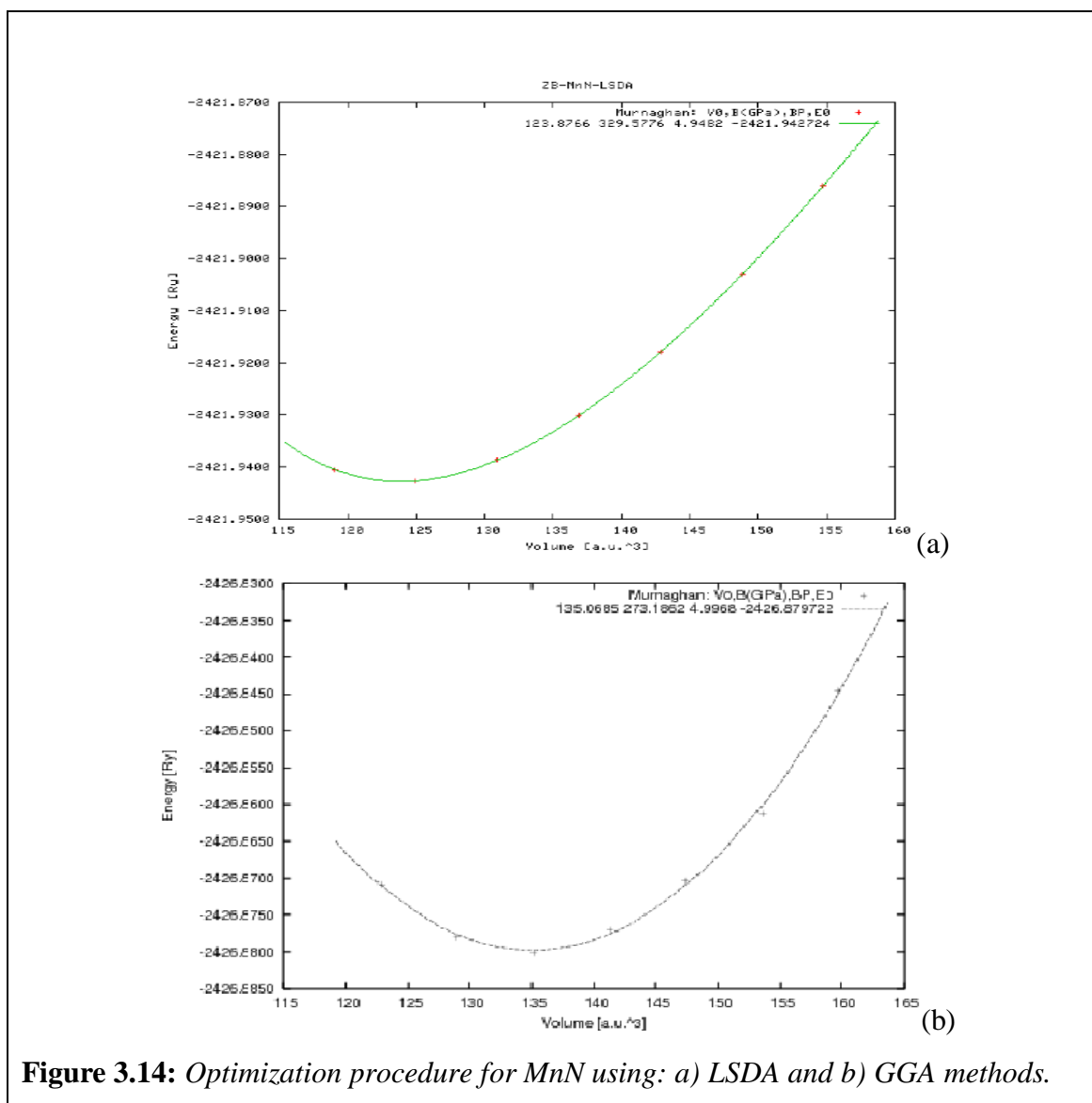
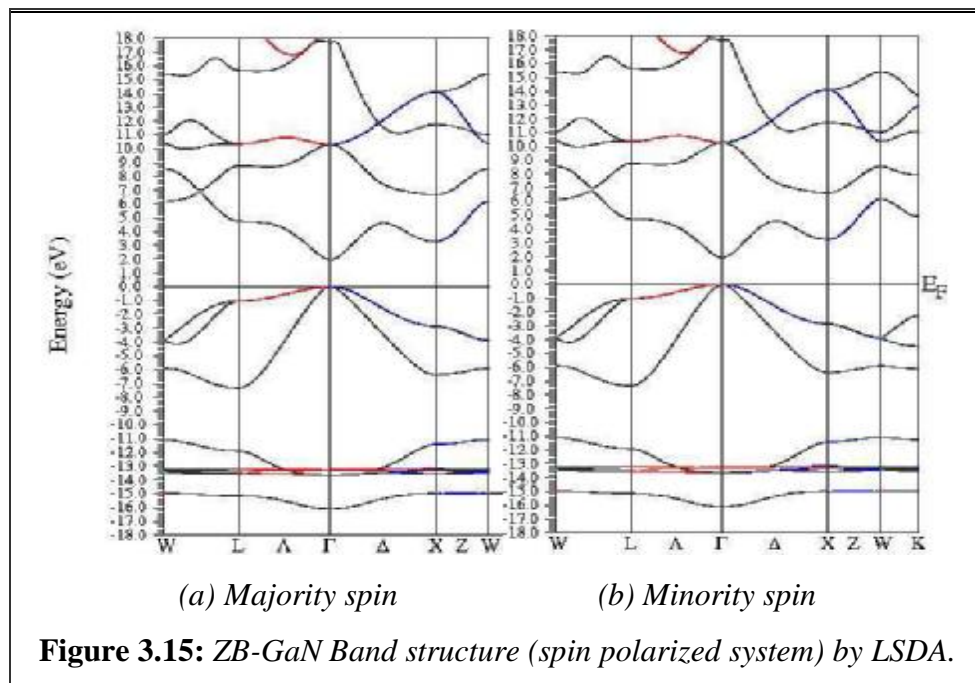


Figure 3.14: Optimization procedure for MnN using: a) LSDA and b) GGA methods.

3.2.2 GaN and MnN Electronic Properties

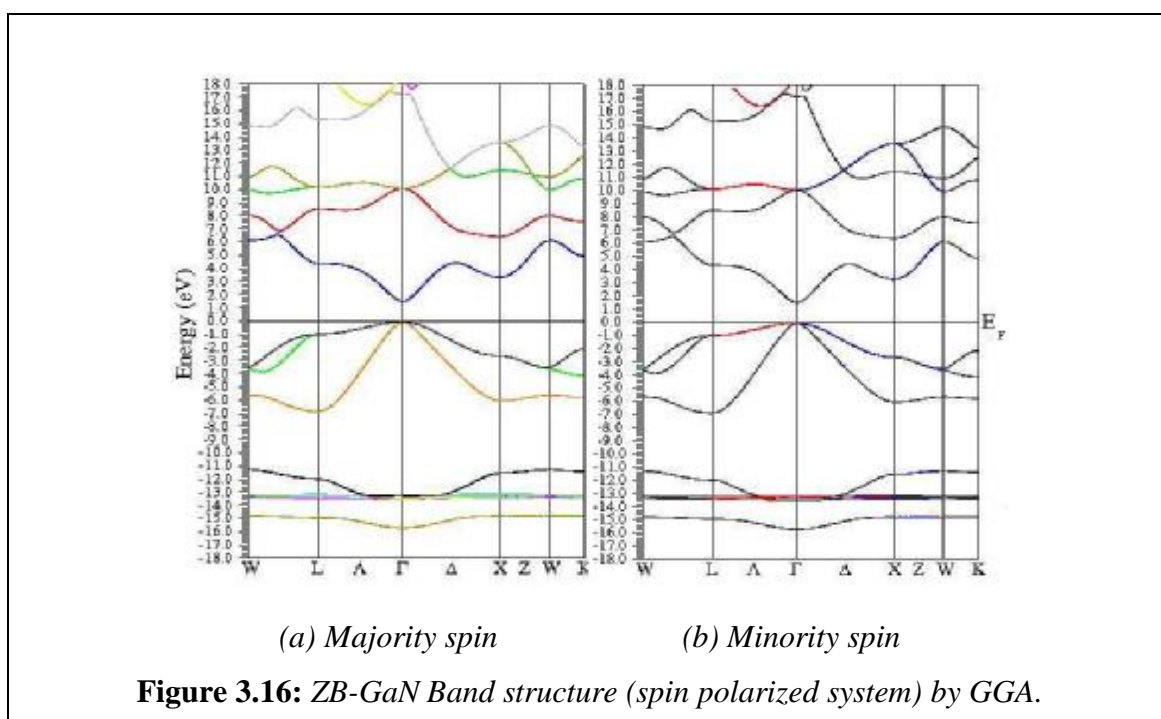
In crystalline solids, atoms interact with their neighbors, and the energy levels of the electrons in isolated atoms turn into bands. Whether a material conducts or not, it is determined by its band structure and the occupancy of these bands as determined by the Fermi level. Electrons, being fermions, follow the Pauli exclusion principle, meaning that two electrons in the same interacting system cannot occupy the same state, which further means

that their four quantum numbers have to be different. Thus electrons in a solid fill up the energy bands up to a certain level, called the Fermi energy. Bands which are completely full of electrons cannot conduct electricity, because there is no state of nearby energy to which the electrons can jump. Therefore materials in which all bands are full (i.e. the Fermi energy is between two bands) are insulators. In some cases, however, the band theory breaks down and materials that are predicted to be conductors by band theory turn out to be insulators. Mott insulators and charge transfer insulators are two such classes of insulators are a class of materials that are expected to conduct electricity under conventional band theories, but which in fact turn out to be insulators when measured. This effect is due to electron-electron interactions which are not considered in the formulation of conventional band theory.



The self-consistent band structures of GaN and MnN are calculated in fcc phase (ZB-structure) at equilibrium volume within the LSDA and GGA

Scheme (Figures 3.15-3.17). For GaN taking into account vectors directions (spin direction) up and down respectively.



GaN in the ZB phase has a direct band gap 1.938 eV, 1.551 eV within the LSDA and GGA, respectively. GGA calculations have no new feature on the band structure of LSDA, unless that the energy gap is smaller than that previously calculated of LDA with semiempirical pseudopotential calculations [80]. This is an accepted result that it has a good agreement with the experiments in what concerns the shape of the bands and the energy levels. It can be shown that fcc-GaN phase is a semiconductor. The profile of this band is in agreement with the earlier work by other methods.

The calculated energy band gaps of GaN are listed in Table 3.13 for LSDA and GGA as well as other calculations and experimental results.

For ZB-MnN, the calculated energy gap -0.00326 eV within LSDA method and -0.00158 eV within GGA method is listed in Table 3.13 for both LSDA and GGA approximations. It is shown in Figure 3.17 the hybridization of the N-p orbitals with the Mn-3d orbitals which reduces the gap to be minus. Movement of the valence band maximum upwards caused by the interaction between p and d states.

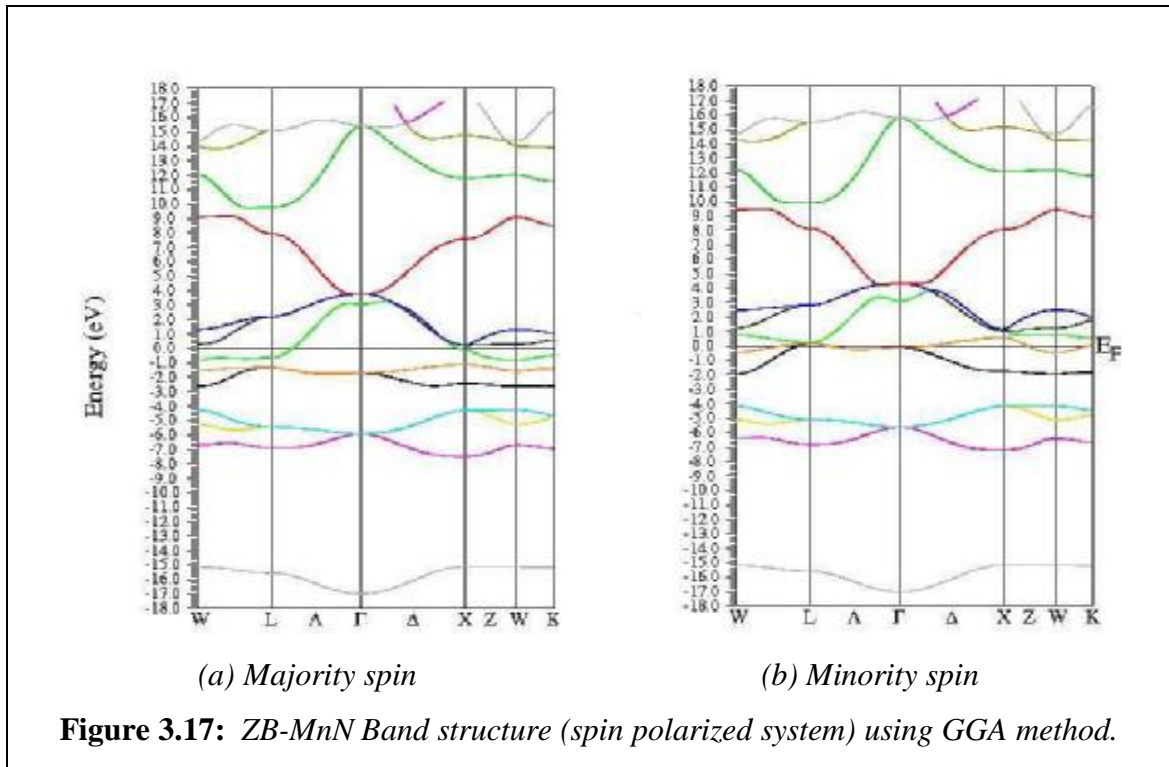
Table 3.13: *Calculated and experimental energy band gap (E_g) of GaN and MnN in ZB-structure (in eV).*

Approach	$E_g^{\Gamma-x}$	$E_g^{\Gamma-L}$	$E_g^{\Gamma-\Gamma}$
GaN			
LSDA	3.153	4.814	1.938
GGA	2.994	4.342	1.551
Other Calculations	3.2 ^{a,c}	(5.0) ^c	2.1 ^c , 1.93 ^d , 1.9 ^{a,b}
Experiment			(3.29 – 3.35) ^e
MnN			
LSDA	-0.00835	-0.00326	-0.01942
GGA	-0.00812	-0.00158	-0.01926

a : Ref.[79], b : Ref.[80], c : Ref.[81], d : Ref.[82], e : Ref.[83, 84]

This p-d coupling reduces the band gaps as known for nitride compounds [86]. From the Figure 3.17, it can be seen the overlap between p-d orbitals, this overlap came from the p-d coupling, which increases with small p-d energy differences. The overall band profile exhibits characteristic features

similar to other pd-compounds as Fe and Cr. Metallization is due to the indirect band gap closing at Γ and L-points.



3.3 Ga_{1-x}Mn_xN Ternary Alloys

Most of the $Ga_{1-x}Mn_xN$ experimental work to date has been carried out on wurtzite structures [87]; only a few studies are dedicated to the ZB structure [88, 12], which may present very different physical and electronic properties. $Ga_{1-x}Mn_xN$ in the wurtzite structure has been grown in several microcrystalline ($x = 0.005$), bulk ($x = 0.03$) [89], epitaxial ($x = 0.14$) and Mn-doped ($x = 0.03-0.05$) forms [91]. However, the experimental results

show significant discrepancies ferromagnetic half-metallic state. We identify and analyze the individual atomic contributions to the magnetic moment of the unit cell of $Ga_{1-x}Mn_xN$ systems as diluted ($x = 0.125, 0.25$) and much more ($x = 0.5, 0.75$). To our best knowledge, this is the first time such concentrations have been analyzed of these systems, in the ZB phase, is accomplished.

3.3.1 Optimization procedure of the lattice constants for $Ga_{1-x}Mn_xN$ Ternary Alloys

The unit cells of the ternary alloys are defined by Vegards law (L. Vegards 1921) as follows:

$$a(Ga_{1-x}Mn_xN) = x \cdot a(MnN) + (1 - x) \cdot a(GaN) \quad (3.3.1)$$

In the ZB case, the volume is directly related to the lattice constant a , the volume of the cell is varied in a specific ranges to calculate the total energy as a function of the volume for each of the ordered alloys. In order to obtain the best results, it is very necessary to make the tests for the K-points and $R_{MT} \cdot K_{max}$, that summarized in Table 3.3 and Table 3.4 for K-points, and Tables 3.8, 3.9 for the $R_{MT} \cdot K_{max}$. The cut off energies have been taken carefully for every system to be $13.5 \text{ Ry} = 183.735 \text{ eV}$. The evaluated values for the initial lattice constants and the optimized values at equilibrium are summarized in Table 3.14. Comparing with those previous other calculated methods [93, 94] they have found the following optimized values of lattice constants 4.48 \AA and 4.45 \AA for $x = 0.125$ and $x = 0.25$ respectively. Kanoun found that it is 4.461 \AA for $x = 0.25$ concentration

using LDA [12]. Our results for diluted $Ga_{1-x}Mn_xN$ are in agreement with the previous results, while for higher concentrations up to our best knowledge there are no studies for $Ga_{1-x}Mn_xN$.

Table 3.14: Evaluated and optimized lattice constants for $Ga_{1-x}Mn_xN$ in the ZB-structure.

Concentration	0.125	0.25	0.50	0.75
LSDA[$Ga_{1-x}Mn_xN$]				
$a_{eval.} (A^0)$	4.430	4.390	4.320	4.260
$a_{opt.} (A^0)$	4.450	4.446	4.400	4.270
B(GPa)	135	195	166	294
B'	3.86	4.25	4.97	3.60
GGA[$Ga_{1-x}Mn_xN$]				
$a_{eval.} (A^0)$	4.53	4.50	4.43	4.37
$a_{opt.} (A^0)$	4.54	4.52	4.47	4.38
B(GPa)	114	165	148	234
B'	3.18	5.42	1.37	3.75

3.3.2 Computational Details

All calculations are performed using the self-consistent full-potential linearized augmented plane-wave (FP-LAPW) method within the density functional theory, as implemented in the WIEN2K code. The local spin density approximations (LSDA) as well as the generalized gradient approximations (GGA) are used to treat the exchange correlation potential. The muffin-tin radii (R_{MT}) used are 1.78 a.u, 1.78 a.u, and 1.6 a.u for Ga, Mn and N, respectively. The cutoff parameters are presented from tables of the tests and the figures followed that have been discussed before. The best $R_{MT} \cdot K_{max}$ values (for the plane wave) using LSDA- $Ga_{1-x}Mn_xN$ are 8.5, 8.5, 8, and 8.5 for $x = 0.125, 0.25, 0.50,$ and 0.75 respectively, and with GGA have been found to be 9, 9, 8.5, and 8.5 for $x = 0.125, 0.25, 0.50,$ and 0.75 respectively as summarized in the tables and the figures followed that have been mentioned in the section of the tests, and $G_{max} = 14$ for the charge density, where R_{MT} is the smallest atomic sphere radius, K_{max} represents the maximum number of plane waves, G_{max} is the largest reciprocal lattice vector. An improved tetrahedron method is used for the Brillouin-zone (BZ) integration.

We achieved convergence in the energy to within less than $1.361 \cdot 10^{-5}$ eV. The irreduced K-points that have been taken for the LSDA- $Ga_{1-x}Mn_xN$ alloys calculations were 20 for $x = 0.125$ and $x = 0.75$, while for $x = 0.25$ and 0.50 they were 30 irreduced K-points. For GGA- $Ga_{1-x}Mn_xN$, the irreduced K-points were found to be used in the following values: 30, 40, 14, and 40 for $x = 0.125, 0.25, 0.50,$ and 0.75 , respectively. Inside the

muffin-tin spheres, the angular momentum expansion is truncated at $l_{\max} = 10$ for the wave functions.

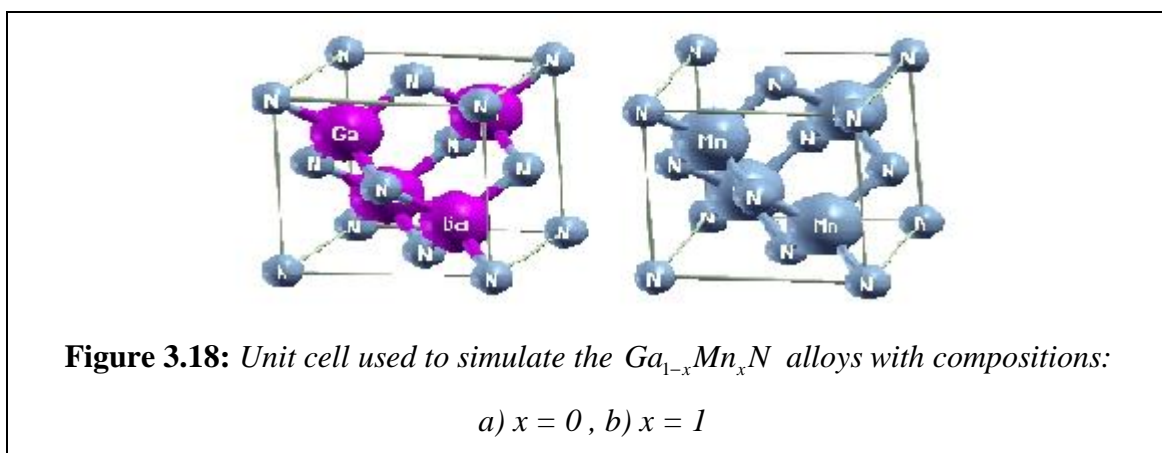
3.3.3 $\text{Ga}_{1-x}\text{Mn}_x\text{N}$ Alloys Geometry

In order to simulate the ordered alloys with ZB structure and compositions $x = 0.125, 0.25, 0.50$ and 0.75 , we adopt supercells containing 32 atoms for $x = 0.125$ and 8 atoms for the other concentrations of Mn atoms with cubic symmetry. The alloy consists of a cation sublattice where the metals are interchanged (Ga and Mn) and an anion sublattice (N), both originated from the Zinc-blende structure as shown in the Figures (3.18-3.20). To optimize the structure, we take the steps of our procedure and simulate relaxing the supercell as follows:

- Starting with GaN cubic cell; $a = b = c$, with the suitable R_{MT} for the atoms.
- Inserting Mn atoms (doping) with certain numbers as shown in (Figures 3.18 - 3.20) for $\text{Ga}_{1-x}\text{Mn}_x\text{N}$.
- Making the k -Points and $R_{MT} \cdot K_{\max}$ tests. Cut off energy have been taken carefully to be 13.5 Ry (taking into account the overlapping of the spheres and the leakage of the electrons).
- Testing the convergence (we achieved convergence in the energy to within less than 10^{-6} Ry = $1.361 \cdot 10^{-5}$ eV).
- Check the force and the magnetic moments for the system.
- The system is optimized, changing the volume of the cell. The fermi energy, the forces and the energy dependence on the volume were tested.

- The system is relaxed a gain changing the volume of the cell. The magnetic moments, fermi energies, the forces, and the energy dependence on the volume were tested as shown in Figures (3.21-3.24).

The results were fitted to the Murnaghan equation of state in order to obtain the equilibrium lattice constant, bulk modulus B , and the first derivative of the bulk. For $\text{Ga}_{0.875}\text{Mn}_{0.125}\text{N}$, the volume is varied from 4020 (a.u.)^3 to 4630 (a.u.)^3 for LSDA calculations as shown in Figure 3.21-a, while Figure 3.21-b shows that the variation begins at 3850 (a.u.)^3 and ends at 4450 (a.u.)^3 for the GGA calculations. For $\text{Ga}_{0.75}\text{Mn}_{0.25}\text{N}$, the volume is varied from 470 (a.u.)^3 to 670 (a.u.)^3 for LSDA calculations, and it is varied from 470 (a.u.)^3 to 730 (a.u.)^3 for the GGA as shown in Figures 3.22-a, b respectively. The equilibrium values are obtained using Murnaghan equation of state fit. It is found that the minimum energies occurs at the lattice constants $a_o^{LSDA} = 4.450, 4.446, 4.401, 4.270 \text{ \AA}$ for $x = 0.125, 0.25, 0.50, 0.75$, while for the GGA calculations, it is found to be $4.54, 4.52, 4.47, 4.38 \text{ \AA}$ for $x = 0.125, 0.25, 0.50, 0.75$ respectively as summarized in Table 3.14. Figures 3.23 and 3.24 show the variation of the energy dependence on the volume of the unit cell for the other systems of the doped Mn atoms.



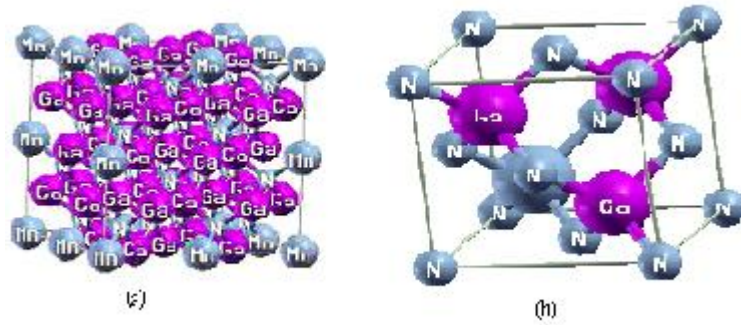


Figure 3.19: Unit cell used to simulate the $Ga_{1-x}Mn_xN$ alloys with compositions:

a) $x = 0.125$, b) $x = 0.25$

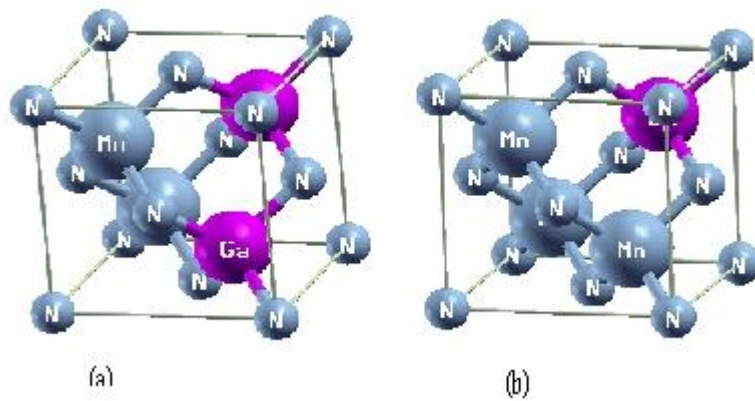


Figure 3.20: Unit cell used to simulate the $Ga_{1-x}Mn_xN$ alloys with compositions:

a) $x = 0.50$, b) $x = 0.75$

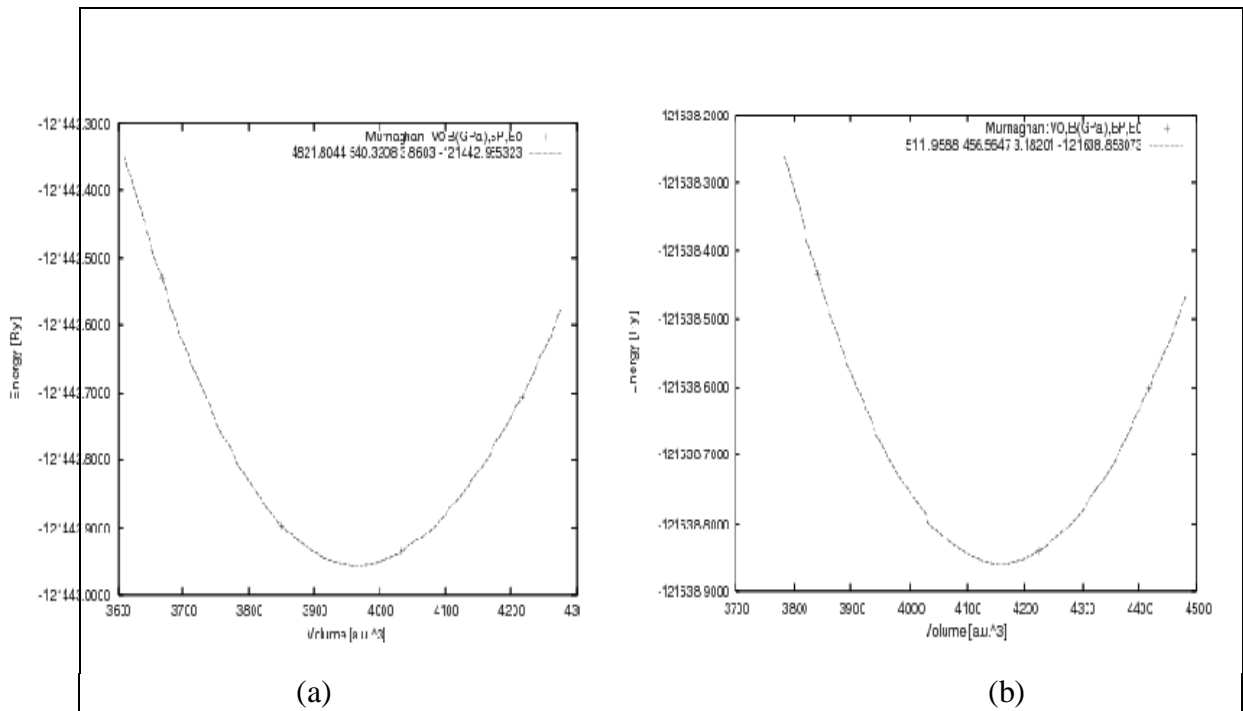


Figure 3.21: Total energy per atom as a function of volume for the alloys $Ga_{1-x}Mn_xN$ for $x = 0.125$ with approximations: a) LSDA, b) GGA.

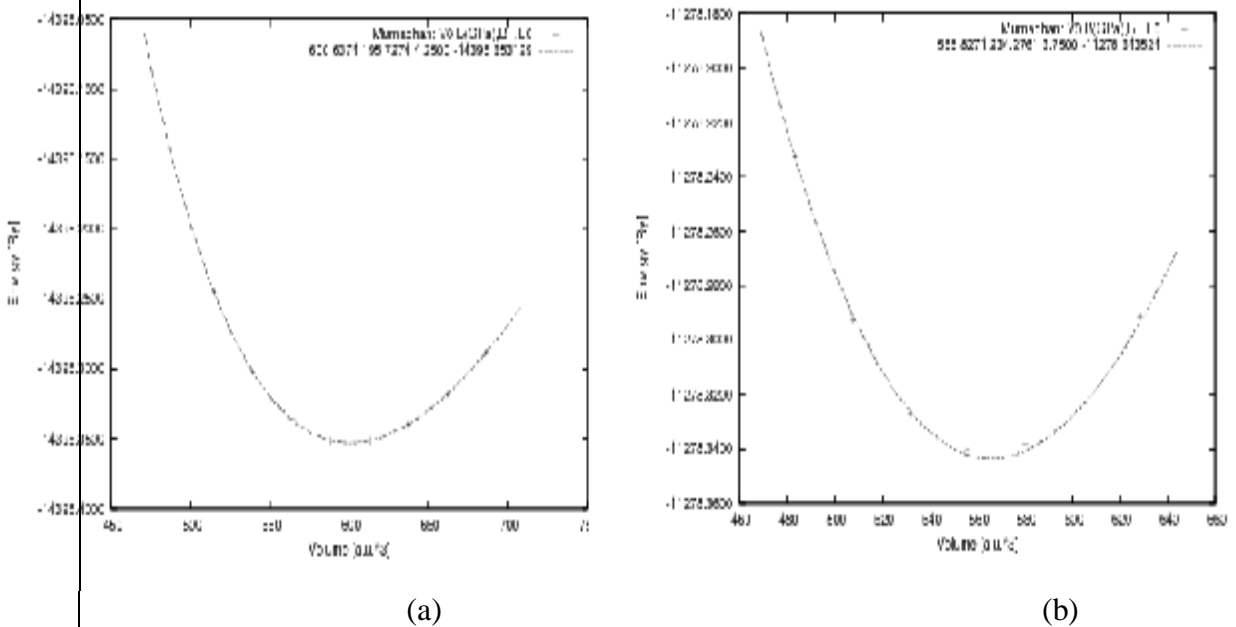


Figure 3.22: Total energy per atom as a function of volume for the alloys $Ga_{1-x}Mn_xN$ for $x = 0.25$ with approximations: a) LSDA, b) GGA.

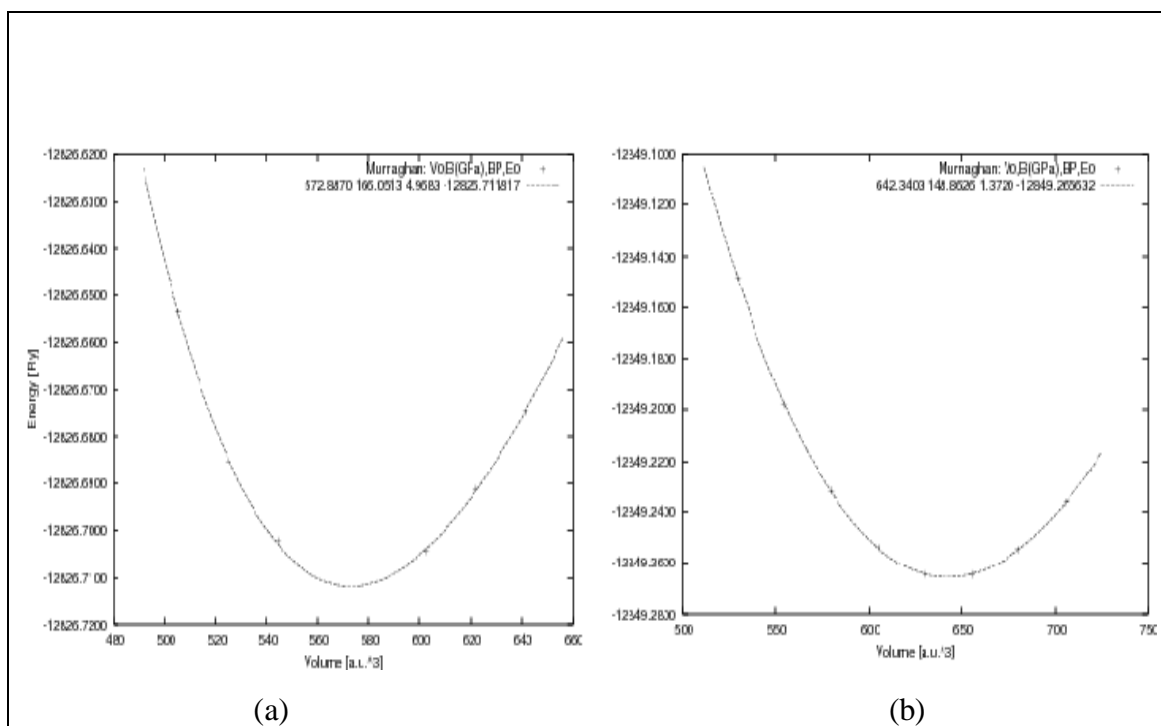


Figure 3.23: Total energy per atom as a function of volume for the alloys $Ga_{1-x}Mn_xN$ for $x = 0.5$ with approximations: a) LSDA, b) GGA.

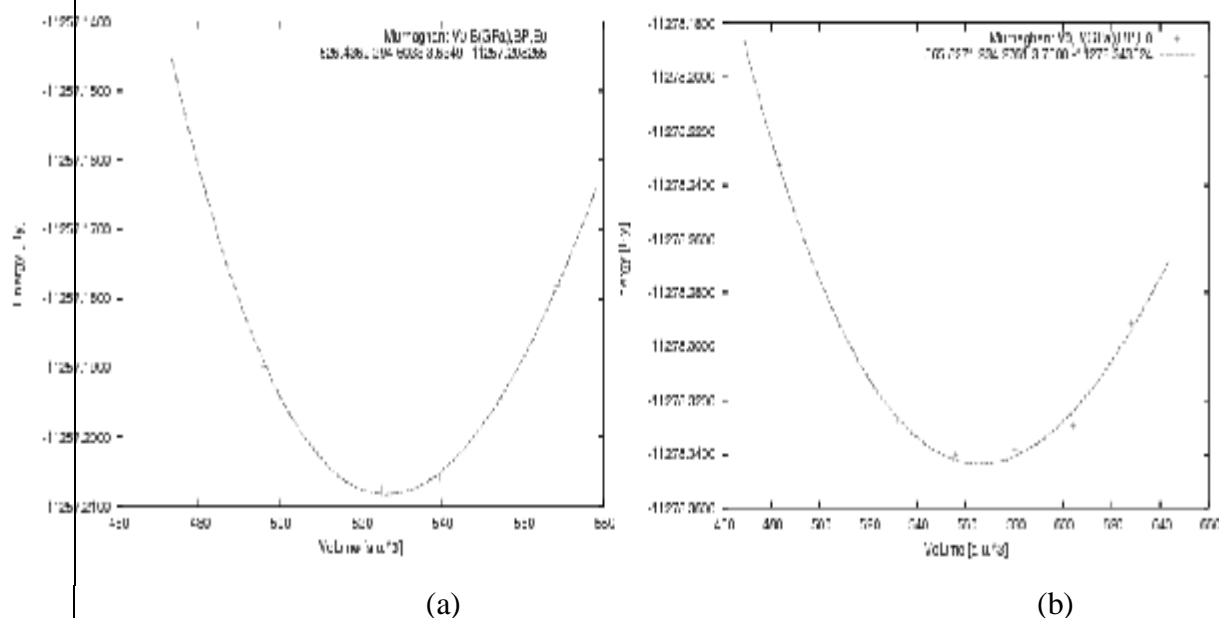


Figure 3.24: Total energy per atom as a function of volume for the alloys $Ga_{1-x}Mn_xN$ for $x = 0.75$ with approximations: a) LSDA, b) GGA.

3.3.4 $Ga_{1-x}Mn_xN$ Electronic Properties

In present section the electronic structures and changes of the energy band gaps also have been analyzed for $Ga_{1-x}Mn_xN$ ternary alloys. The spin-polarized band structures of the compositions of Mn atoms ($x = 0.25, 0.75$ as samples for comparison) for LSDA and GGA methods are shown in the Figures (3.25 - 3.26).

As expected, one can see that the Mn-3d bands get thinner when the concentration x is decreased, or in other words we can say that increasing the Mn mole fraction (concentration), affecting on the band gap of the $Ga_{1-x}Mn_xN$ alloys to be decreased. This band has some dispersion along some directions of the Brillouin zone and this is an important detail for the alloys to behave properly as half-metallic, as the Fermi level runs across the band.

The spin-polarized band structures for the $Ga_{0.75}Mn_{0.25}N$ alloy at the lattice constants $a_o = 4.446 \text{ \AA}$ with LSDA and $a_o = 4.52 \text{ \AA}$ with GGA are depicted in Figures 3.25-(a, b), and for the $Ga_{0.25}Mn_{0.75}N$ alloy at the lattice constants $a_o = 4.27 \text{ \AA}$ with LSDA and $a_o = 4.38 \text{ \AA}$ with GGA are depicted in Figures 3.26-(a , b).

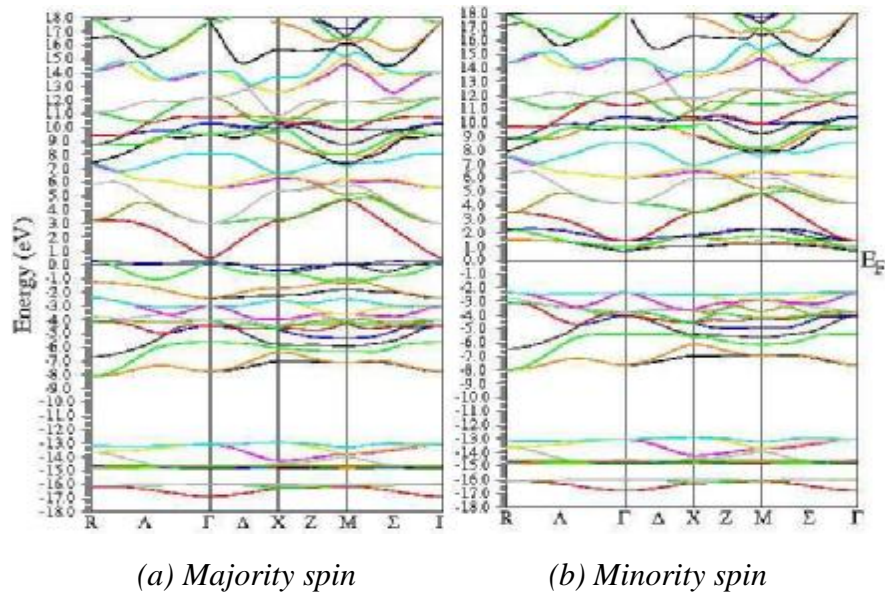


Figure 3.25: The spin polarized band structure for $Ga_{0.75}Mn_{0.25}N$ in the ZB- structure:
a) Majority spin, b) Minority spin.

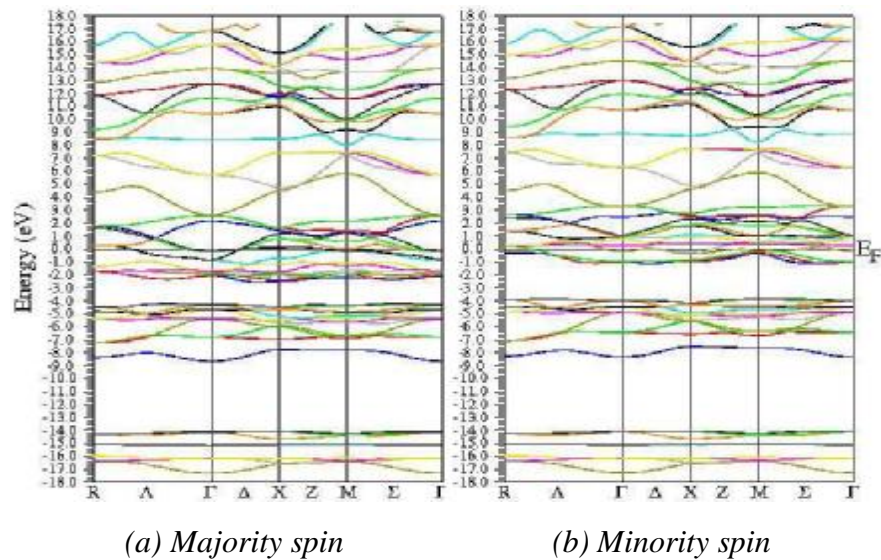


Figure 3.26: The spin polarized band structure for $Ga_{0.25}Mn_{0.75}N$ in the ZB- structure:
a) Majority spin, b) Minority spin.

We define the majority-spin component to be the one that contains the largest number of electrons. Taking the first case (0.25Mn), the N-s states are low-lying around -15 eV, below the top of the valence band. The states in the energy range from -13.0 eV to -15 eV are contributed primarily from Ga-3d states. The states in the energy range from -8.1 eV to -2.3 eV come mainly from N-2p states and are mixed with a minor amount of Mn- 3d and Ga-4s, 4p states. The Mn-3d band contribution for the majority-spin system can be divided into two parts: first, the Mn-3d-e (doubly degenerated) band. Second, the Mn-3d-t₂ (triply degenerated) band, which is centered at -0.036 eV. As one can see, the majority-spin band structure shown in Figure 3.27 has the same overall structure as the minority-spin, except for the region between -2.4 eV and 2.4 eV. So it is found that this system has a narrow gap around (1.34 eV), while for the other cases it depends on the concentration of Mn. The energy band gaps of the system of interest have been summarized in Table 3.15.

Table 3.15: A summary of the energy band gaps (eV) for $Ga_{1-x}Mn_xN$.

Concentration	0.125	0.25	0.50	0.75
$[Ga_{1-x}Mn_xN]$				
E_g^{LSDA} (eV)	2.09	1.34	0.92	0.41
E_g^{GGA} (eV)	2.16	1.33	0.85	0.38
Other results	2.2 a	1.334 b	-	-

a : Ref [95], b : Ref [12]

The calculated band structures for $Ga_{0.875}Mn_{0.125}N$ are in agreement with those already calculated theoretically using the (FP-LMTO) method [95].

From these comparisons, we believe that our results for the $\text{Ga}_{0.75}\text{Mn}_{0.25}\text{N}$ and $\text{Ga}_{0.875}\text{Mn}_{0.125}\text{N}$ alloys with the cubic structure results for M. Kanoun and B.S. Kang *et al* [12] may provide a good approximation to the average values of the other systems.

3.4 $\text{Ga}_{1-x}\text{Mn}_x\text{N}$ Magnetic Properties

Mn-doped GaN, $\text{Ga}_{1-x}\text{Mn}_x\text{N}$ was predicted by Dietl *et al.* [89] to be ferromagnetic with a high Curie temperature, with possible use in spintronics. Several workers have since investigated $\text{Ga}_{1-x}\text{Mn}_x\text{N}$ because of its potential applications [90]. Thus, magnetic, optical, and electronic properties of $\text{Ga}_{1-x}\text{Mn}_x\text{N}$, especially in the form of thin films, have been reported widely. Thus, Overberg *et al.* [87] found room temperature ferromagnetism in $\text{Ga}_{1-x}\text{Mn}_x\text{N}$ films for Mn levels below 0.07, while Zajak *et al.* [91] reported that Mn-doped GaN to be paramagnetic. The highest T_c reported so far in $\text{Ga}_{1-x}\text{Mn}_x\text{N}$ films is by Sasaki *et al.* [92] who prepared the films by reactive molecular beam epitaxy using ammonia as the nitrogen source. Some of the studies have suggested the possible presence of second phases such as Ga-Mn or Mn-N alloys as being responsible for the observation of ferromagnetism. One of the limitations in most of the studies of thin films is that they are generally prepared at temperatures in the range of $750\text{-}1250\text{C}^\circ$. Such temperatures can give rise to Ga-Mn alloy impurities with high ferromagnetic T_c s.

By the way we made the calculations, having only one Mn atom per unit cell, the calculated phase is ferromagnetic. The calculated magnetic

moment was found to be about $4.00 \mu B$ for both $x = 0.125$ and $x = 0.25$, showing that the magnetization of the cell does not change with the Mn concentration in the dilution case. On the other hand we have found the local magnetic moments to be $3.15, 3.04 \mu B$ (Mn), $0.0174, 0.0352 \mu B$ (Ga) and $-0.028, 0.0277 \mu B$ (N) for $x = 0.125$ and $x = 0.25$ respectively. For the cases (0.75, 0.50, 0.25, 0.125) Mn, the spin magnetic moments of these four alloys are given in Table 3.16.

Table 3.16: Magnetic moments in $Ga_{1-x}Mn_xN$ systems in the ZB-structure.

Concentration	0.00	0.125	0.25	0.50	0.75	1.00
<i>Total magnetic moments in $Ga_{1-x}Mn_xN$</i>						
<i>LSDA – $MM^{tot.} (\frac{mB}{Mn})$</i>	0.0002	4.01	3.93	4.70	3.54	0.00
<i>GGA – $MM^{tot.} (\frac{mB}{Mn})$</i>	0.00	4.0	4.02	4.14	3.46	0.00
<i>Local magnetic moments in $Ga_{1-x}Mn_xN$</i>						
Mn (μB)	-	3.150	3.042	3.226	3.184	0.00045
Ga (μB)	0.0065	0.0174	0.035	0.055	0.0417	-
N (μB)	-0.0005	-0.028	0.028	0.010	0.0295	-0.00049

From Table 3.16 we can also find that the magnetic moment of about $4.0 \mu B$ per the Mn is in agreement with the other theoretical calculations [96,91,12], and the total spin magnetic moment of $Ga_{1-x}Mn_xN$ is about 4.0

μ_B per molecule [95]. Wei *et al* studied Ga_3MnN_4 and $Ga_{15}MnN_{16}$, these results show that the interaction of the Mn atoms with the valence band is ferromagnetic (FM). Table 3.16 shows that the total magnetic moment for the system of interest is going about $4m_B$. We can note that the most important role in this system is due to the contribution of the Mn atoms, also there is a little contribution by Ga and N atoms in some cases, but there is a decrease or loss of some of the total magnetic moment, this can be found in the interstitial region (*I*).

Chapter Four

Summary and Conclusion

The $Ga_{1-x}Mn_xN$ properties are calculated using the self-consistent FP-LAPW method with the LSDA and GGA exchange correlation potentials. We have investigated the equilibrium lattice parameters for different values of Mn concentrations ($x = 0.00, 0.125, 0.25, 0.50, 0.75, 1.00$), this can be shown in the first part of our results (bulk parameters). Our results are in good agreement with the others [75, 93]. The lattice parameters of $Ga_{1-x}Mn_xN$ alloys depend strongly on the concentration of the Mn-doped atoms.

Table 3.14 shows that the equilibrium values of the lattice constants depend on the concentration of the doped Mn atoms; this can be shown in the Figure (4.1). Our results give us a good agreement with other theoretical results [12].

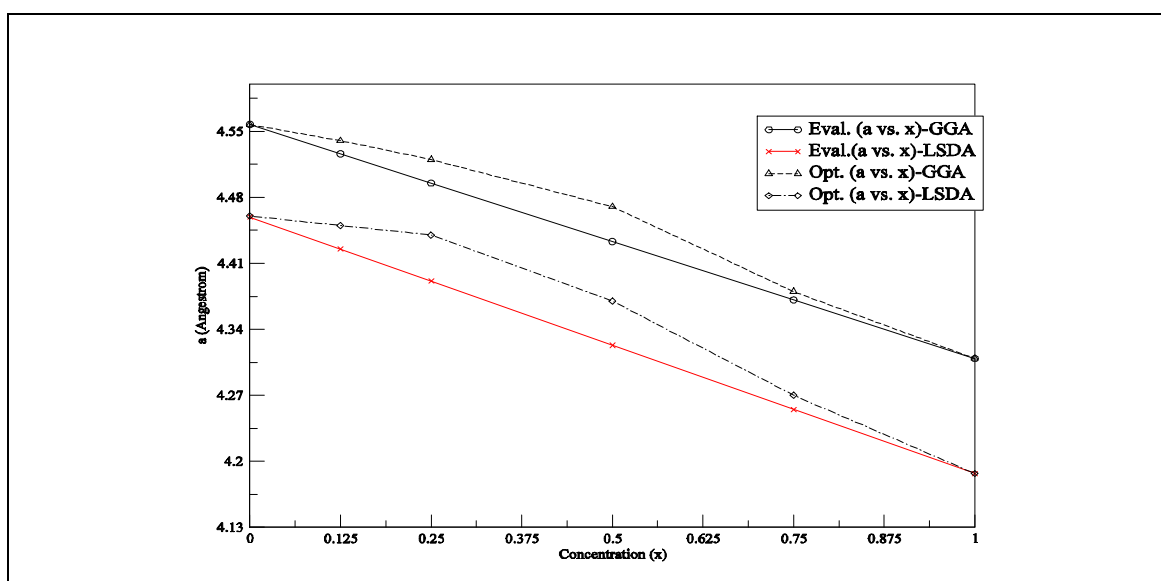


Figure 4.1: Evaluated and optimized lattice constants vs. the Mn concentration for the $Ga_{1-x}Mn_xN$ systems.

The band structure calculations for Mn-doped zinc-blende GaN using the FP-LAPW method are carried out. Upon Mn doping into GaN, new states were found to form within the band gap of GaN, and the Fermi level was shifted downward. An increase of Mn concentration broadens the impurity bands in DMSs, but does not change their energies. The majority-spin band Mn-3- d-e (doubly degenerated) is fully occupied and the band Mn- 3d-t2 (triply degenerated) is partially filled or almost half filled, whereas the minority-spin Mn-3d gap bands are empty.

For $Ga_{1-x}Mn_xN$ ($x=0.125, 0.25, 0.50, 0.75$) the FM state is more energetically stable than the anti-ferromagnetic state (AFM). It is possible that Mn-N or Ga-Mn compounds are formed in the crystal and contribute to the ferromagnetic properties [97, 98, 99, 100]. Therefore in this range of lattice parameters ($4.19 \text{ \AA} - 4.56 \text{ \AA}$), the MnN material changes from a non-magnetic metallic phase to a ferromagnetic phase in which the majority-spin system is metallic and the minority-spin is insulating. This phenomenon leads us to make a separate study for the volume expansion of the MnN cell, and show the behavior of the cell magnetic moment as a function of the lattice parameter. We can see that the total magnetic moments for MnN are zero at the equilibrium lattice parameters ($a_o^{LSDA} = 4.187 \text{ \AA}$, and $a_o^{GGA} = 4.31 \text{ \AA}$). In both approaches it is predicted that expansion tends to turn the material more ferromagnetic.

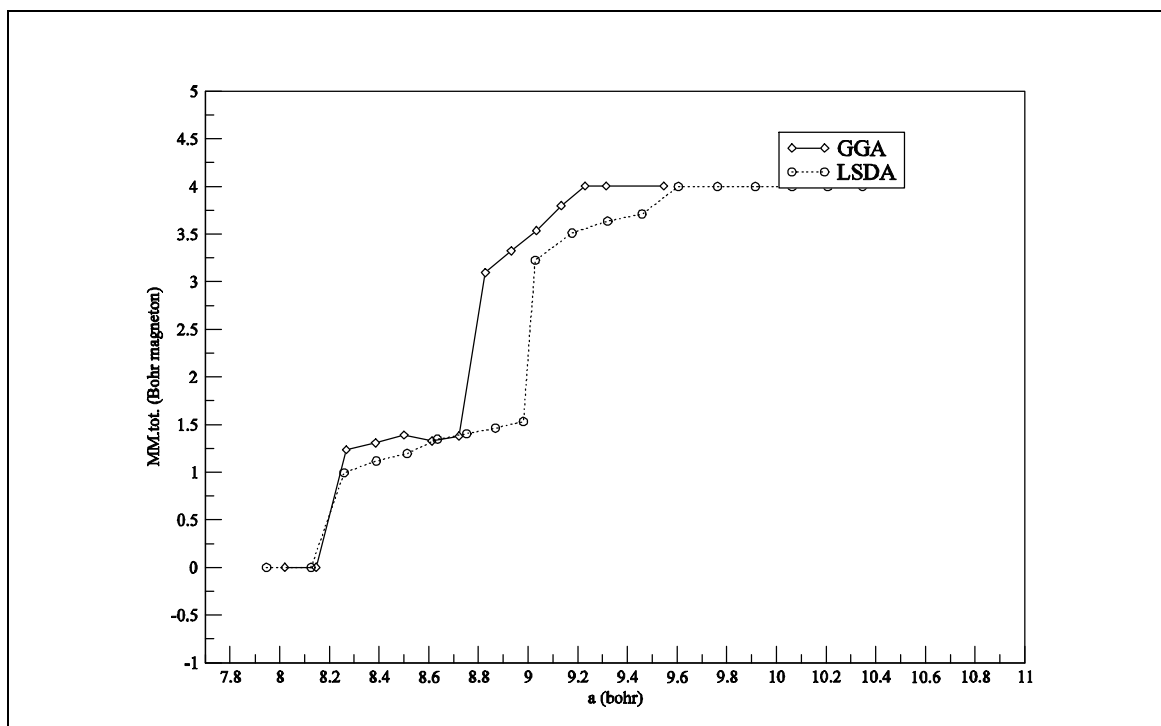


Figure 4.2: Magnetization for the MnN compound as a function of the lattice parameter in both approaches LSDA and GGA.

It can be seen in figure 4.2 that the magnetic moments increase as a function of the lattice parameters, and there is saturation at the value around $4 m_B$ in both cases. These results have a good agreement with R. de Paiva *et al.* [78]. Kang *et al* [101] studied $Ga_{1-x}Mn_xN$ for Mn concentrations of about 0.06; they found that the ferromagnetic solution is more stable than the anti-ferromagnetic state.

The magnetic properties of alloys depend strongly on both the conduction electron concentration and chemical order. For spintronics applications, minimizing interfacial reactions and controlling the growth of Heusler alloys thin films are very important task.

In all of $Ga_{1-x}Mn_xN$ systems, we calculate a total magnetic moment around $4 m_B$, strongly localized on the Mn site. However the orientation of spins around the impurity is different. In some cases, all magnetic moments are parallel to the Mn moment, while in the others the moments of the nearest N atoms are antiparallel, which agrees with experiment. The first behavior may be interpreted as a tunneling of spin-up impurity states to neighboring atoms, while the second one is in accordance with Ruderman-Kittel-Kasuya-Yoshida (RKKY) model [102, 103], which describes the magnetic moment embedded in a uniform electron gas.

The electrical transport properties of $Ga_{1-x}Mn_xN$ are not simply related to its magnetic characteristics. Further investigations must be performed to explain the physical mechanisms.

In a word, now we have a more complete picture of the structure and magnetic properties of $Ga_{1-x}Mn_xN$ systems. And by investigating a class of $Ga_{1-x}Mn_xN$ and other related magnetic and non-magnetic materials, we study the foundations of physics, and also explore new possible device structures which appear to be good candidates for spintronics applications.

References

- [1] S. Nakamura, T. Mukai M. Senoh. **Applied Physics Letter. 64, 1687** (1994).
- [2] S. D. Smith, *Optoelectronic Devices*, London: **Prentice –Hall, p92** (1995).
- [3] I. Moreno. ”*LED Intensity Distribution*”. **International Optical Design, Technical Digest.** (2007).
- [4] S Nakamura, M. Senoh, S. Nagahama, N. Iwasa, T Yamada, T Matsushita, H. Kiyoku, Y. Sugimoto, Jpn. **Journal of Applied Physics. 35, L74-L76** (1996).
- [5] R.Gunshore, A. Nurmikko and M. Kobayashi, **Physics World March47** (1992).
- [6] O. Madelung, *Physics of III-V Compounds* (New York: Wiley) p **18** (1964).
- [7] W.A. Harrison, *Electronic Structure and the Properties of Solids*, **Dover, New York**, (1989).
- [8] A. Garcia and M. L. Cohen, **Physical Review B 47, 4215** (1993).
- [9] S. Ruvimov, Z. Liliental-Weber, C. Dieker, J. Washburn, M. Koike, H. Amano, I. Akasaki in *Gallium Nitride and Related Materials II*, edited by C.R. Abernathy, H. Amano, J.C. Zolper, **Mater. Res. Soc. Symp. Proc. 468, Pittsburgh, PA, pp. 287-293.** (1997).

- [10] N. W. Ashcroft, N.D. Mermin, Cornell University, *Solid state physics*, **Harcourt College Publishers**.
- [11] S. Saib, N. Bouarissa, **Physica B 387, 377-382** (2007).
- [12] M B Kanoun, S Goumri-Said, A. E. Merad and J. Cibert **Journal of Physics D: Applied Physics. 38 1853-1859** (2005).
- [13] Leeor Kronik, Manish Jain, and James R. Chelikowsky, **Physical Review B 66, 041203(R)** (2002).
- [14] C. Kittel *Introduction to solid state physics, a seventh edition*, Published by **John Wiley and sons**, Inc., New York, Chichester, Brisbane, Toronto, Singapore. "W.O.D"
- [15] M. Abu-Jafar, A. I. Al-Sharif, A. Qteish, **Solid State Communications, 116 389-393** (2000).
- [16] Ramirez-Flores G, Navarro-Contreras H, Lastras-Martinez A, Powell RC and Greene J E, **Physical Review B 50, 8433**, (1974).
- [17] Logothetidis S, Petals J, Cardona M and Moustakes TD, **Physical Review B 50, 18017** (1994).
- [18] Wladek, Walukiewicz, **Physica E, Volume 20, Issue 3-4, p. 300-307** (2004).
- [19] S. Gene, **Business Financial, Page F1, 1133 words**, (1964).
- [20] K. Tom, **IDG News Service** (2005).
- [21] D. E. Grider, N. X. Nguyen and C. Nguyen, **Solid-State**

Electronics, Volume 43, Issue 8, Pages 1473-1478 (1999)

[22] B. D. Cullity, *An Introduction To Magnetic Materials, Fifth Edition*, **Springer Publishers** (2003).

[23] Joonyeon Chang, Gyeungho Kim, Woo-Young Lee and Jae-Min Myoung, **Thin Solid Films, Volume 472, Issues 1-2, Pages 144-149**, (2005).

[24] M. Tanaka, Y. Higo: **Physical Review Letter. 87, 026602** (2001).

[25] J. Anthony, C. Bland, and E. B. Heinrich, *Ultra-thin Magnetic Structure*, **III Fundamentals of Nanomagnetism, Springer** (2005).

[26] M. Usuda, N. Hamada, **Physical Review B 66, 125101** (2002).

[27] P. LeClair, J.S. Moodera and H.J.M. Swagten, *Spin polarized electron tunneling, in Ultra-thin Magnetic Structures III: Fundamentals of Nanomagnetism*, **Eds. B. Heinrich and J.A.C. Bland, Springer, Berlin** (2005).

[28] H. Munekata, H. Ohno, S. von Molnar, Armin uller, L. L. Chang, and L. Esaki, *Diluted Magnetic III-V Semiconductors*, **Physical Review Letter. 63, 1849** (1989).

[29] H. Ohno, *Making Nonmagnetic Semiconductors Ferromagnetic*, **Science 281, 951** (1998).

[30] H. Akinaga and H. Ohno, *Semiconductor Spintronics*, **IEEE Transactions on Nanotechnology 1, 19** (2002).

[31] Venkatesan et al., **Physical Review Letter. 93, 177206** (2004).

- [32] Shan W, Walukiewicz W, Ager J W III, Haller, Geisz J F, Friedman D J, Olson J M, and Kurtz S R, **Physical Review Letter. 82 1221** (1999).
- [33] J. B. Ketterson and S. N. Song. **Superconductivity** (1999).
- [34] C. P. Gazzara, R. M. Middleton, R. J. Weiss, and E. O. Hall, **Acta Crystallography, 22, 859**, (1967) .
- [35] H. Hohenberg and W. Kohn, *Inhomogeneous Electron Gas*, **Physical Review. 136, B864** (1964).
- [36] M. Ernzerhof, J. P. Perdew, and K. Burke, *Density Functionals: Where do they come from, why do they work?, in Topics in Current Chemistry, Vol. 180, R.F. Nalewajski Ed. Springer, Berlin*, (1996).
- [37] C. Friedrich and A. Schindlmayr. John von Neumann Institute for Computing, Julich, **NIC Series, Vol. 31, ISBN 3-00-017350-1, pp. 335-355**, (2006).
- [38] M. Petersilka, U. J. Gossmann, and E. K. U. Gross, *Excitation Energies from Time- Dependent Density-Functional Theory*, **Physical Review Letter. 76, 1212** (1996).
- [39] J. D. Talman and W. F. Shadwick, *Optimized effective atomic central potential*, **Physical Review A 14, 36** (1976).
- [40] M. Weinert, E. Wimmer, and A. J. Freeman, *Total-energy all-electron density functional method for bulk solids and surfaces*, **Physical Review B 26, 4571** (1982).

- [41] D. Singh, *Planewaves, Pseudopotentials and the LAPW Method*, **Kluwer Academic Publishers, Boston/Dordrecht/London**, (1994).
- [42] J. C. Slater, *Energy band calculations by the augmented plane wave method*, **Advances in Quantum Chemistry** **1**, **35** (1964).
- [43] O. K. Andersen, *Linear methods in band theory*, **Physical Review B** **12**, **3060** (1975).
- [44] M. Weinert, *Solution of Poisson's equation: beyond Ewald-type methods*, **Journal of Math. And Physics**, **22**, **2433** (1981).
- [45] P. Blaha, K. Schwarz, P. Sorantin, and S.B. Trickey, *Full-potential, linearized augmented plane wave programs for crystalline systems*, **Comp. Physics Communications. Full-potential, linearized augmented plane wave programs for crystalline systems** **59**, **399** (1990).
- [46] D. D. Koelling and B. N. Harmon, *A technique for relativistic spin-polarized calculations*, **Journal of Physics C (Solid State Physics)** **10**, **3107** (1977).
- [47] J. M. Soler and A. R. Williams, *Augmented-plane-wave forces*, **Physical Review B** **42**, **9728** (1990).
- [48] S. Blugel, *First Principles Calculations of the Electronic Structures of magnetic Overlayers on Transition Metal Surfaces*, (**PhD thesis, RWTH Aachen**, (1988).
- [49] E. Sjöstedt, L. Nordström, and D. Singh, *An alternative way of linearizing the augmented plane-wave method*, **Solid State**

Communications. 114, 15 (2004).

[50] Ph. Kurz, F. Foorster, L. Nordstraom, G. Bihlmayer, and S. Blugel, *Ab initio treatment of noncollinear magnets with the full-potential linearized augmented plane wave method*, **Physical Review B** **69, 024415** (2004).

[51] Y. Mokrousov, G. Bihlmayer, and S. Blugel, *Full - potential linearized augmented plane-wave method for one-dimensional systems: Gold nanowire and iron monowires in a gold tube*, **Physical Review B** **72, 045402** (2005).

[52] E. E. Krasovskii, *Augmented-plane-wave approach to scattering of Bloch electrons by an interface*, **Physical Review B** **70, 245322** (2004).

[53] W. E. Pickett, *Pseudopotential methods in condensed matter applications*, **Comp. Physics. Rep.** **9, (1)15** (1989).

[54] H. Akai, M. Akai, S. Blugel, B. Drittler, H. Ebert, K. Terakura, R. Zeller, and P. H. Dederichs, *Theory of Hyperfine Interactions in Metals*, **Program of Theoretical Physics (Suppl)** **101, 11** (1990).

[55] W. Kohn and L. Sham. *Self-Consistent Equations Including Exchange and Correlation Effects*, **Physical Review**, **140:1133**, (1965).

[56] R. M. Dreizler and E. K. U. Gross, *Density Functional Theory*. **Springer Verlag, Berlin**, (1990).

- [57] J. P. Perdew, J. A. Chevary, S. H. Vosko, K. A. Jackson, M. R. Pederson, D. J. Singh, and C. Fiolhais, *Atoms, molecules, solids, and surfaces: Applications of the generalized gradient approximation for exchange and correlation*, **Physical Review B** **46**, **6671** (1992).
- [58] A. D. Becke, **Physical Review A** **38**, **3098** (1988).
- [59] R. O. Jones and O. Gunnarsson, *The density functional formalism, its applications and prospects*, **Review Model Physics**. **61**, **689** (1989).
- [60] L. Hedin and B. I. Lundqvist, *Explicit local exchange-correlation potentials*, **Journal of Physics. C (Solid State Physics)** **4**, **2064** (1971).
- [61] S. H. Vosko, L. Wilk, and N. Nusair, *Accurate spin-dependent electron liquid correlation energies for local spin density calculations: a critical analysis*, **Can. Journal of Physics**. **58**, **1200** (1980).
- [62] J. P. Perdew, K. Burke, and M. Ernzerhof, *Generalized Gradient Approximation Made Simple*, **Physical Review Letter**. **77**, **3865** (1996).
- [63] Josef Stoer, **Optimization Methods and Software, Volume 3, Issue 1 – 3** (1994).
- [64] D. D. Koelling and G. O. Arbman, *Use of energy derivative of the radial solution in an augmented plane wave method: application to copper*, **Journal of Physics. F (Metal Physics)** **5**, **2041** (1975).

- [65] V. L. Moruzzi, J. F. Janak, and A. R. Williams, *Calculated Electronic Properties of Metals*, **Pergamon, New York**, (1978).
- [66] Yoonsik Oh, E. Badraxe, P. Marksteiner, and A. J. Freeman, **Physical Review B** **46**, **4495 - 4501** (1992).
- [67] Ira B. Bernstein, John M. Greene, and Martin D. Kruskal, **Physical Review**. **108**, **546 - 550** (1957).
- [68] D. R. Chakraborty, and P. S. Salvekar, **Advances in Atmospheric Sciences. Volume 6, Number 4 / December**, (1989).
- [69] S. Porowski and I. Grzegory, **Group III Nitrides pp.71-88** (1994).
- [70] A. I. Lichtenstein and M. I. Katsnelson, *Ab initio calculations of quasiparticle band structure in correlated systems: LDA+U approach*, **Physical Review B** **57**, **6884** (1998).
- [71] C.H. Shang, J. Nowak, R. Jansen, J.S. Moodera: **Physical Review B** **58**, **R2917** (1998).
- [72] K. Suzuki, T. Kaneko, H. yoshida, Y. Obi, H. Fujimori and H. Morita, **Journal of Alloys and Compounds**. **306(1-2)**, **66** (2000).
- [73] F. Schippan, M. K^oastner, L. D^oaweritz and K. H. Ploog, **Applied Physics Letter**, **76**, **834** (2001).
- [74] R. de Paiva 2002, J.L.A. Alves, R.A. Nogueira, C. de Oliveira, H.W.L. Alves, L.M.R. Scolfaro and J.R. Leite, **Materials Science and Engineering B****93 2-5** (2002).

- [75] R. de Paiva et al., **Journal of Magnetism and Magnetic Materials** **288** 384-396 (2005).
- [76] Shi-Hao Wei, X. G. Gong, Gustavo M. Dalpian and Su-Huai Wei. **Physical Review B** **71**, 144409 (2005).
- [77] A. Janotti, Su-Huai Wei, and L. Bellaiche, **Applied Physics Letter**, Vol. **82**, No. **5**, (2003).
- [78] R. de Paiva et al., **Brazilian Journal of Physics** vol. **34** (2004).
- [79] B. Bouhafs, F. Litimein, Z. Dridi, and P. Ruterana, **Physics Status Sol. (b)** **236**, 61 (2003).
- [80] S. K. Pugh, D. J. Dugdale, S. Brand, and R. A. Abram, **Semiconductor Science Technology**. **14**, 23 (1999).
- [81] A. Rubio, J. L. Corkill, M. Cohen, E. Shirley, and S. G. Louie, **Physical Review. B** **48**, 11810 (1993).
- [82] M. B. Kanoun, A. E. Merada, J. Cibert, H. Aourag, G. Merada, **Journal of Alloys and Compounds**, **366**, 86 (2004).
- [83] D. Xu, H. Yang, J. B. Li, D. G. Zhao, S. F. Li, S. M. Zhuang, R. H. Wu, Y. Chen, and G. H. Li, **Applied Physics Letter**. **76**, 3025 (2000).
- [84] J. L. Corkill, A. Rubio, and M. L. Cohen, **Journal of Physics: Condensed Matter**. **6**, 963 (1994).
- [85] Murnaghan, *The Compressibility of Media under Extrem e*

Pressures. Proc. National Academic Science (U.S.A.) **30 244** (1944).

[86] S. H. WEI and A. Zunger, **Physical Review, B 50, 2719** (1996).

[87] M. E. Overberg, C. R. Abernathy, S. J. Pearton, N. A. Theodoropoulou, K. T. McCarthy, A. F. Hebard, **Applied Physics Letters, 79 1312** (2001).

[88] Y. Cui, L. Li, **Applied Physics Letters, 80 4139** (2002).

[89] T. Diet, H. Ohno, F. Matsukura, J. Cibert, and D. Ferrand, **Journal of Material Science 287 1019** (2000).

[90] C. Liu, F. Yun, and H. Morkok, **Journal of Material Science: Mater. Electron, 16, 555** (2005).

[91] M. Zajak, J. Gosk, M. Kaminska, A. Twardowski, T. Szyszko, and S. Podsiadlo, **Applied Physics Letter. 79, 2432** (2001).

[92] T. Sasaki, S. Sonoda, Y. Yamamoto, K. Suga, S. Shimizu, K. Kindo, and H. Hori, **Journal of Applied Physics. 91, 7911** (2002) .

[93] Wei et al. **Physical Review B 71, 144409** (2005).

[94] Thomas C. Schuithess, Walter M. Temmermane, Zdzislawa Szotek, William H. Butler and G. Malcolm Stocks, **Nature materials Vol. 4** (2005).

[95] B.S. Kang *et al.*, **Journal of Crystal Growth 287 74-77** (2006).

[96] E. Kalatov, H. Nakayama, H. Mariette, H. Ohta and Yu. A. Uspenskii, **Physical Review, B 66, 045203** (2002).

- [97] S. Kuwabara, T. Kondo, T. Chikyow, P. Ahmet, and H. Munekata, Jpn. **Journal of Applied Physics, Part 2** **40**, L724 (2001).
- [98] S. Dhar, O. Brandt, A. Trampert, L. Dweritz, K. J. Friedland, K. H. Ploog, J. Keller, B. Bescjpten, and G. Gntherodt, **Applied Physics Letter**. **82**, 2077 (2003).
- [99] M. Zajac, J. Gosk, E. Grzanska, M. Kaminska, A. Twardowski, B. Strojek, T. Szyszko, and S. Podsiadlo, **Journal of Applied. Physics**. **82**, 2077 (2003).
- [100] J. D. Albrecht, J. E. van Nostrand, B. Clain, Y. Liu, M. I. Nathan, and P. P. Ruden, *Mixed valence, percolation, and ferromagnetism in transition-metal-doped GaN*, **Physical Review B**. **72**. 195209 (2005).
- [101] J. Kang, K. J. Chang, and H. Katayama-Yoshida, *First-principles study of ferromagnetism in Mn-doped GaN*, **Journal of Superconductivity** **18**, p. 55-60 (2005).
- [102] M.A. Ruderman and C. Kittel, **Physical Review**, **96**, 99 (1954).
- [103] K. Yosida, **Physical Review**, **106**, 893 (1957).

Appendix

Appendix

In order to build the $A_{1-x}B_xC$ alloy in the ZB-structure, for the case $x=0.125$, it is very important to build a supercell with 64 atoms as the following struct. File. The first 32 atoms are the C atoms, and the last 32 atoms are a mixture of A and B atoms. The doped B atoms have the coordinates of atoms 33-36 in the first struct. File.

In the other cases of the $A_{1-x}B_xC$ for the other concentrations that have been studied in this thesis, a supercell of 8 atoms have been build, in which the C atoms takes the first four positions, while the others have a mixture of A and B atoms. Such that the doped material takes the positions begins from number five. As an example for the case that $x=0.25$ the doped material only takes the position number five and the other three atoms are of the form of B atoms.

First Struct. File

P LATTICE, NONEQUIVILANT ATOMS: 64
MODE OF CALCULATIONS=RELA unit=bohr

```

ATOM  1: X=0.00000000 Y=0.00000000 Z=0.00000000 RMT 1=  Z1=
ATOM  2: X=0.50000000 Y=0.00000000 Z=0.00000000 RMT 2=  Z2=
ATOM  3: X=0.00000000 Y=0.50000000 Z=0.00000000 RMT 3=  Z3=
ATOM  4: X=0.00000000 Y=0.00000000 Z=0.50000000 RMT 4=  Z4=
ATOM  5: X=0.50000000 Y=0.50000000 Z=0.00000000 RMT 5=  Z5:

```

ATOM 6: X=0.50000000 Y=0.00000000 Z=0.50000000 R_{MT} 6= Z6=
ATOM 7: X=0.00000000 Y=0.50000000 Z=0.50000000 R_{MT} 7= Z7=
ATOM 8: X=0.50000000 Y=0.50000000 Z=0.50000000 R_{MT} 8= Z8=
ATOM 9: X=0.00000000 Y=0.25000000 Z=0.25000000 R_{MT} 9= Z9=
ATOM 10: X=0.50000000 Y=0.25000000 Z=0.25000000 R_{MT} 10= Z10=
ATOM 11: X=0.00000000 Y=0.75000000 Z=0.25000000 R_{MT} 11= Z11=
ATOM 12: X=0.00000000 Y=0.25000000 Z=0.75000000 R_{MT} 12= Z12=
ATOM 13: X=0.50000000 Y=0.75000000 Z=0.25000000 R_{MT} 13= Z13=
ATOM 14: X=0.50000000 Y=0.25000000 Z=0.75000000 R_{MT} 14= Z14=
ATOM 15: X=0.00000000 Y=0.75000000 Z=0.75000000 R_{MT} 15= Z15=
ATOM 16: X=0.50000000 Y=0.75000000 Z=0.75000000 R_{MT} 16= Z16=
ATOM 17: X=0.25000000 Y=0.00000000 Z=0.25000000 R_{MT} 17= Z17=
ATOM 18: X=0.75000000 Y=0.00000000 Z=0.25000000 R_{MT} 18= Z18=
ATOM 19: X=0.25000000 Y=0.50000000 Z=0.25000000 R_{MT} 19= Z19=
ATOM 20: X=0.25000000 Y=0.00000000 Z=0.75000000 R_{MT} 20= Z20=
ATOM 21: X=0.75000000 Y=0.50000000 Z=0.25000000 R_{MT} 21= Z21=
ATOM 22: X=0.25000000 Y=0.50000000 Z=0.75000000 R_{MT} 22= Z22=
ATOM 23: X=0.75000000 Y=0.00000000 Z=0.75000000 R_{MT} 23= Z23=
ATOM 24: X=0.75000000 Y=0.50000000 Z=0.75000000 R_{MT} 24= Z24=
ATOM 25: X=0.25000000 Y=0.25000000 Z=0.00000000 R_{MT} 25= Z25=

ATOM 26: X=0.75000000 Y=0.25000000 Z=0.00000000 R_{MT} 26= Z26=
ATOM 27: X=0.25000000 Y=0.75000000 Z=0.00000000 R_{MT} 27= Z27=
ATOM 28: X=0.25000000 Y=0.25000000 Z=0.50000000 R_{MT} 28= Z28=
ATOM 29: X=0.75000000 Y=0.75000000 Z=0.00000000 R_{MT} 29= Z29=
ATOM 30: X=0.25000000 Y=0.75000000 Z=0.50000000 R_{MT} 30= Z30=
ATOM 31: X=0.75000000 Y=0.25000000 Z=0.50000000 R_{MT} 31= Z31=
ATOM 32: X=0.75000000 Y=0.75000000 Z=0.50000000 R_{MT} 32= Z32=
ATOM 33: X=0.12500000 Y=0.12500000 Z=0.12500000 R_{MT} 33= Z33=
ATOM 34: X=0.62500000 Y=0.12500000 Z=0.12500000 R_{MT} 34= Z34=
ATOM 35: X=0.12500000 Y=0.62500000 Z=0.12500000 R_{MT} 35= Z35=
ATOM 36: X=0.12500000 Y=0.12500000 Z=0.62500000 R_{MT} 36= Z36=
ATOM 37: X=0.62500000 Y=0.62500000 Z=0.12500000 R_{MT} 37= Z37=
ATOM 38: X=0.62500000 Y=0.12500000 Z=0.62500000 R_{MT} 38= Z38=
ATOM 39: X=0.12500000 Y=0.62500000 Z=0.62500000 R_{MT} 39= Z39=
ATOM 40: X=0.62500000 Y=0.62500000 Z=0.62500000 R_{MT} 40= Z40=
ATOM 41: X=0.12500000 Y=0.37500000 Z=0.37500000 R_{MT} 41= Z41=
ATOM 42: X=0.62500000 Y=0.37500000 Z=0.37500000 R_{MT} 42= Z42=
ATOM 43: X=0.12500000 Y=0.87500000 Z=0.37500000 R_{MT} 43= Z43=
ATOM 44: X=0.12500000 Y=0.37500000 Z=0.87500000 R_{MT} 44= Z44=
ATOM 45: X=0.62500000 Y=0.87500000 Z=0.37500000 R_{MT}45= Z45=

ATOM 46: X=0.62500000 Y=0.37500000 Z=0.87500000 R_{MT} 46= Z46=
ATOM 47: X=0.12500000 Y=0.87500000 Z=0.87500000 R_{MT} 47= Z47=
ATOM 48: X=0.62500000 Y=0.87500000 Z=0.87500000 R_{MT} 48= Z48=
ATOM 49: X=0.37500000 Y=0.12500000 Z=0.37500000 R_{MT} 49= Z49=
ATOM 50: X=0.87500000 Y=0.12500000 Z=0.37500000 R_{MT} 50= Z50=
ATOM 51: X=0.37500000 Y=0.62500000 Z=0.37500000 R_{MT} 51= Z51=
ATOM 52: X=0.37500000 Y=0.12500000 Z=0.87500000 R_{MT} 52= Z52=
ATOM 53: X=0.87500000 Y=0.62500000 Z=0.37500000 R_{MT} 53= Z53=
ATOM 54: X=0.37500000 Y=0.62500000 Z=0.87500000 R_{MT} 54= Z54=
ATOM 55: X=0.87500000 Y=0.12500000 Z=0.87500000 R_{MT} 55= Z55=
ATOM 56: X=0.87500000 Y=0.62500000 Z=0.87500000 R_{MT} 56= Z56=
ATOM 57: X=0.37500000 Y=0.37500000 Z=0.12500000 R_{MT} 57= Z57=
ATOM 58: X=0.87500000 Y=0.37500000 Z=0.12500000 R_{MT} 58= Z58=
ATOM 59: X=0.37500000 Y=0.87500000 Z=0.12500000 R_{MT} 59= Z59=
ATOM 60: X=0.37500000 Y=0.37500000 Z=0.62500000 R_{MT} 60= Z60=
ATOM 61: X=0.87500000 Y=0.87500000 Z=0.12500000 R_{MT} 61= Z61=
ATOM 62: X=0.37500000 Y=0.87500000 Z=0.62500000 R_{MT} 62= Z62=
ATOM 63: X=0.87500000 Y=0.37500000 Z=0.62500000 R_{MT} 63= Z63=
ATOM 64: X=0.87500000 Y=0.87500000 Z=0.62500000 R_{MT}64= Z64=

Second Struct. File

P LATTICE, NONEQUIVILANT ATOMS: 8

MODE OF CALCULATIONS=RELA unit=bohr

ATOM 1: X=0.50000000 Y=0.50000000 Z=0.00000000 R_{MT}1= Z1=

ATOM 2: X=0.00000000 Y=0.50000000 Z=0.50000000 R_{MT}2= Z2=

ATOM 3: X=0.50000000 Y=0.00000000 Z=0.50000000 R_{MT}3= Z3=

ATOM 4: X=0.00000000 Y=0.00000000 Z=0.00000000 R_{MT}4= Z4=

ATOM 5: X=0.25000000 Y=0.25000000 Z=0.75000000 R_{MT}5= Z5=

ATOM 6: X=0.75000000 Y=0.75000000 Z=0.75000000 R_{MT}6= Z6=

ATOM 7: X=0.75000000 Y=0.25000000 Z=0.25000000 R_{MT}7= Z7=

ATOM 8: X=0.25000000 Y=0.75000000 Z=0.25000000 R_{MT}8= Z8=

Notes:

- At the beginning of the structure file for all the cases, we have to take the calculations for the primitive unit cell (P).
- It was better to make the calculations by the bohr unit (0.529177 bohr = 1 Angstrom).
- It is worth noting that for the case of $x = 0.5$, we should distinguish between the atoms of Mn as Mn1 and Mn2.

جامعة النجاح الوطنية

كلية الدراسات العليا

دراسة الخصائص الأولية لأشباه الموصلات الممغطة للمخلوط الثلاثي $Ga_{1-x}Mn_xN$

إعداد

فرح علي ديب صالح

إشراف

د. عبد الرحمن مصطفى أبو لبده

و

د. محمد سلامه سالم أبو جعفر

قدمت هذه الأطروحة استكمالاً لمتطلبات درجة الماجستير في الفيزياء بكلية الدراسات العليا في

جامعة النجاح الوطنية في نابلس - فلسطين.

2008

ب

دراسة الخصائص الأولية لأشباه الموصلات الممغطة للمخلوط الثلاثي



إعداد

فرح علي ديب صالح

إشراف

د. عبد الرحمن مصطفى أبو لبده

و

د. محمد سلامة سالم أبو جعفر

ملخص

نقدم في هذه الأطروحة حساب الخصائص المغناطيسية والالكترونية للمخاليط المغناطيسية $\text{Ga}_{1-x}\text{Mn}_x\text{N}$ في حالة التركيب البلوري لكبريتات الخارصين وذلك باستخدام طريقة الموجات المستوية المعدلة الخطية لجهد تام (FP-LAPW). لقد تم استخدام تقريب الكثافة المغزلية الموضعية (LSDA) وتقريب الميل الإتجاهي المعمم (GGA) للجهد التبادلي

ت

الترابطي. لقد حصلنا على سلوك ثابت في الخصائص المغناطيسية مع ازدياد نسبة مادة المنغنيز (Mn) في الخليط.

أظهرت الدراسة الحالية بأن المركب GaN ذو طاقة فجوة مباشرة وأنه شبه موصل غير انه لا يمتلك الخصائص المغناطيسية في التركيب البلوري الحالي ، كما تم الحصول على طاقة فجوة متباينة للمخلوط $Ga_{1-x}Mn_xN$ وتبين بأنها تعتمد على تركيز مادة المنغنيز .

أظهرت النتائج الحالية بان مركب MnN في التركيب البلوري الحالي يمكن به أن يصل إلى حالة المادة المغناطيسية إذا تعرض لظروف تجعله يزداد حجما كالحرارة مثلا.